Controlling deformability in metallic glass nanopillars and nanolattices

Thesis by

Rachel Liontas

In Partial Fulfillment of the Requirements

for the Degree of

Doctor of Philosophy

California Institute of Technology

Pasadena, California

2017

(Defended September 6, 2016)

Acknowledgements

I would like to thank my academic advisor, Professor Julia R. Greer, for her enthusiasm and constant support. I am grateful for the freedom she has given me to choose my own research direction and consider which research questions are important and interesting. She has been incredibly supportive in allowing me to tailor the graduate school experience to enable pursuit of my goals. I am thankful for the resources she has provided to allow me to develop technical skills and experience with advanced microscopy, fabrication, and nanomechanical testing tools. Her encouragement to attend numerous conferences has given me the opportunity to develop presentation skills beyond what I thought was possible and to interact with and gain insight from people in a range of fields. Regardless of where my career path goes, I know I will use the presentation, communication, and critical thinking skills that Julia has been instrumental in helping me develop.

I would also like to thank Professors Frances H. Arnold, John F. Brady, William A. Goddard, Sossina M. Haile, and William L. Johnson for taking the time to serve on my candidacy and/or thesis committees and evaluate my work.

The experiments of this thesis required the use of numerous labs and user facilities around Caltech. I am especially grateful for the Kavli Nanoscience Institute (KNI) at Caltech for support and availability of cleanroom facilities throughout my time here. The KNI staff has been incredibly helpful, particularly Matthew Sullivan Hunt for fantastic SEM/FIB support that went above and beyond. Carol Garland has also provided excellent TEM training and helpful TEM discussions throughout my work. I am very grateful to the Atwater and Lewis groups for their willingness to share lab resources and to the numerous graduate students in those groups who work so hard maintaining the equipment and training others. In particular, I would like to thank Sunita Darbe, Ethan Simonoff, and Jonathan Thompson for this type of instrumental assistance.

The Greer Group has of course also played a key role in my graduate school experience. I would like to thank David Chen for discussion on metallic glasses, Dongchan Jang for training on electroplating and TEM, Lucas Meza and Lauren Montemayor for Nanoscribe training and discussion on nanolattices, and Wendy Gu for initial training and discussion on just about everything. Warren Oliver and Sam Bacon from Nanomechanics were instrumental in helping develop the method used in running many of my nanomechanical experiments conducted in the Greer Group SEMentor. Thank you to all the members of the Greer Group (past and present) that I have gotten the chance to know. The friendliness and openness of the group has made for a great work environment.

Collaborators and co-authors outside of Caltech have been great in providing additional experiments and simulations to develop further understanding of my work done at Caltech. Collaborators at Los Alamos National Laboratory including Yongqiang Wang, Nathan Mara, Engang Fu, and Nan Li as well as the Center for Integrated Nano-technologies (CINT) user program enabled use of the ion beam facilities at Los Alamos to perform the irradiations discussed in Chapter 2 and Chapter 5. Wendy Mao and Qiaoshi (Charles) Zeng performed the synchrotron XRD measurements shown in Chapter 3 and were involved in data analysis as well as helpful discussion on that topic. Mehdi Jafary-Zadeh and Yong Wei Zhang at the Institute of High Performance Computing in Singapore performed the molecular dynamics simulations discussed in Chapter 3.

I would like to thank administrators and offices at Caltech that helped enrich my experience. The administrators Kathy Bubash and Cecilia Gamboa helped make everything run smoothly. I am also grateful to the Caltech Center for Diversity for the graduate women's lunch discussion group as well as numerous excellent programming events and the Caltech Career Development Center for providing great career and professional development opportunities.

Thank you to my family for their constant love and support. I also thank Jonathan's family for being incredibly welcoming and kind.

I am grateful for the awesome friends I have made at Caltech. Michelle Dee, Nikki Peck, Bill Napier, and Kelvin Bates – thank you for all the great adventures. Lauren Montemayor, Viki Chernow, and Wendy Gu – thank you for always being there to talk, have fun, and bake some cakes. Thanks again to all of the Greer Group for making an enjoyable, friendly work environment. Special thanks to Ottman Tertuliano for his match-making skills and encouragement to pursue Jonathan.

Finally, I thank my boyfriend, Jonathan Thompson, for being my best friend and biggest supporter. Thank you for the countless hours spent discussing my research, listening to practice presentations, and helping me work through challenges. You have given me confidence when I needed it most and always believed in me. I am incredibly grateful for the chance to get to know you so well over these past few years and for all the fun we have had along the way.

I would like to acknowledge financial support during my graduate studies from my National Science Foundation Graduate Research Fellowship under Grant DGE-11444. Additional support came via the U.S. Department of Energy through Julia's Early Career Research Program under Grant DE-SC0006599, NASA's Space Technology Research Grants Program through Julia's Early Career Faculty Grant NNX12AQ49G, and the National Academies Keck Futures Initiative under Grant NAKFI ANT1.

Abstract

Metallic glasses offer desirable mechanical properties, including high strength, hardness, and elasticity. In bulk, they suffer from catastrophic failure upon mechanical loads. However, ductility may emerge upon (1) reducing the characteristic dimension of the metallic glass to the nanoscale or (2) irradiating the metallic glass. These two methods of controlling metallic glass deformability are investigated through a host of mechanical experiments on metallic glass nanopillars and nanolattices before and after irradiation. The mechanical experiments are conducted inside a scanning electron microscope to allow simultaneous mechanical loading and visualization of nanoscale deformation behavior.

Such experiments reveal that helium irradiation of electrodeposited $Ni_{73}P_{27}$ metallic glass tensile nanopillars increases plasticity by a factor of two with no sacrifice in strength. Other tensile experiments on Zr-Ni-Al metallic glass nanopillars in as-sputtered and annealed states reveal substantial ductility, highly dependent upon both the nanopillar size and processing conditions. Molecular dynamics simulations, transmission electron microscopy, and synchrotron x-ray diffraction are used to explain the observed mechanical behavior through changes in free volume and short-range order.

Larger nanolattice structures are fabricated to contain hollow beams of metallic glass, with beam wall thicknesses in the nanoscale size range that may allow proliferation of the beneficial "smaller is more ductile" size effect observed in metallic glass nanopillars. Compression experiments on Zr-Ni-Al metallic glass nanolattices reveal enhanced deformability as the nanolattice wall thickness is reduced and upon irradiation. This work points to metallic glass nanolattices as promising candidates for radiation-intensive applications and demonstrates that by fabricating the metallic glass in a nanolattice architecture the beneficial nanoscale size effect in deformability can be preserved.

Published Content

(1) **R. Liontas**, X.W. Gu, E. Fu, Y. Wang, N. Li, N. Mara, J.R. Greer. "Effects of Helium Implantation on the Tensile Properties and Microstructure of $Ni_{73}P_{27}$ Metallic Glass Nanostructures" *Nano Letters.* 14, 5176-5183 (2014). DOI: 10.1021/nl502074d

Contributions: fabricated and characterized samples (TEM, SEM, EDS), performed tensile experiments, analyzed data, performed SRIM calculations, prepared samples for ion beam implantation, monitored implantation progress, wrote manuscript with input from all authors

(2) **R. Liontas**, M.J. Zadeh, Q. Zeng, Y. Zhang, W.L. Mao, J.R. Greer. "Substantial tensile ductility in sputtered Zr-Ni-Al nano-sized metallic glass" *Acta Materialia.* 118 (2016) 270-285. DOI: 10.1016/j.actamat.2016.07.050

Contributions: fabricated samples for mechanical and XRD experiments, characterized samples (TEM, SEM, EDS), performed tensile experiments, analyzed mechanical and XRD data, provided input and discussion for MD simulations, wrote manuscript with input from all authors

(3) **R. Liontas** and J.R. Greer. "Brittle-to-deformable transition in metallic glass nanolattices via decreased wall thickness" (in preparation).

Contributions: fabricated samples, characterized samples (TEM, SEM, EDS), performed compression experiments, analyzed data, wrote manuscript

(4) **R. Liontas**, Y. Wang, J.R. Greer. "Irradiation strengthens and enhances deformability of metallic glass nanolattices" (in preparation).

Contributions: fabricated samples, characterized samples, performed compression experiments, analyzed data, prepared samples for irradiation, monitored irradiation, performed SRIM calculations, wrote manuscript

Table of Contents

List of Figures

List of Tables

List of Videos

Video 1. Tensile stress-strain response of an as-fabricated $Ni_{73}P_{27}$ metallic glass nanopillar. The video is played back at a speed 3x faster than it was captured

Video 2. Tensile stress-strain response of a helium-implanted $Ni_{73}P_{27}$ metallic glass nanopillar. The video is played back at a speed 3x faster than it was captured.

Video 3. Stress-strain response of 212-nm wide nano-tensile specimen composed of Zr-Ni-Al metallic glass in the as-sputtered state. The video is played back at a speed 10x faster than it was captured. The tensile data is shown for (a) engineering stress-strain and (b) true stress-strain.

Video 4. Stress-strain response of 114-nm wide nano-tensile specimen composed of Zr-Ni-Al metallic glass in the as-sputtered state. The video is played back at a speed 10x faster than it was captured. The tensile data is shown for (a) engineering stress-strain and (b) true stress-strain.

Video 5. Stress-strain response of 209-nm wide nano-tensile specimen composed of Zr-Ni-Al metallic glass in the annealed state. The video is played back at a speed 10x faster than it was captured. The tensile data is shown for (a) engineering stress-strain and (b) true stress-strain.

Video 6. Stress-strain response of 109-nm wide nano-tensile specimen composed of Zr-Ni-Al metallic glass in the annealed state. The video is played back at a speed 10x faster than it was captured. The tensile data is shown for (a) engineering stress-strain and (b) true stress-strain.

Video 7. Stress-strain response of 93-nm wide nano-tensile specimen composed of Zr-Ni-Al metallic glass in the annealed state. The video is played back at a speed 10x faster than it was captured. The tensile data is shown for (a) engineering stress-strain and (b) true stress-strain.

Video 8. Nanolattice with ~10 nm wall thickness compressed to ~67% strain. The video is played back at a speed 50x faster than it was captured.

Video 9. Nanolattice with ~20 nm wall thickness compressed to ~67% strain. The video is played back at a speed 50x faster than it was captured.

Video 10. Nanolattice with ~30 nm wall thickness compressed to ~67% strain. The video is played back at a speed 50x faster than it was captured.

Video 11. Nanolattice with ~38 nm wall thickness compressed to ~67% strain. The video is played back at a speed 50x faster than it was captured.

Video 12. Nanolattice with ~57 nm wall thickness compressed to ~67% strain. The video is played back at a speed 50x faster than it was captured.

Video 13. Nanolattice with ~88 nm wall thickness compressed to ~67% strain. The video is played back at a speed 50x faster than it was captured.

Video 14. As-fabricated nanolattice (~88 nm wall thickness) compressed to ~67% strain. The video is played back at a speed 50x faster than it was captured.

Video 15. Irradiated nanolattice (~88 nm wall thickness prior to irradiation) compressed to ~67% strain. The video is played back at a speed 50x faster than it was captured.

*All videos are included in the supplemental thesis files

Chapter 1. Introduction and Background

1.1. Metallic Glasses

The first report of metallic glass came in 1960 at California Institute of Technology. There, W. Klement et al. [1] found that if molten metal (in their case the binary alloy $Au_{80}Si_{20}$) is uniformly and rapidly cooled then there is insufficient time and energy for the atoms to rearrange and nucleate crystals. Instead, when the molten metallic alloy reaches its glass transition temperature (T_g) it solidifies as a metallic glass with atoms in an amorphous distribution, randomly packed with no long-range order. Metallic glasses have a combination of characteristics; like crystalline metals, metallic glasses have cohesive metallic bonding and appear opaque, gray, and shiny as shown in Figure 1 (a), like oxide glasses, metallic glasses have an amorphous atomic-level structure as shown in Figure 1 (b).

This combination of features leads to a host of desirable properties. The absence of grain boundaries in metallic glasses makes the material corrosion and wear resistant with excellent soft magnetic properties [2-4]. In addition, the amorphous structure of metallic glasses hinders the displacement of atoms, for example to accommodate a dislocation. Thus compared to a material with a crystalline microstructure, a metallic glass responds to mechanical deformation by absorbing less energy through damping and returning more energy by elastically returning to its initial state [3]. The lack of crystal defects in metallic glasses also leads to desirable mechanical properties including high strength and hardness, a large elastic limit, elasticity, and low mechanical dissipation [2]. The superior strength and elasticity of metallic glasses as compared to other materials is illustrated in Figure 1 (c).

Due to these beneficial properties, metallic glasses have started to see use in a variety of applications. One of the first applications was in sporting equipment, such as baseball bats and golf clubs, where the excellent strength and elasticity of metallic glasses allowed them to transfer more energy to the ball [5], see for example Figure 1 (d). Metallic glasses have also

seen use in watch cases and jewelry to replace Ni and other metals that may cause allergic reactions, along with providing enhanced scratch- and dent- resistance as well as a high gloss finish [3]. Liquidmetal Technologies, a company focused on commercializing metallic glasses, has numerous patents with Apple to incorporate metallic glasses into iPhones, and the iPhone sim ejector is currently made of metallic glass [6]. Metallic glasses have also found use in aerospace applications, such as the $200 million Genesis spacecraft [3].

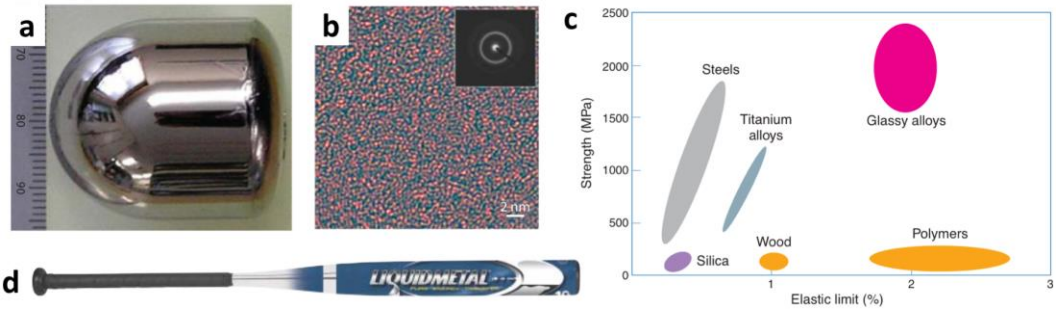

Figure 1. Metallic glass properties and applications. (a) A sample of bulk metallic glass illustrates the typical opaque, shiny, metallic appearance of these alloys. (b) Metallic glasses contain an amorphous structure with no long range order as shown by this characteristic diffuse ring diffraction pattern and high resolution transmission electron microscopy image. (c) Metallic glasses possess high strength and a large elastic limit compared to other materials, as illustrated in this chart. (d) Metallic glasses have seen use in applications such as sporting equipment, including this baseball bat made by Liquidmetal Technologies. (a, b) were adapted from [7] with permission and (c, d) were adapted from [3] with permission.

The availability of convenient metallic glass processing techniques, such as thermoplastic forming and blow molding [8], gives metallic glasses a processability comparable to plastics. This enhanced processability allows for metallic glasses to be fabricated into a variety of intricate geometries and custom shapes precisely and inexpensively, for example in biomedical devices and complex implants [9]. The low flow stresses that allow metallic glasses to be molded like plastics along with the homogeneous and isotropic structure of metallic glasses also renders metallic glasses as ideal materials for use in nanofabrication [10] and templates for nanoimprint lithography [11]. Economically and scalably fabricating large surface area

nano-architectures with the appropriate chemical composition of some metallic glasses also is applicable to electrochemical catalysts [12], specifically fuel cells [13].

1.2. Strategies to induce ductility in metallic glasses

Despite the suite of desirable properties observed in metallic glasses, these materials have seen limited use in structural applications because of their low ductility. Upon loading a metallic glass, strains are first accommodated by elastic deformation until the stress activates flow in a locally perturbed region, causing strain to accumulate in that region [14]. These locally perturbed regions are often referred to as shear transformation zones (STZs), pictured schematically in Figure 2 (a, b). STZs involve local collections of atoms rearranging under applied stress, resulting in shear displacements, and in most cases shear banding [14]. Room temperature deformation of metallic glasses typically involves localization of plastic strain into narrow shear bands shown in Figure 2 (c, d), which result in catastrophic failure and a lack of tensile ductility [14].

Some monolithic bulk metallic glasses have been shown to exhibit significant plasticity under compression [15-19]; however all exhibit virtually no extendibility (<0.5% strain) under tension. The lack of tensile ductility leads to characteristic stress-strain data involving linear elastic loading followed by failure with almost no plastic strain; a representative stress-strain response of a metallic glass under tension is displayed in Figure 2 (e). Consequently, recent studies have focused on understanding the potential of metallic glasses to accommodate plastic deformation and developing strategies to mitigate their inherently brittle behavior, suppress catastrophic failure, and impart tensile ductility.

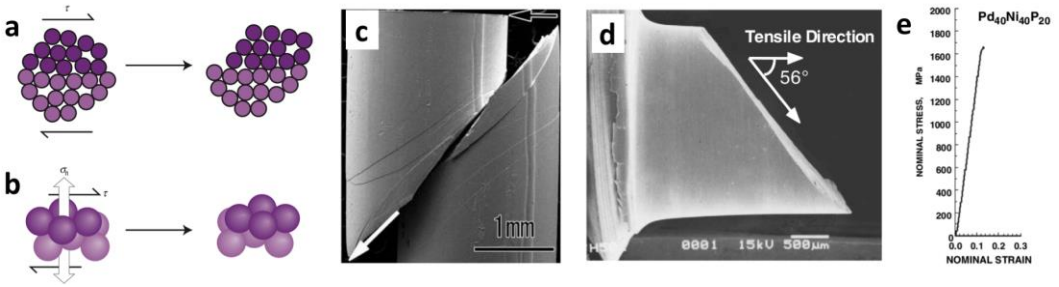

Figure 2. Typical deformation in metallic glasses. Schematic of shear transformation zones represented in (a) 2-dimensions and (b) 3-dimension with local collections of atom rearranging as result of the applied shear stress, τ (c) Typical morphology of metallic glass under compression, shear bands are clearly visible. (d) Typical morphology of shear band failure surface in metallic glass after tensing with the corresponding stress-strain data shown in (e) where almost no plastic strain is observed before failure. (a, b) are adapted from [20] with permission, (c) is adapted from [21] with permission, and (d, e) are adapted from [22] with permission.

1.2.1. Irradiation

One such strategy that has emerged recently to induce ductility in metallic glasses is utilizing irradiation [23-26]. While it is well known that irradiating crystalline materials with high-energy ions causes the formation of self-interstitials, vacancies, and voids, which lead to hardening, embrittlement, and a degradation of mechanical properties [27-34], the effects of irradiation on metallic glasses are not as well understood.

Some studies on irradiation of metallic glasses have demonstrated an actual improvement in mechanical properties, specifically ductility, upon irradiation. Studies to date on the tensile properties of ion-irradiated metallic glasses have mostly utilized Ga^+ ion irradiation from a focused ion beam (FIB), due to the ease of accessing such irradiation with SEM-FIB dual-beam systems. In these studies, FIB-induced Ga^+ irradiation on the sample surfaces was found to cause originally brittle $Pt_{57.5}Cu_{14.7}Ni_{5.3}P_{22.5}$ metallic glass nanowires to exhibit post-yielding strains of up to 2% [23] and $Ni_{80}P_{20}$ metallic glass nanopillars to increase in tensile ductility by a factor of three [24]. Another study found that Ni irradiation led to smaller stress drops and reduced yield strength in the compression of $Zr_{41.2}Ti_{13.8}Cu_{12.5}Ni_{10}Be_{22.5}$ metallic glass, implying enhanced ductility with irradiation [26]. In molecular dynamics simulations of irradiated

$Zr_{50}Cu_{40}Al_{10}$ metallic glass nanopillars, increasing irradiation caused the plastic deformation mode to switch from localized shear banding to homogeneous shear flow [25]. These studies suggest that irradiation is capable of enhancing the mechanical performance and ductility of otherwise brittle metallic glasses, thus rendering metallic glass components and thin coatings suitable candidates for irradiation-intensive applications, such as space and nuclear energy.

1.2.2. Reducing sample dimension

Another approach to induce ductility in metallic glass involves reducing the external dimension of the metallic glass sample below some critical length scale, on the order of ~100 nm. Such sample size reduction has been found to induce a brittle-to-ductile transition in bending [35,36], compression [37-39], and tension [40-42] in what is often referred to as a "smaller is more ductile" effect.

Tensile ductility at room temperature is particularly elusive and has been shown to emerge in monolithic metallic glasses only when the sample size is reduced to the nanoscale [40,41,43]. The extent of tensile ductility induced by sample size reduction was reported to vary widely as a function of the specific metallic glass and its processing conditions, with some studies indicating almost no plasticity (<1%) even for sub-100 nm molded $Pt_{57.5}Cu_{14.7}Ni_{5.3}P_{22.5}$ [23,44] and electrodeposited $Ni_{80}P_{20}$ [24], others reporting strains of 23-45% for 100 nm copper-mold casted $Zr_{52.5}Cu_{17.9}Al_{10}Ni_{14.6}Ti_5$ [41] (shown in Figure 3 (Top)), 25% for 100 nm sized $Zr_{35}Ti_{30}Co_6Be_{39}$ [40] (shown in Figure 3 (Bottom)), and others reporting elongation of 200% for <20 nm nanohills of twin-jet electropolished $Al_{90}Fe_5Ce_5$ [43]. While these studies are promising in achieving tensile ductility by nano-sizing the metallic glass, the origins of such a wide range of post-elastic deformability in nano-sized metallic glasses are not well understood.

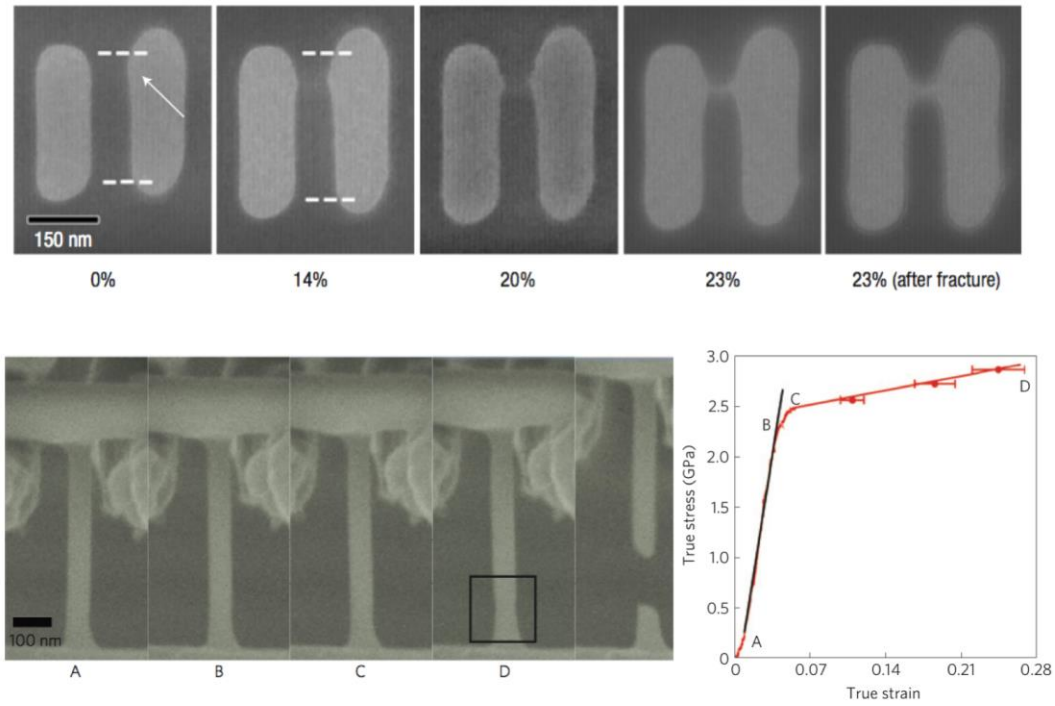

Figure 3. Existing literature on ductility and necking in ~100 nm metallic glass nanopillars. (Top) TEM images of 100 nm copper-mold casted $Zr_{52.5}Cu_{17.9}Al_{10}Ni_{14.6}Ti_5$ during tensile testing. (Bottom) SEM images of 100 nm $Zr_{35}Ti_{30}Co_6Be_{39}$ during tensile testing with corresponding true stress-strain data. (Top) is adapted from [41] with permission and (Bottom) is adapted from [40] with permission.

The observed "smaller is more deformable" effect has primarily been rationalized by considering the energetic completion between shear band propagation and homogeneous deformation [23,24,41,45]. For a sample of dimension, L, the energy required for a crack-like shear band to propagate scales with the sample cross-sectional area, or

$$E_{shear\ band} \sim L^2 \quad (1)$$

while the energy required to deform a sample in a homogeneous way scales with the sample volume, or

$$E_{homogeneous} \sim L^3 \quad (2)$$

Figure 4 (a) illustrates that as the sample dimension is reduced L^3 decreases faster than L^2, with the result that shear band propagation may become energetically unfavorable in nanoscale volumes. Analogous to Griffith criterion for crack propagation, these energetic scaling

arguments can be further used to estimate the critical stress for shear band formation as has been discussed elsewhere [38,40].

Another way the size effect has been rationalized is by considering that small samples may be smaller than certain deformation units within metallic glasses. Some have stated that in order for a shear band to be fully developed and propagate its nucleus would need to be at least ~50-500 nm [14,41,46]. As such, small nanoscale samples may not provide sufficient space for shear banding to occur. Another deformation unit relevant at even larger length scales is the plastic zone size at the tip of an incipient crack, which can be micron-sized or larger. If the plastic zone size is greater than the sample size then brittle failure is not expected [2] and bending plasticity is greatly enhanced when the plastic zone is larger than half the sample thickness [35,47,48]. Figure 4 (b) illustrates the sizes of typical deformation units and regimes of observed size effects in $Zr_{41.2}Ti_{13.8}Cu_{12.5}Ni_{10}Be_{2s.5}$ (Vit1). In Figure 4 (b) the size regime most relevant for this thesis is the sub-100 nm region labeled "homogeneous deformation". While bending and compressive plasticity can be observed at larger length scales, only at the nano-scale has tensile ductility been observed in monolithic metallic glasses at room temperature. All samples in this thesis will involve some characteristic dimension close to this ~100 nm size range.

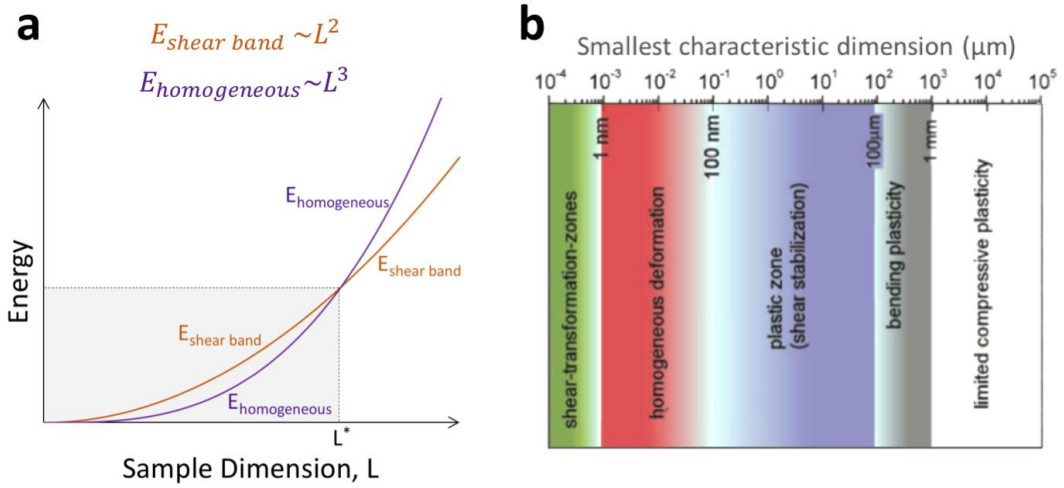

Figure 4. Rationalizations for the "smaller is more deformable" size effect in metallic glasses. (a) Energetic scaling comparison between shear band propagation and homogeneous deformation. (b) Size effects in metallic glasses with dimensions estimated for $Zr_{41.2}Ti_{13.8}Cu_{12.5}Ni_{10}Be_{22.5}$ (Vit1). (b) is adapted from [49] with permission.

1.2.3. Considering atomic structure

Another strategy for enhancing ductility in monolithic metallic glasses has focused on the choice of alloying elements and the corresponding stoichiometry of those constituent elements. Some studies indicate that ductility can be brought about by choosing alloying elements such that the ratio of the shear modulus (G) to the bulk modulus (B) is low, that is, G/B less than 0.41-0.43 [17,50,51]. The correlation between a small G/B ratio and inherent ductility was first studied in polycrystalline metals [52], where it was rationalized by considering that the shear modulus, G, is proportional to resistance to plastic deformation, and the bulk modulus, B, is proportional to fracture strength; thus a smaller value of G/B corresponds to a larger plastic range before fracture. For metallic glasses, a small G/B ratio favors the tip of a shear band extending rather than initiating a crack, allowing deformation to occur by the formation of multiple shear bands that intersect as opposed to a single catastrophic shear band failure event [17]. Another study investigated the effect of metallic glass composition on intrinsic plasticity or brittleness and found that metallic glasses with compositions at or near

intermetallic compounds were extremely ductile compared to those with compositions at or near eutectics [53].

These investigations do not take into account the effects of the metallic glass fabrication method and processing conditions on ductility, which likely serve as key factors in governing post-elastic deformability in these materials. Metallic glasses may be formed through a variety of methods including splat quenching, melt spinning, copper-mold casting, arc melting, electrodeposition, and sputtering. A metallic glass formed by copper-mold casting could exhibit a significant difference in ductility than a metallic glass with the same chemical composition formed by sputtering. Even a single metallic glass fabrication method has some variability in processing conditions, such as the cooling rate of splat quenching or the deposition conditions of sputtering, which could greatly influence the short- and medium-range atomic order as well as the presence of free volume.

1.2.4. Metallic glass foams and cellular solids

An additional strategy for imparting plasticity to metallic glasses is by utilizing microstructural architecture, which can be done either stochastically to create metallic glass foams with a random distribution of feature sizes or periodically to create ordered metallic glass cellular solids with precise architectures. Metallic glass systems incorporating architecture are particularly promising for their high energy absorption capacity, where the very high strength and elasticity of metallic glasses offers the opportunity to develop very elastic spring-like cellular solids with excellent strength [54]. Furthermore, architecture may allow for proliferation of the beneficial "smaller is more deformable" size effect in metallic glasses, discussed in section 1.2.2 to create larger meta-materials.

The most important structural characteristic of a cellular solid is its relative density ($\bar{\rho}$), which is defined as the density of the cellular solid (ρ^*) divided by the density of the solid material making up the cellular solid (ρ_s) [55],

$$relative\ density \equiv \bar{\rho} = \frac{\rho^*}{\rho_s} \tag{3}$$

Relative density is also equivalent to the volume fraction of the solid. Example values of relative density for cellular solids are 0.001 for special ultra-low-density foams, 0.05-0.2 for polymeric foams used for packaging and insulation, and 0.14 for cork [55]. The use of cellular structure can allow a material to have good mechanical properties while maintaining a low mass and low relative density.

A cellular material under compression undergoes three regimes of behavior in its stress-strain response [55], as shown in Figure 5. Initially, the bending of cell edges corresponds to the linear elastic behavior. This linear elastic region is followed by a stress plateau involving cell collapse and specific behavior, such as plastic yielding or brittle failure, dependent on the nature of the solid material from which the cellular solid is composed [55]. The final regime begins when opposite cell walls come into contact, with further deformation compressing the cell wall material itself. This results in the steeply rising regime of the stress-strain response, known as densification [55].

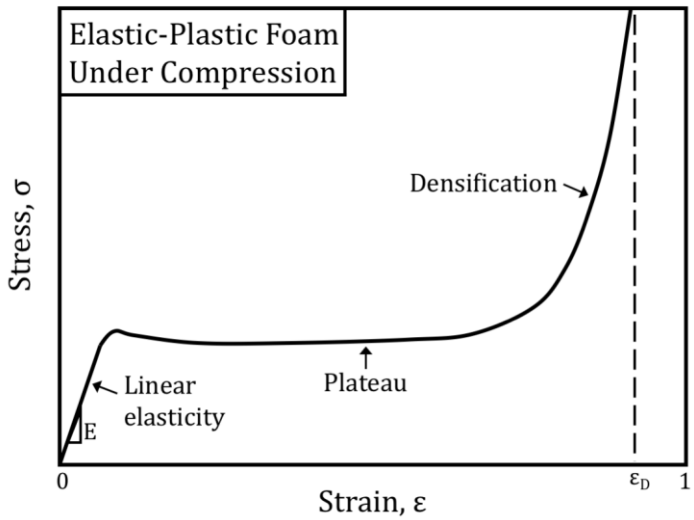

Figure 5. Typical uniaxial stress-strain response for an elastic-plastic foam under compression. The three regimes of the mechanical behavior (linear elasticity, plateau, and densification) are labeled. Based on [55].

Stochastic metallic glass foams have been more commonly studied than periodically architected metallic glass cellular solids due to the availability of various pore forming techniques, where gas or some other space-holder material is incorporated to create a non-uniform pore size distribution. One study found ~80% compressive ductility for open-cell Zr-based amorphous metal foams with relative densities of 14-28% and pores sizes of 150-355 μm [56]. Another study found that the commercial glass-forming alloy Vit106, which exhibits no significant plasticity in the monolithic alloy, can become ductile under compression (reaching ~50% strain) when it is made into an open-cell foam with porosity ~78% and pore size 212-250 μm [57]. In another study, open-cell $Zr_{41.25}Ti_{13.75}Cu_{12.5}Ni_{10}Be_{22.5}$ metallic glass foams, fabricated by using NaCl as a space-holder material, were shown to exhibit high energy absorption capacity with ductile cracking a result of the complex stress state arising from the presence of pores in the foam [58]. While these results are promising, stochastic cellular structures almost always contain imperfections and are therefore difficult to manipulate and study systematically. Furthermore, the randomness of the architecture can lead to a reduction in mechanical performance [59,60], particularly elastic modulus and yield strength, which have

been shown to be lower in stochastic metallic glass foams compared to periodically ordered metallic glass foams [61].

Unlike stochastic foams, periodically architected foams may be precisely engineered with a completely tunable architecture for optimal mechanical performance. Study of such periodically architected metallic glass foams has been limited due to the difficulty in fabricating such materials, particularly in three dimensions. One study utilized thermoplastic replication of metallic glass to fabricate two-dimensional metallic glass cellular structures that ranged from perfectly periodic to highly stochastic, and observed that while the periodic structures generally had improved mechanical performance, as evidenced by higher elastic modulus and yield strength compared to stochastic structures, the stochastic structures exhibited higher flaw tolerance [61], as shown in Figure 6 (a-c). To create three-dimensional periodically architected metallic glass structures, one study utilized thermoplastic forming-based patterning of metallic glass sheets combined with parallel joining, which resulted in honeycomb-like architectures exhibiting high elastic energy storability and superior energy absorption [54]. Another study achieved three-dimensional periodically architected metallic glass cellular structures with electroless deposition of Ni-P metallic glass onto a sacrificial polymer microlattice, which was fabricated from an interconnected pattern of self-propagating photopolymer waveguides [62]. The resultant metallic glass microlattices consisted of ~1 mm unit cells with metallic glass wall thicknesses of 60 – 600 nm (Figure 6 (d)), and reported structures with wall thicknesses above 150 nm failed catastrophically while those with wall thicknesses below 150 nm failed with significant plasticity [62] (Figure 6 (e-h)). Even smaller periodically architected three-dimensional cellular structures were fabricated by sputtering $Cu_{60}Zr_{40}$ metallic glass onto polymer nanolattice templates fabricated by two-photon direct laser write lithography [63]. These resultant metallic glass nanolattices consisted of ~15 μm unit cells with metallic glass

wall thicknesses of 20, 60, and 120 nm, and reported a brittle-to-ductile transition occurring as the wall thickness was reduced [63].

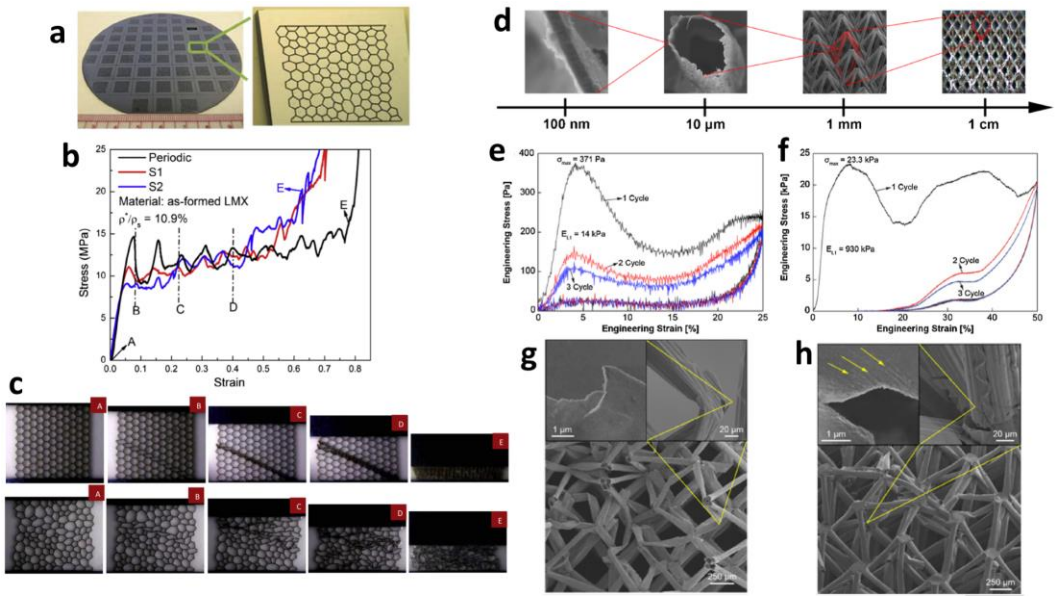

Figure 6. Existing literature on metallic glass cellular solids. (a-c) are adapted from [61] with permission and (d-h) are adapted from [62] with permission. (a) Si molds fabricated for replicating bulk metallic glass two-dimensional cellular structures, (b) stress-strain data obtained from stochastic and periodically architected metallic glass cellular structures with 10.9% relative density, (c) corresponding sequential microstructural evolution in periodically architected and stochastic metallic glass cellular structures. (d) Open cellular structure of periodically architected NiP metallic glass microlattices, which are tested under cyclic compression to obtain the stress-strain data shown in (e, f) and the corresponding post-compression images in (g, h) for microlattices with wall thickness of (e, g) 85 nm and (f, h) 600 nm.

1.3. Nanomechanical testing

Advances in nanofabrication processes have enabled precise control of material dimensions and microstructure, facilitating the use of highly controlled nanoscale mechanical testing specimens. The mechanical behavior of nanoscale materials is of interest due to the emergence of nanoscale size effects in mechanical behavior and the potential for exploiting such size effects to develop nano-architected materials. These size effects take different forms depending on the material microstructure. One of the most well-studied size effects is the

"smaller is stronger" effect observed in single crystalline metals. Reducing sample dimensions of single crystalline metals to sub-micron levels leads to an order of magnitude increase in strength over bulk materials [64-66]. The relation between single crystalline pillar strength (σ) and diameter (d) is generally described by a power law,

$$\sigma = Ad^{-n} \tag{4}$$

where A is an empirically determined constant and n is a power law exponent, which is ~0.6 for FCC metals, the most widely studied system in nanopillar mechanics. While the "smaller is more ductile or deformable" size effect in metallic glasses, discussed in section 1.2.2, is not as well understood as the "smaller is stronger" size effect in single crystalline metals, it presents a similar opportunity to exploit improved mechanical behavior arising at nano length scales.

The nanopillar is one specimen that has seen ubiquitous use in fundamental experimental studies of nanoscale mechanical behavior [67,68]. Nanopillars generally contain a round or square cross-section with a width (i.e. critical dimension) less than 1 μm, and can be fabricated from a variety of materials. The most common fabrication method, focused-ion beam (FIB) milling, involves using the focused-ion beam in an SEM to mill the material of interest into a desired geometry. One disadvantage of FIB fabrication is that the milling is performed by irradiation, usually with a high energy Ga^+ ion beam, which can modify local arrangements of atoms and even cause surface crystallization in metallic glasses [69-71]. However, there has been a scarcity of "FIB-less" fabrication techniques for individual metallic glass nanomechanical testing specimens. Two viable techniques that have been utilized recently are: (1) hot embossing metallic glass molds, which can subsequently be crystallized and used to form additional metallic glass replicas, with resultant feature sizes as small as 13 nm [11], and (2) lithographically patterning vertical pores in resist then electroplating into those pores to form arrays of vertically-oriented nanopillars [72].

Common mechanical tests on confined (nano) geometries include nanoindentation of thin films and uniaxial compression or tension testing of nanopillars, as shown schematically in Figure 7. Of these three testing options, tension testing can provide the most information about intrinsic material properties. In contrast, nanoindentation, which involves pressing a hard indenter tip into a thin film of material, suffers from measurements influenced by large strain gradients and underlying substrate effects. These effects make it a less suitable test for assessing mechanical behavior intrinsic to the material. While both uniaxial compression and tension tests can be conducted on nanopillars to determine mechanical behavior without the presence of large strain gradients or substrate effects, compression tests are not as useful for obtaining some mechanical properties, particularly ductility. Compression tests involve inhomogeneous deformation, a gauge section that is difficult to assess, and a contact area between sample and tip that continually evolves during testing. Tension testing avoids these disadvantages and also allows for observation of certain deformation morphology, such as necking and fractured surfaces, which is well suited for evaluating ductility. It is also a powerful technique for establishment of sought-after mechanical properties, such as plastic strain, ultimate tensile strength, and fracture toughness.

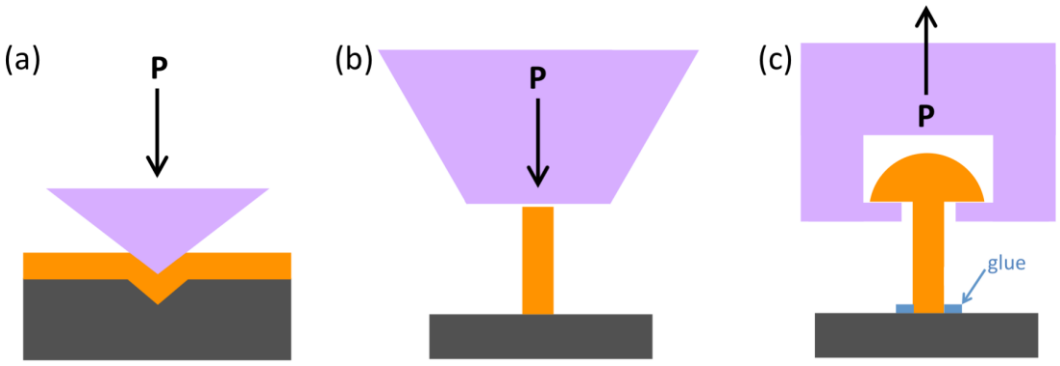

Figure 7. Common nanomechanical testing configurations. Load, *P*, is applied for (a) nanoindentation of a thin film, (b) uniaxial compression testing of a nanopillar with a flat-punch tip, and (c) uniaxial tension testing of a nanopillar with a diamond tip FIB-milled into tensile grips. Prior to testing, the tensile nanopillar may be secured to the surface with glue.

To perform nanomechanical tensile testing, it is necessary to conduct the experiment inside a scanning electron microscope (SEM). SEM-level resolution is required in order to be able to observe the specimen in enough detail to align the tensile grips in the proper position for testing, as illustrated in Figure 7 (c). In-situ testing also allows direct observation of a sample's mechanical response and correlation of observed behavior with measured stress-strain data. Observation of mechanical events, such as necking, crack nucleation and propagation, and shear banding, can provide significant insight to help understand a material's mechanical response. The mechanical experiments conducted in subsequent chapters were conducted with either the InSEM system by Nanomechanics, Inc. or the PI-85 by Hysitron. A typical in-situ mechanical testing setup is illustrated in Figure 8.

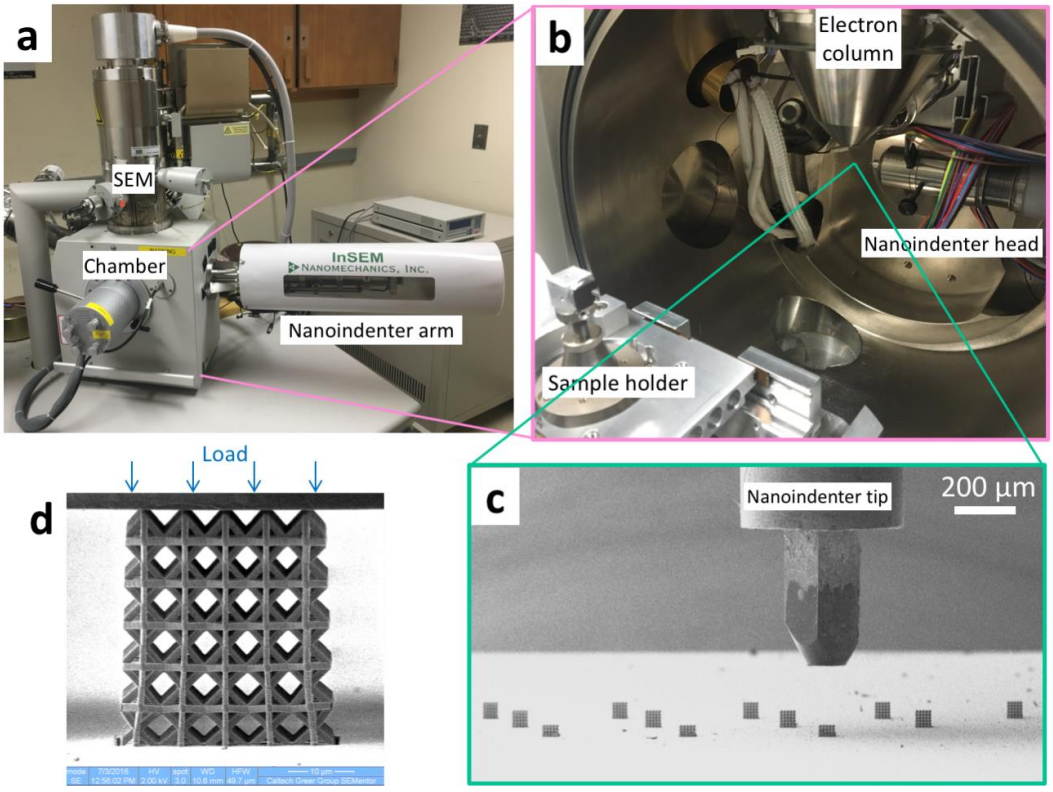

Figure 8. Typical in-situ mechanical testing setup. The setup includes (a) SEM with nanoindenter inserted into side of the chamber for simultaneous mechanical testing and imaging. (b) Inside the SEM chamber the nanoindenter head can be observed underneath the electron column, where the sample will be moved for mechanical experiments. (c) The nanoindenter can be fitted with a flat punch tip used to compress samples, as pictured here. (d) A typical SEM image obtained during compression of a nanolattice sample.

1.4. Objectives

The aim of this thesis is to develop an understanding of some of the factors that govern deformability in nano-sized metallic glasses, with particular emphasis on the influences of irradiation and the "smaller is more ductile or deformable" size effect and irradiation. Deformability is assessed via uniaxial tension and compression experiments on metallic glass samples conducted inside a scanning electron microscope to allow simultaneous mechanical loading and visualization of nanoscale deformation behavior. The size effect is investigated first through fundamental studies on metallic glass nanopillars of various sizes and then through study of larger nano-architected metallic glass samples, referred to as nanolattices, which are composed of hollow metallic glass beams with beam wall thickness on the nanoscale. Irradiation is investigated by bombardment of metallic glass nanopillars and nanolattices with ions, followed by assessment of any changes in mechanical behavior.

The word "deformability" is used here to refer generally to ductile-like behavior, which may involve necking, homogeneous flow, and gradual, continuous deformation in contrast to the catastrophic shear-banding failure frequently observed in bulk metallic glasses. Ductility is technically defined as a material's ability to deform under tensile stress while deformability can be generally applied to other modes of deformation, such as compression. As such, deformability is the more general, widely applicable term, which is chosen for use in this thesis.

Chapter 2. Effects of helium implantation on the tensile properties and microstructure of $Ni_{73}P_{27}$ metallic glass nanopillars

Adapted with permission from:

R. Liontas, X.W. Gu, E. Fu, Y. Wang, N. Li, N. Mara, J.R. Greer. "Effects of Helium Implantation on the Tensile Properties and Microstructure of $Ni_{73}P_{27}$ Metallic Glass Nanostructures" *Nano Letters.* 14, 5176-5183 (2014). DOI: 10.1021/nl502074d

In this chapter we report fabrication and nanomechanical tension experiments on as-fabricated and helium-implanted ~130 nm diameter $Ni_{73}P_{27}$ metallic glass nanopillars. The nanopillars were fabricated by a templated electroplating process and implanted with He^+ at energies of 50, 100, 150, and 200 keV, to create a uniform helium concentration of ~3 at. % throughout the nanopillars. Transmission electron microscopy (TEM) imaging and through-focus analysis reveal that the specimens contained ~2 nm helium bubbles distributed uniformly throughout the nanopillar volume. In-situ tensile experiments, which allow correlation of tensile stress-strain data with morphological evolution of the specimens, indicate that helium-implanted specimens exhibit enhanced ductility as evidenced by a 2-fold increase in plastic strain over as-fabricated specimens, with no sacrifice in yield and ultimate tensile strengths. This improvement in mechanical properties suggests that metallic glasses may actually exhibit a favorable response to high levels of helium implantation.

2.1. Motivation

To assess the use of metallic glasses in irradiating environments, additional studies are needed beyond those discussed in section 1.2.1, particularly studies utilizing more relevant irradiation ions, such as helium, implanted throughout the sample volume, not just at the sample surface as in previous studies [23,24]. Certain irradiation conditions can produce helium in solid materials, such as transmutation reactions in nuclear reactor environments. The low solubility of helium in metals leads to its precipitation into bubbles and voids, which cause embrittlement of crystalline metals and alloys [27,73-75]. However, the effect of such helium irradiation on the tensile properties of metallic glasses is not well understood as most experimental studies on irradiated metallic glass have focused on FIB-induced Ga^+ ion irradiation [23,24], due to the ease of accessing such irradiation with SEM-FIB dual beam systems. Studying the tensile properties of metallic glasses upon helium implantation, where the incoming helium ends up in the metallic glass material, would be particularly relevant for radiation applications where helium byproducts are produced in materials, such as neutron irradiations, high energy proton irradiations, and nuclear reactors.

Ion beam irradiation with particle accelerators allows irradiation of materials with small dimensions by a variety of ions, including He^+, and has been shown to be a time- and cost-effective method for studying radiation damage in small-scale specimens [76-79]. Small-scale nanotensile specimens fabricated without the use of ion irradiation, such as FIB, are well-suited for such studies because the small specimens size allows full penetration by ion accelerators, the ensuing nano-tension tests enable quantitative assessment of mechanical properties, including ductility, under known stress states, and FIB-less fabrication avoids the complicating effects of additional irradiation. The effects of FIB irradiation have been shown to include ductility enhancement in metallic glass [23,24], modification of local atom arrangements [69,71], and surface crystallization [70]. The scarcity of "FIB-less" fabrication

techniques for individual metallic glass nanopillars has limited dedicated nanomechanical studies of irradiated metallic glasses. One viable technique reported by Kumar et al. utilizes hot embossing to create metallic glass molds, which can subsequently be crystallized and used to form additional metallic glass replicas [11]. Another technique developed by Burek et al. [72] and utilized in this chapter involves lithographically patterning vertical pores in resist and then electroplating metallic glass into those pores to form arrays of vertically-oriented nanopillars [72].

2.2. Fabrication of electrodeposited $Ni_{73}P_{27}$ tensile specimens

Specimens were fabricated using the FIB-less templated electroplating process developed by Burek et al. [72] In brief, 130-nm diameter nano-tensile cylinders were formed by first utilizing electron-beam lithography to create a poly(methyl methacrylate) (PMMA) template containing vertical pores, and subsequently electroplating $Ni_{73}P_{27}$ metallic glass into those vertical pores. The nanopillar arrays were fabricated on 1 cm^2 Si substrates covered by a 20 nm thick Ti adhesion layer and a 100 nm thick Au seed layer deposited on the substrates by electron beam evaporation. The conductive Au seed layer serves as a cathode in electroplating of the nanomechanical testing specimens. PMMA 495A8 resist (Micro-Chem Corp.) is spin-coated at 4000 rpm on top of the Si/Ti/Au layers to create a ~500 nm thick layer of PMMA. The PMMA is patterned by electron beam lithography (Leica Electron-Beam-Pattern-Generator 5000+) to create a template of ~130 nm diameter vertical pores, and Ni-P is electroplated galvanostatically into these pores. A nickel-phosphorous metallic glass was chosen because it is amenable to electrodeposition [80-84]. The electrodeposition occurs according to the following cathodic reaction mechanism [82]:

$$Ni^{2+} + 2e^- \rightarrow Ni(s) \quad (5)$$

$$HPO_3^{2-} + 2H_2O + 2e^- \rightarrow H_2PO_2^- + 3OH^- \quad (6)$$

$$H_2PO_2^- + e^- \rightarrow P(s) + 2OH^- \quad (7)$$

During electroplating, a constant current between the anode (Ni foil) and the cathode (Au) is provided, and tensile specimens are formed by electroplating the Ni-P metallic glass above the level of the PMMA surface to create hemispherical-shaped "mushroom caps" on top of the nanopillars. These "mushroom caps" serve as grips to grab during tensile testing of individual nanopillars. Following electroplating, the PMMA template is removed by dissolution in acetone, resulting in a free-standing array of vertically oriented nanopillars with "mushroom caps". An overview of the fabrication process is illustrated in Figure 9.

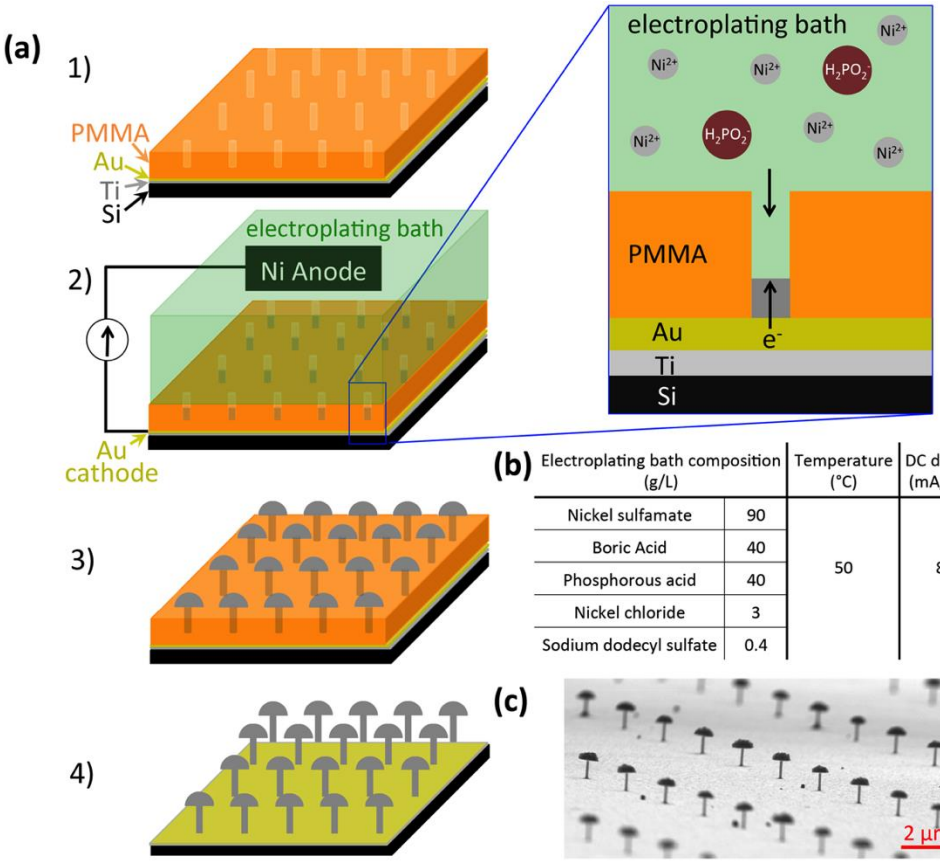

Electroplating bath composition (g/L)		Temperature (°C)	DC density (mA/cm²)	Anode
Nickel sulfamate	90	50	80	Nickel plate
Boric Acid	40			
Phosphorous acid	40			
Nickel chloride	3			
Sodium dodecyl sulfate	0.4			

Figure 9. Fabrication of $Ni_{73}P_{27}$ nanopillars. (a) Schematic representation of the fabrication, starting with (1) an electroplating template consisting of a Si substrate coated with 20 nm of Ti, 100 nm of Au, and 500 nm of PMMA patterned with e-beam lithography to contain an array of vertical pores, (2) $Ni_{73}P_{27}$ is electroplated into the vertical pores with inset depicting the details, (3) electroplating is continued until the $Ni_{73}P_{27}$ deposits above the PMMA layer to create tensile "mushroom caps" on the nanopillars, (4) the PMMA is dissolved in acetone, resulting in a free-standing array of $Ni_{73}P_{27}$ tensile nanopillars. (b) Electroplating conditions. (c) SEM image of as-fabricated $Ni_{73}P_{27}$ nanopillars.

Before tensile testing, the electroplated Ni-P nanopillars were secured to the Au substrate by using the electron-beam in an SEM (Nova 200 Nanolab, FEI co.) to deposit a small amount of W at the base of the nanopillar. This W deposition was performed at an energy of 30 keV and a current of 0.63 nA.

After specimens were fabricated, the 1 cm^2 substrate on which the specimens were grown contained thousands of nanopillars and was cleaved into halves, with one of the halves subsequently implanted with He^+ and the other half left as-fabricated. Nanomechanical experiments conducted on the individual nanopillars from each half allowed a direct comparison between helium-implanted and as-fabricated specimens that had been fabricated under completely identical conditions, and thus contained identical original microstructure and chemical composition.

2.3. Helium implantation

Helium implantation was conducted using a Danfysik 200 keV ion implanter at Los Alamos National Laboratory. The samples were mounted with silver paste onto a large Cu holder, which served as a heat sink. The temperature at the Cu mount was continuously measured and kept at room temperature. The energies and fluences were selected according to SRIM calculation to create an overall uniform helium concentration of ~3 at. % throughout each sample. The implantations were performed at room temperature, with the helium implanted vertically into the nanopillars in the form of He^+, as shown schematically in Figure 10 (a), using several different energies and fluences, noted in Figure 10 (b). The implantations were conducted in order of highest energy to lowest energy: 200 keV, 150 keV, 100 keV, and then 50 keV. The helium concentration profiles and displacements per atoms (dpa) were calculated using the Stopping and Range of Ions in Matter (SRIM) software [85] with the Kinchin-Pease model, the bulk density for $Ni_{73}P_{27}$ (6.985 g cm^{-3}), and the default threshold

displacement energies for Ni and P (25 eV). The profiles for each implantation energy are shown in Figure 10 (c, d). The resultant radiation damage within the specimens, measured in dpa, was non-uniform, with more damage occurring near the top of the specimens, as expected for the vertical top-down nature of the implantation. Implanting He^+ vertically from above the sample results in more He^+ ions travelling through the top of the specimens than the bottom, and consequently there are more collisions and thus more damage in the top of the specimens.

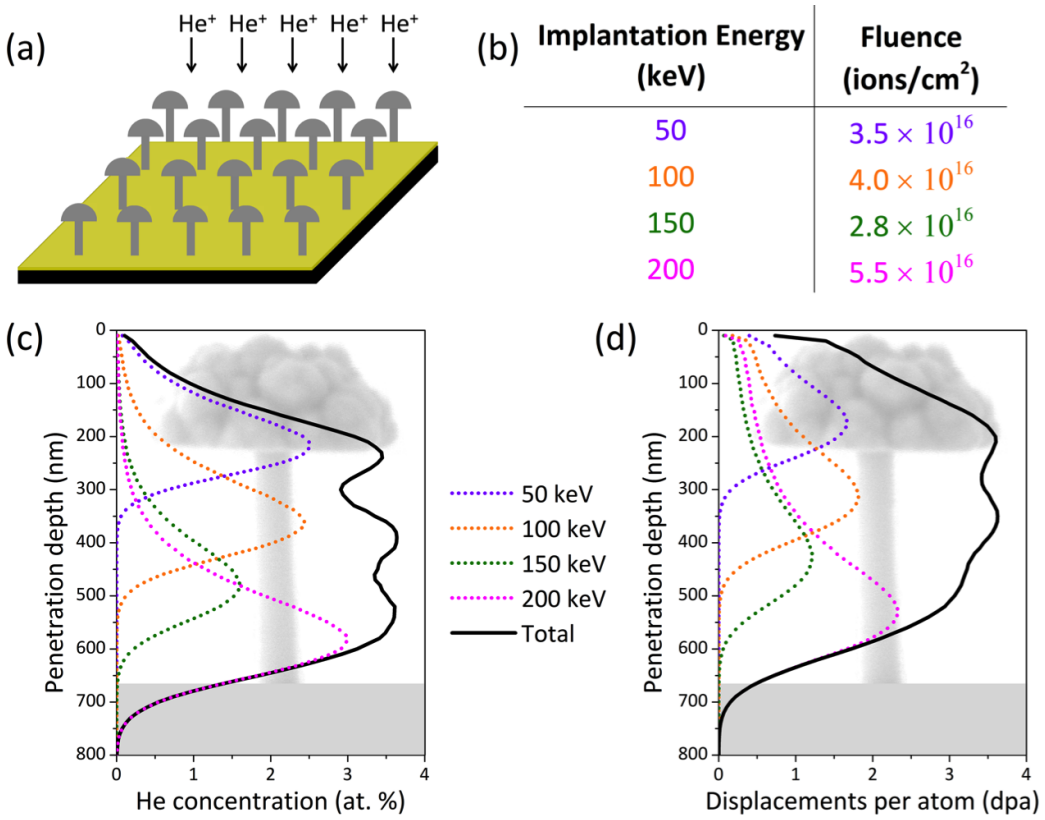

Figure 10. Helium implantation of $Ni_{73}P_{27}$ nanopillars. (a) Schematic of implantation direction. (b) Helium implantation conditions. (c) Helium concentration and (d) displacements per atom profiles as calculated by SRIM for each implantation energy (dashed lines) and the total sum (solid line) from all energies, overlaid on a typical specimen geometry.

SRIM calculations estimated the damage to be 3.00 ± 0.78 dpa and the helium concentration to be 3.18 ± 0.49 at. %, at penetration depths of 150 to 650 nm, which are dimensions corresponding to the length of a typical nanopillar. Helium penetration depths of less than ~150 nm are located above than the nanopillar in the "mushroom cap" and penetration depths greater than ~650 nm are in the underlying Au substrate. Since SRIM assumes the He^+ ions are entering a material that is infinite in lateral dimensions, it likely overestimates the helium concentration and dpa for our ~130 nm nanopillar specimens as the limited lateral dimensions of such specimens allow some of the incoming He^+ ions to escape from the external nanopillar surfaces.

2.4. Microstructural characterization

Figure 11 displays characterization of the as-fabricated and helium-implanted nanopillars. SEM images of representative individual tensile nanopillars are shown in Figure 11 (a) for the as-fabricated sample and Figure 11 (f) for the helium-implanted sample. These images reveal that the helium-implanted specimens have a smoother exterior than the as-fabricated specimens, with no noticeable swelling, blistering, or flaking occurring as a result of the implantation. An increase in the smoothness of specimen surfaces upon helium implantation agrees with earlier work reporting a decrease in surface roughness upon ion bombardments [86-88]. The lack of any noticeable swelling, blistering, or flaking in the helium-implanted specimens is consistent with studies on helium implantation in bulk metallic glasses, in which these morphological changes were observed only at radiation levels above an extremely high critical fluence of 10^{17} - 10^{18} ions cm^{-2} [89-94]. Based on these studies, it is likely that the ~10^{16} ions cm^{-2} fluence used in the current work is below the critical fluence necessary for blistering in $Ni_{73}P_{27}$.

The chemical composition of the samples was analyzed using energy-dispersive x-ray spectroscopy (EDS). EDS was conducted in an SEM (Nova 200 Nanolab, FEI Co.) at 4 keV on five as-fabricated and five helium-implanted nanopillars randomly chosen from different regions on the samples. EDS analysis shown in Figure 11 (b, g) reveals that both the as-fabricated and helium-implanted samples contain ratios of Ni to P corresponding to a chemical composition of ~73 at. % Ni and ~27 at. % P. As measured by EDS, the only significant difference in chemical composition between the two samples was that the helium-implanted sample had nearly twice the amount of carbon and oxygen as the as-fabricated sample; any difference in helium concentration is indiscernible by EDS because helium is too light for detection. The presence of carbon and oxygen in both samples may be caused by exposure to air, residual solvent used to strip the PMMA, or small amounts of un-removed PMMA. The helium-implanted sample likely contains more carbon and oxygen due to carbon and oxygen exposure in the ion accelerator and increased exposure to air during transport to ion beam facilities (the as-fabricated sample was stored in a N_2 environment). These carbon and oxygen impurities do not form a continuous layer on the specimen surfaces and thus do not bear load, which renders their effect on mechanical properties negligible. Further, the EDS results over-represent the amount of carbon and oxygen present because this technique is more sensitive to surface atoms, and the amount of carbon and oxygen is highest at the sample surfaces.

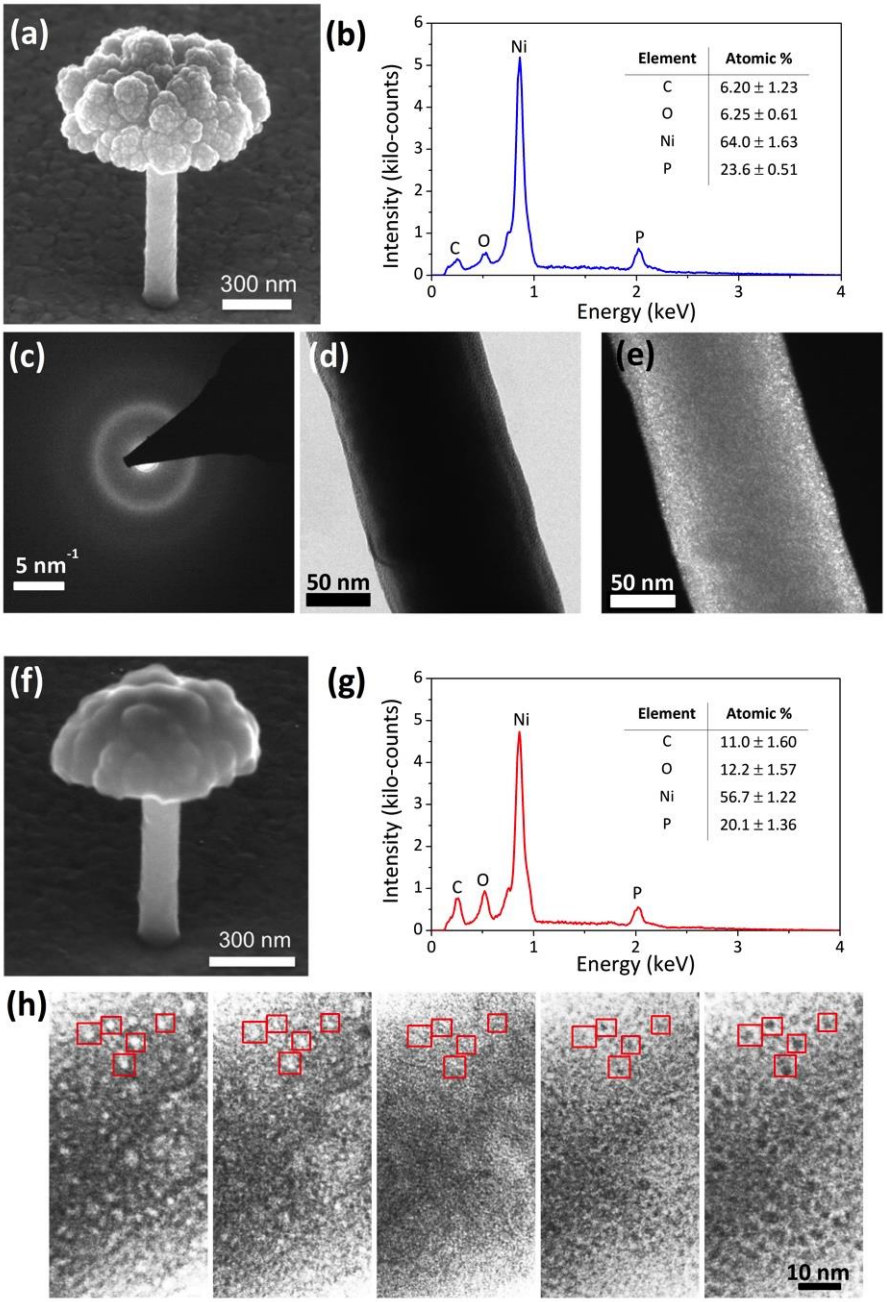

Figure 11. Sample characterization of $Ni_{73}P_{27}$ metallic glass nanopillars. Grouped by (a-e) as-fabricated and (f-h) helium-implanted samples. SEM images of typical (a) as-fabricated and (f) He-implanted $Ni_{73}P_{27}$ specimen. EDS spectra from a typical (b) as-fabricated and (g) He-implanted $Ni_{73}P_{27}$ specimen. Inset tables in top right corners shows chemical composition obtained from five representative (b) as-fabricated and (g) He-implanted $Ni_{73}P_{27}$ nanopillars. (c) Diffraction pattern, (d) bright-field, and (e) dark-field TEM images on an as-fabricated $Ni_{73}P_{27}$ nanopillars. (h) A through-focal TEM series on a representative He-implanted $Ni_{73}P_{27}$ nanopillar with defocus values spanning −2 μm, −1 μm, 0, +1 μm, and +2 μm, from left to right, with example bubbles surrounded by red squares to guide the eye.

The microstructure of the nanopillars was examined using a TEM operating at 200 keV and 300 keV (TF20 and TF30, FEI Co.), and nanopillars were prepared for TEM analysis by two methods, both of which avoided the use of FIB so as to prevent extraneous Ga^+ ion irradiation. The first TEM sample preparation method involved moving individual nanopillars from the Au substrate to a Cu TEM grid (Ted Pella) by attaching a nanomanipulator needle (OmniProbe 200, Oxford Instruments) inside an SEM (Nova 600 Nanolab, FEI Co.) to the "mushroom cap" of a specimen using electrostatic forces and then transferring that specimen to the TEM grid also with only electrostatic forces. Once on the grid, a small amount of W was deposited onto the nanopillar's "mushroom cap" with the electron-beam in an SEM (Nova 200 Nanolab, FEI Co.) to secure the specimen to the TEM grid. The second TEM sample preparation method involved physically rubbing a TEM grid containing a holey carbon film (Ted Pella) on the surface of the substrates to cause some specimens to attach to the carbon film. After rubbing, the TEM grid was examined by SEM to find appropriately placed nanopillars located over holes in the carbon film. Nanopillars positioned in this way could be imaged without interference from the carbon film. These two TEM sample preparation methods were complimentary as the first method allowed selectivity in choosing nanopillars for TEM analysis and the second method allowed picking up many nanopillars simultaneously to conduct "brute-force" TEM and ensure that the microstructure observed in specimens prepared by the first method was representative across many specimens. To visualize the helium bubbles, a common technique for studying radiation damage with TEM is through focus imaging [95], which was used to view the helium bubbles by taking a through-focal series of images on the helium-implanted nanopillars at defocus values of -2 μm, -1 μm, 0, +1 μm, and +2 μm.

TEM analysis is shown in Figure 11 (c-e) for the as-fabricated specimens and Figure 11 (h) and Figure 12 for the helium-implanted specimens. Both specimen types have diffuse ring

electron diffraction patterns, which confirm the amorphous microstructure of the nanopillars. The amorphous microstructure was further corroborated by the featureless and uniform contrast bright-field and dark-field TEM images shown for the as-fabricated nanopillars in Figure 11 (c, d). Similar featureless and uniform contrast bright-field and dark-field images were obtained for the helium-implanted sample as well, and are included in Figure 12. These images verify that unlike the crystallization observed in other irradiated metallic glasses [70,96,97], the current specimens maintained an amorphous microstructure during helium implantation. Multiple helium bubbles are visible in the through-focal TEM images shown in Figure 11 (h), with the bubbles appearing lighter in the under-focused images and darker in the over-focused images. From the through-focal images, the average helium bubble diameter was measured to be 2.25 ± 0.85 nm. Several through-focal series of images were taken both at different locations within the same nanopillar and on multiple nanopillars, with no significant changes in the apparent bubble size and distribution from location to location or from cylinder to cylinder. This consistency of the through-focal images suggests that the helium implantation did indeed result in a relatively uniform distribution and concentration of helium, as expected based on the SRIM-calculated uniform helium concentration.

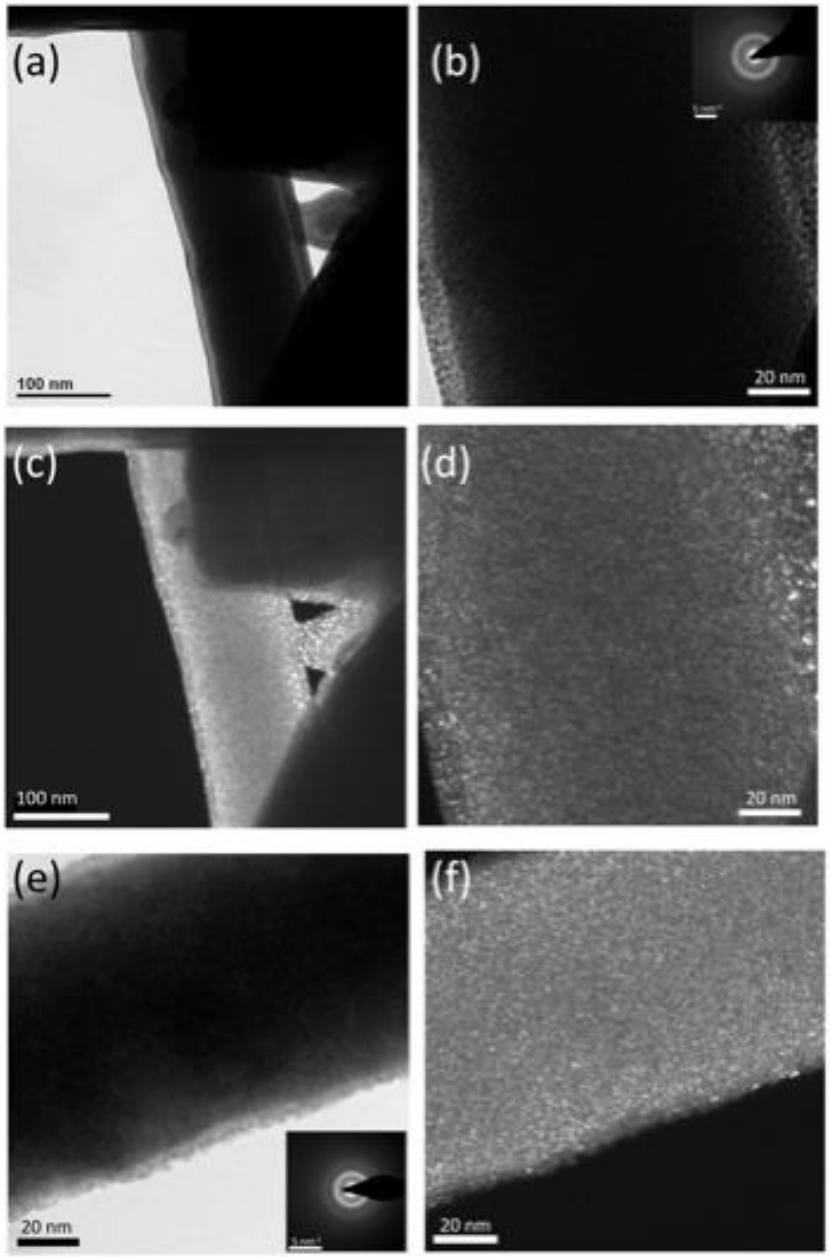

Figure 12. He-implanted nanopillar TEM analysis on two individual specimens. The first specimen is shown in (a-d) and the second specimen is shown in (e, f). (a) bright field image of entire nanopillar (center of image) on TEM grid (right side of image). (b) bright field image at higher magnification near center of nanopillar with inset diffraction pattern. (c) dark field image of entire nanopillar (center of image) on TEM grid (right side of image). (d) dark field image at higher magnification near center of nanopillar. Similar (e) bright field and (f) dark-field image are provided from another He-implanted specimen for further corroboration. The brighter spots on edges of the specimen in (d) and (f) indicative of crystallites present in the deposited W glue used to secure the specimen to the TEM grid.

2.5. Uniaxial tension experiments

In-situ uniaxial tensile experiments on individual metallic glass nanopillars were conducted at a constant nominal strain rate of 1×10^{-3} s^{-1} to the point of failure in the InSEM, a combined SEM (Quanta SEM, FEI Co.) and nanoindenter (Nanomechanics, Inc.). The nanoindenter arm was fitted with a boron-doped diamond tensile grip. After accounting for response from the load frame, support spring, and substrate compliances, the raw load and displacement due to deformation of the specimen were recorded. Using load-displacement data, engineering stresses and strains were calculated using the initial nanopillar diameter and gauge length and by assuming homogeneous deformation. Elastic modulus was calculated from the slope of the loading curve, using stress-strain data from the initial loading until yielding occurred. The yield point was determined by visually inspecting the data for the first deviation from linear elastic loading and the yield stress was defined as the stress at this yield point.

The InSEM system (Nanomechanics, Inc.) used has a load resolution of 3 nN and a displacement resolution of 0.0002 nm. In-situ SEM tensile testing also allowed the identification of tests with noticeable bending of the nanopillar or tilting of the nanopillar "mushroom-cap". These tests were then discarded as unreliable. In addition, only tests where fracture occurred in the gauge section of the nanopillar were used; tests where the sample fractured at the Au substrate or at the top of the gauge section near the nanopillar's "mushroom cap" were discarded. Such tests, where fracture occurred near the very top or bottom of the nanopillar, had noticeably lower strength, indicating those tests merely tested the strength of adhesion to the substrate or a reduced failure strength due to stress concentrated at the joint between "mushroom cap" and cylinder, and not actual strength of the nanopillar gauge section.

Figure 13 contains tensile engineering stress versus strain data for five as-fabricated and five helium-implanted samples. Representative videos obtained during tensile experiments are

included in the supplementary files for as-fabricated (Video 1) and helium-implanted (Video 2) nanopillars. As shown in Figure 13, helium implantation appears to lower the elastic modulus, which was measured to be 47.9 ± 5.20 GPa for the as-fabricated specimens and 38.2 ± 5.25 GPa for the helium-implanted specimens. This decrease in modulus upon helium implantation may be due to the fact that the helium-implanted specimens contain ~3.2 at. % helium and thus have a higher porosity. A relation between elastic modulus, (E), porosity (ϕ), and elastic modulus of the non-porous monolithic material (E_0) was developed by Lu et al. [98],

$$E = E_0(1 - 2\phi)(1 + 4\phi^2) \tag{8}$$

Using equation (8) with the elastic moduli obtained from the slope of linear elastic loading in our experiments, E_0 = 47.9 GPa and E = 38.2 GPa , results in a porosity of ϕ = 0.125, which is higher than anticipated based on the lack of any measurable volume change in the nanopillars upon helium implantation. This seeming discrepancy in modulus is not unreasonable because uniaxial tension experiments at the nanoscale often have significant variability in measured moduli data especially when the moduli are measured from the loading portions of the nanomechanical data [99-101]. Several factors can affect the apparent elastic modulus obtained via nanomechanical testing, including slight misalignments between tension grips and sample, roughness or imperfections on the sample and tensile grip surfaces, substrate effects, and machine compliance. To obtain more accurate results, instead of using the raw data of the measured displacement signal, frames from the in-situ SEM videos were examined to determine the actual displacement. This technique allows for more reliable strain data and has been used successfully in many publications [24,77,99]. The relation by Lu et al. equation (8) is qualitatively useful for illustrating the general trend of elastic modulus decreasing with porosity but should not be used for precise quantification of porosity.

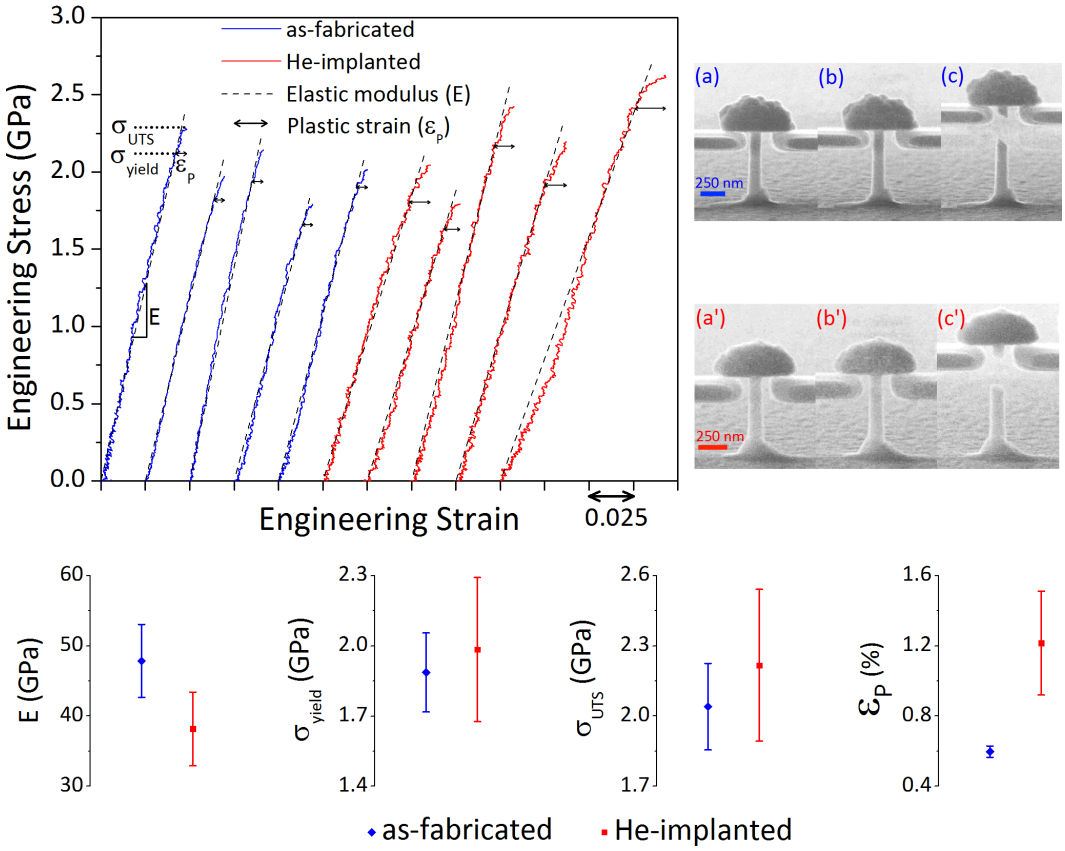

Figure 13. Mechanical behavior of as-fabricated and He-implanted samples under tension. Top right: video stills from in situ SEM for (a-c) as-fabricated and (a'-c') He-implanted samples during (a, a') initial contact between grip and sample, (b, b') just before failure, and (c, c') after failure. Top left: engineering stress−strain for as-fabricated and helium-implanted samples. Bottom: elastic modulus (E), yield strength (σ_{yield}), ultimate tensile strength (σ_{UTS}), and plastic strain (ε_p) for both sample types.

All specimens broke within the nanopillar at a ~45° angle with respect to the substrate (images of fracture surfaces are included in Figure 14), which indicates that both as-fabricated and helium-implanted specimens failed by a similar mechanism of shear banding without significant necking. Prior to failure, the specimens underwent some plastic deformation, which was quantified by measuring plastic strain (ε_p), defined as the total strain at fracture (ε_f) less the strain at the yield point (ε_y), that is, $\varepsilon_p = \varepsilon_f - \varepsilon_y$. Helium-implanted specimens were on average capable of withstanding around two times greater plastic strain before failure (ε_p = 1.215 ± 0.296 %) as compared with the as fabricated specimens (ε_p = 0.598 ± 0.032 %). The

yield strength (σ_{yield}) and ultimate tensile strength (σ_{UTS}) for both specimen types were similar, at 1.89 ± 0.169 GPa and 2.04 ± 0.185 GPa for the as-fabricated specimens and 1.98 ± 0.307 GPa and 2.21 ± 0.324 GPa for the helium-implanted specimens. The similarity in the strengths between helium-implanted and as-fabricated samples suggests that helium implantation did not alter the failure mechanism. In summary, these tensile tests revealed that implanting He^+ into $Ni_{73}P_{27}$ metallic glass nanopillars increases ductility by a factor of two without a sacrifice in strength.

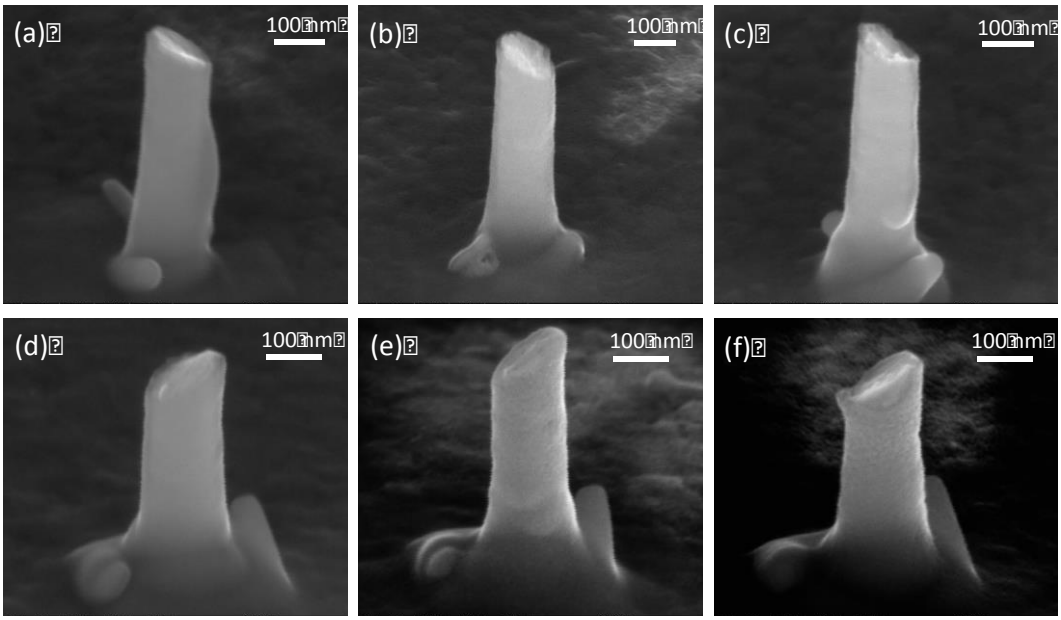

Figure 14. SEM images of the nanopillar fracture surfaces after tensile testing. Images are grouped for (a-c) as-fabricated and (d-e) He-implanted specimens. All specimens failed at a ~45° angle with respect to the loading axis indicating a similar shear-banding failure mechanism in both as-fabricated and He-implanted specimens.

2.6. Discussion

The mechanical results imply that instead of being a detriment, irradiation may actually enhance ductility in metallic glasses. This is the opposite trend seen in irradiation on crystalline metals and alloys, where the large body of literature indicates irradiation leads to embrittlement [27,28,34,73,75]. The substantial difference in mechanical response upon irradiation between

crystalline materials and metallic glasses likely arises from the disordered microstructure of metallic glasses, which undergo deformation by atomic rearrangements within ~100 atom-sized regions, often called shear transformation zones (STZs) [102,103], instead of the dislocation-motion inherent to plasticity of crystalline materials. Deformation in metallic glasses occurs by collective rearrangements and coalescence of multiple STZs. At yield stress, some STZs coalesce to form large planar bands, known as shear bands [14]. The formation and propagation of shear bands are localized events that depend upon the distribution of STZs. As such, a more uniform distribution of STZs is better able to accommodate applied strain without failure before the STZs coalesce and form a catastrophic shear band. During helium implantation, the incoming He^+ ions knock the metallic glass atoms from their native positions. For the implantation conditions used in this work, corresponding to a SRIM-calculated damage of 3.00 ± 0.78 dpa, the metallic glass atoms underwent a significant number of knock-on events. These knock-on events likely disrupted the local icosahedral symmetries between metallic glass atoms, which generated additional free volume within the metallic glass, and facilitated a more uniform distribution of STZs. As discussed by others [24,25], irradiation shifts native metallic glass atoms away from equilibrium and propels them to higher potential energy states, thereby lowering the activation energy for atomic rearrangements and lending greater probability to non-catastrophic plastic deformation. This line of reasoning is consistent with the observed ~2-fold increase in plastic strain of the helium-implanted specimens compared with the as-fabricated specimens. Based on this reasoning, the potential energy landscape in the as-fabricated metallic glass samples is closer to equilibrium, where diffuse local atomic activity and plastic deformation is inhibited. We speculate that compared to the helium-implanted specimens, the as-fabricated specimens contain a more localized free volume and heterogeneous distribution of STZs that more readily coalesce into shear bands.

These arguments are consistent with previous studies that have reported a deformability enhancement in metallic glass nanostructures as a result of FIB-induced Ga^+ ion bombardments. Magagnosc et al. found that Ga^+ ion irradiation caused originally brittle $Pt_{57.5}Cu_{14.7}Ni_{5.3}P_{22.5}$ nanowires to exhibit tensile ductility, with up to 2% post yielding strains [23]. Chen et al. found that Ga^+ ion bombardment into the surface of $Ni_{80}P_{20}$ nanopillars led to a 3-fold increase in plastic strain [24]. The difference in the extent of irradiation-induced increase in plastic strain between Chen et al. (3-fold increase) [24] and the current work (2-fold increase) may arise from slight differences in the composition of the constituent Ni-P metallic glass and the dissimilar nature of the irradiating ions. The experiments of Chen et al. involved bombardment with Ga^+ ions, which have limited penetration due to the large size of the Ga^+ ions and relatively low FIB energies used. In contrast, samples of the current work were implanted with He^+, which resulted in a distribution of high-pressure helium bubbles throughout the volume of the nanopillars.

At equilibrium, the pressure of helium gas inside a bubble is balanced by surface tension, and thus to estimate the pressure difference between the inside and outside of a spherical bubble we use the well-known Laplace pressure relationship,

$$\Delta P = P_{inside} - P_{outside} = \frac{2\gamma}{r_{bubble}} \tag{9}$$

where γ is the surface energy of the surrounding material and r_{bubble} is the bubble radius. For $Ni_{73}P_{27}$ metallic glass, γ was measured to be 3 J/m^2 using contact angle goniometry and the bubble radius from the TEM images was ~1 nm, which results in a pressure difference of ΔP~6 GPa between the inside of the bubble and the surrounding $Ni_{73}P_{27}$. The presence of such high-pressure helium bubbles likely reduces the free volume available for plastic deformation and thus the extent of ductility brought about by displacements from He^+ ion bombardments. This suggests that helium implantation leads to two competing effects on

metallic glass ductility: (1) bombardments from incoming He^+ ions enhances ductility by increasing free volume in the metallic glass, and (2) the presence of helium segregated into high-pressure bubbles reduces ductility by decreasing free volume in the metallic glass. The dominant effect depends on how the displacements per atom (a measure of bombardments) compare with the implanted helium concentration. The increased ductility observed in the current work suggests that the effect of bombardments dominates for the implantation conditions used, which correspond to SRIM-calculated dpa of 3.00 ± 0.78 and helium concentration of 3.18 ± 0.49 at. %.

2.7. Outlook

This work discussed in this chapter demonstrates a promising new pathway for developing materials that can maintain and even improve their mechanical properties in irradiation-intensive environments. By utilizing an electroplating-based nanofabrication technique we created isolated tensile metallic glass nanostructures without the use of focused-ion beam irradiation. We then utilized an ion accelerator to uniformly implant helium throughout the samples at a concentration of 3.2 at. % with resultant damage of ~3 dpa. In-situ uniaxial tensile tests on the as-fabricated ~130 nm diameter $Ni_{73}P_{27}$ metallic glass nanostructures and on identical helium-implanted ones indicate that helium implantation enhanced post-elastic deformability by a factor of two without any sacrifice in strength. The absence of dramatic changes in mechanical properties upon helium implantation suggests that the small ~2 nm sized helium bubbles produced as a result of the helium implantation in this study were not large enough to serve as sufficient stress concentrators, thus the mechanical response of the helium-implanted nanopillars did not transition to the regime where stress-concentrating helium bubbles would act as flaws that induce failure.

Our work suggests that metallic glasses may respond to helium irradiation in a beneficial way, a finding diametrically opposite to the behavior of crystalline metals and alloys, for which irradiation has been widely reported to induce hardening, embrittlement, catastrophic failure, and dramatic changes in mechanical properties. For example, in a study where 3 at. % He was implanted into pure Ni at room temperature under conditions similar to those used in this work, the hardness increased from 1.1 GPa to 5.8 GPa [104]. The results of the current work are even more promising because the amount of helium implanted, 3.2 at. %, is over an order of magnitude larger than what a nuclear reactor would typically experience (typically 0.2 at. % for fusion reactors) [73]. Consequently, the improvement in mechanical properties of the studied metallic glass system upon very high levels of helium implantation suggests that metallic glasses may be particularly well suited for irradiation-intensive applications, involving high levels of implanted ions. Caution should be taken because a significant limitation of metallic glasses may be their glass transition temperature (T_g), which restricts their use to applications below T_g in order to prevent crystallization.

Chapter 3. Substantial tensile ductility in sputtered Zr-Ni-Al nano-sized metallic glass

Adapted with permission from:

R. Liontas, M.J. Zadeh, Q. Zeng, Y. Zhang, W.L. Mao, J.R. Greer. "Substantial tensile ductility in sputtered Zr-Ni-Al nano-sized metallic glass" *Acta Materialia*. 118 (2016) 270-285. DOI: 10.1016/j.actamat.2016.07.050

This chapter describes investigation into the mechanical behavior and atomic-level structure of glassy Zr-Ni-Al nano-tensile specimens with widths between 75 and 215 nm. Studies were focused on nano-tensile specimens in two different energy states: (1) as-sputtered and (2) sputtered followed by annealing below the glass transition temperature. Tensile experiments conducted inside a scanning electron microscope reveal substantial tensile ductility in some cases reaching >10% engineering plastic strains, >150% true plastic strains, and necking down to a point during tensile straining in specimens as wide as ~150 nm. We found the extent of ductility depends on both the specimen size and the annealing conditions. Using molecular dynamics simulations, transmission electron microscopy, and synchrotron x-ray diffraction, we explain the observed mechanical behavior through changes in free volume as well as short- and medium- range atomic-level order that occur upon annealing. This work demonstrates the importance of carefully choosing the metallic glass fabrication method and post-processing conditions for achieving a certain atomic-level structure and free volume within the metallic glass, which then determine the overall mechanical response. An important implication is that sputter deposition may be a particularly promising technique for producing thin coatings of metallic glasses with significant ductility, due to the high level of disorder imparted by the sputtering process.

3.1. Motivation

We chose Zr-Ni-Al as our model metallic glass because of its oxidation resistance [105,106] and excellent glass-forming ability [107,108]. The high glass transition temperature (T_g) of Zr-Ni-Al metallic glass, reported to range from 680 to 760 K depending on composition [109], increases the applicability of this metallic glass to extreme environments, such as those involving elevated temperatures and radiation, with a lower risk of crystallization or oxidation. The Zr-Ni-Al system contains only metallic components, which renders it a more representative metallic glass with true metallic bonding, as opposed to a system containing metalloid components with some covalent bonding. The properties of metal-metal systems are much better understood than those of metal-metalloid systems, whose covalent interatomic bonds influence glass formation and make modeling such systems difficult [110]. With only three component elements, this system is also practical for conducting molecular dynamics (MD) simulations. The shortage of literature on mechanical properties and detailed structural analysis of sputtered Zr-Ni-Al metallic glass motivated us to undertake a fundamental study of its mechanical behavior and atomic-level structure. The microstructure was analyzed by transmission electron microscopy (TEM) and synchrotron X-ray diffraction (XRD) to elucidate the unique atomic arrangement brought about by forming this metallic glass via sputtering and the changes in this structure that occur as a result of subsequent annealing. Mechanical behavior was assessed by conducting in-situ uniaxial tension and compression experiments. MD simulations were conducted to explore the effect of metallic glass fabrication conditions, sub-T_g annealing, and sample size.

3.2. Methods

3.2.1. Fabrication of Zr-Ni-Al nano-tensile specimens

All samples in this study were fabricated from a sputtered Zr-Ni-Al metallic glass thin film. We deposit this material by sputtering an alloyed $Zr_{56}Ni_{22}Al_{22}$ target (ACI Alloys, Inc.) with a base pressure less than 1×10^{-6} Torr using a DC power supply at 100 W with resultant voltage of 320-390 V, under 3 mTorr argon in a magnetron sputter deposition system (ATC Orion sputtering system, AJA International, Inc.). The sputtering process produces an amorphous Zr-Ni-Al film, which is the starting point for the fabrication of nano-tensile specimens. Samples were fabricated from two different amorphous states of this metallic glass: (1) as-sputtered and (2) sputtered then annealed at the sub-T_g temperature of 625 K for 24 hours. For the as-sputtered state, specimens were fabricated by sputtering Zr-Ni-Al directly onto a silicon TEM grid (PELCO FIB Lift-Out TEM grid, Ted Pella) to a minimum thickness of 3 μm as shown in Figure 15 Step (1, 2) and then using XeF_2 gas from the insulator enhanced etching system in a SEM to selectively etch away the silicon substrate underneath the sputtered Zr-Ni-Al (Figure 15 Step (3)). In this step, a fine needle was positioned close to the sample surface to create a high local flux of XeF_2 gas while the ion beam was used to induce reactions between the XeF_2 gas and the scanned area. As such, significant etching of the Zr-Ni-Al metallic glass was prevented not only by the chemical selectivity of XeF_2 for Si but also by physically selecting only Si as the scanned area in the SEM. This resulted in the creation of a free-standing Zr-Ni-Al film directly on the TEM grid, which was then FIB-milled into the desired geometry of nano-tensile specimens shown in the insets of Figure 15 Step (4). The FIB-milling step in the specimen fabrication required extensive tilting and rotating of the SEM stage to achieve the desired removal of material. A schematic of this process is shown in Figure 15. This methodology allowed fabrication of the specimens directly on the TEM grid, which facilitated the TEM analysis after tension experiments. The resultant specimens contained test-

sections that were approximately square in cross-section with rounded corners. Specimens of this as-sputtered metallic glass were fabricated with widths ranging from 85 – 215 nm and heights correspond to an aspect ratio of ~1:10.

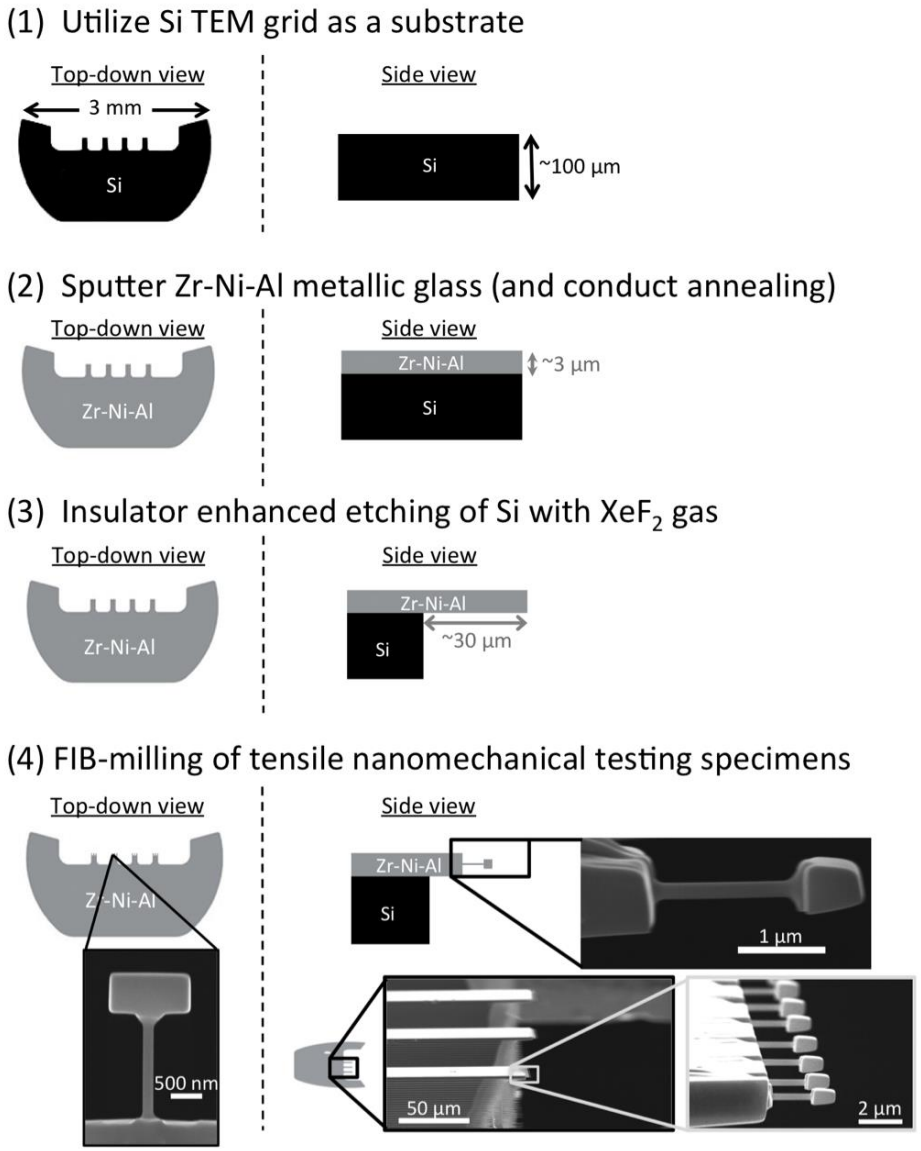

Figure 15. Fabrication process for sputtered nano-tensile specimens. (1) A commercially available Si TEM grid is used as the substrate, (2) Zr-Ni-Al metallic glass is sputtered onto the TEM grid, with annealing conducted under an Ar environment in a tube furnace, (3) insulator enhanced etching of Si with XeF_2 gas in an SEM used to selectively remove Si from the top section of the posts on the TEM grid, (4) the resultant free-standing film of Zr-Ni-Al on the posts of the TEM grid, FIB-milled into individual nano-tensile specimens by extensively tilting/rotating the SEM stage to allow the appropriate FIB-removal of material. SEM images of the nanomechanical testing specimens are shown from both top-down and side view at ~5° tilt.

To fabricate specimens in the annealed state, the TEM grid with the ~3 μm-thick sputter-deposited Zr-Ni-Al film was annealed in a Carbolite tube furnace (in between Steps (2) and (3) of Figure 15). Prior to raising the temperature of the furnace, argon was flowed through the tube furnace at a rate of 3 liters per minute for 1 hour to avoid sample oxidation; this flow rate was maintained during the entire annealing process. The temperature of the tube furnace was increased from room temperature to the annealing temperature of 625 K at a rate of 45 K min^{-1} and then held at the annealing temperature for 24 hours. From literature, the T_g of $Zr_{55}Ni_{25}Al_{20}$ is 757.1 K [109], which means the annealing temperature of 625 K roughly corresponds to 80% of T_g. After the 24-hour annealing period, the furnace was turned off and allowed to reach room temperature before stopping the argon flow and removing the sample. Following annealing, nano-tensile specimens were fabricated using an identical FIB-milling process as the ones made from the as-sputtered state, with similar sizes of 79 – 209 nm, and the aspect ratio of ~1:10. Potential oxidation induced by the annealing was prevented by conducting the annealing in an argon environment. FIB-milling the specimens from a larger film of annealed Zr-Ni-Al metallic glass provided substantial oxidation protection as any surface oxide layers that may have formed during annealing were removed by FIB, and the resultant specimen test-section consists of material at a distance greater than 1μm from the surfaces exposed to the annealing environment.

3.2.2. TEM sample preparation and conditions

TEM samples were prepared with the Ga^+ FIB following standard lamella preparation techniques and by fabricating the nano-tensile specimens directly onto the TEM grid (Figure 15). The FEI Technai TF20 transmission electron microscope was operated at 200 keV to obtain bright field and dark field images, diffraction patterns, high-resolution TEM images, and to conduct energy dispersive X-ray spectroscopy (EDS) in STEM mode. To assess any

changes in the atomic structure as a result of tension experiments, some nano-tensile specimens were left untested; the microstructure in both types of specimens, mechanically strained and as-fabricated, was examined by TEM. To analyze the overall sample composition and phase homogeneity, we fabricated the lamella lift-out sample from a Zr-Ni-Al film that had been sputtered for ~20 hours to a thickness of ~4.5 μm. EDS was conducted at several points along the depth of the film to determine whether there were any changes in the chemical composition with sputter deposition time.

3.2.3. In-situ uniaxial tension experimental setup

Uniaxial tensile experiments were performed in-situ inside an SEM to allow simultaneous visualization of deformation and measurement of load and displacement during tensing. Tensile experiments were conducted using the Hysitron PI-85 nanomechanical module in an SEM (FEI, Versa 3D). Tensile grips were fabricated by FIB-milling boron-doped diamond into a grip shape, shown in Figure 18 (a-d) and Figure 19 (a-d). To perform a tension experiment, a nano-tensile specimen was moved inside the tension grips and then a displacement-controlled uniaxial tension experiment was conducted at a strain rate of 1×10^{-3} s^{-1} until the point of failure. Load-displacement data was acquired at a rate of 200 data points per second; to display representative data points, the data was smoothed with a span containing data over the nearest 2 nm of the displacement, using the rlowess method in MATLAB, which involves a robust local regression using weighted linear least squares and a first degree polynomial model.

Load-displacement data was converted to stress and strain by measuring the relative dimensional changes throughout the experiments in each individual specimen. Engineering stresses and strains were calculated by utilizing the initial specimen height and cross-sectional area obtained from measurement of specimen height and width in SEM images taken prior to

tensile experiments. True stresses and strains were calculated using the instantaneous specimen height and cross-sectional area during the tension experiment. To obtain these instantaneous specimen dimensions, we assumed that necking began at the maximum load during the tension experiment, and the criterion for necking was the presence of any stress-strain data beyond the maximum stress. We assumed that prior to necking the gauge length deformed uniformly according to

$$\sigma_T = \sigma_E(1 + \varepsilon_E) \tag{10}$$

$$\varepsilon_T = \ln(1 + \varepsilon_E) \tag{11}$$

where σ_T is true stress, σ_E is engineering stress, ε_E is engineering strain, and ε_T is true strain. To account for the large localization of deformation in the necked region that occurs upon necking, true stress-strain data was calculated after necking according to

$$\sigma_T = \frac{F}{A_{neck}} \tag{12}$$

$$\varepsilon_T = \ln\left(\frac{A_0}{A_{neck}}\right) \tag{13}$$

where F is the load measured during the tension experiment, A_{neck} is the cross-sectional area of the thinnest portion of the necked region, and A_0 is the initial cross-sectional area of the specimen. The width of the neck region (w_{neck}) was measured at approximately 10 load-displacement points during necking. Due to the roughly square cross-sectional area of the specimens, the cross-sectional area of the necked region (A_{neck}) was calculated from measured w_{neck} as w_{neck}^2 and A_{neck} was assumed to vary linearly between each measurement point.

Engineering stresses and strains were used to calculate the elastic modulus (E), yield strain ($\varepsilon_{y,engineering}$), yield strength ($\sigma_y$), engineering plastic strain ($\varepsilon_{p,engineering}$), and ultimate tensile strength (UTS). The only mechanical property calculated form the true stress-strain data was the true plastic strain ($\varepsilon_{p,true}$). The elastic modulus was calculated as the slope of the loading curve by conducting a linear fit on the region of the loading curve just after any initial loading

instabilities and just before the yield point. The yield point was determined by visually inspecting the data for the first deviation from linear elastic loading and the yield stress and strain (σ_y and $\varepsilon_{y,engineering}$) were defined as the respective stress and strain at this yield point. The UTS was found as the maximum stress in the engineering stress-strain response of a specimen.

3.2.4. Synchrotron XRD sample preparation and conditions

Synchrotron XRD experiments were conducted on Zr-Ni-Al metallic glass in the same two states as the nanomechanical experiments: (1) as-sputtered and (2) sputtered then annealed at 625 K. To obtain enough material for synchrotron XRD measurements, Zr-Ni-Al was deposited using identical sputter conditions discussed previously with kapton tape as the substrate, which allowed flakes of the sputtered Zr-Ni-Al to be easily removed from the kapton tape and collected for analysis. Synchrotron XRD analysis was conducted on the as-sputtered Zr-Ni-Al flakes and annealed flakes, which were annealed prior to the diffraction measurements using identical annealing conditions discussed previously. Synchrotron XRD was performed in a transmission geometry using the high-intensity, high-energy monochromatic beam at Sector 11-IDC of the Advanced Photon Source at Argonne National Laboratory. The photon energy was 105.1 keV corresponding to an X-ray wavelength of 0.11798 Å and the beam size was 0.5 × 0.5 mm^2. The X-ray attenuation length of the $Zr_{55}Ni_{25}Al_{20}$ sample at 105.1 keV is ~2.5 mm. Zr-Ni-Al flakes were sandwiched between two layers of kapton tape to increase the sample thickness (in this case ~200 μm). A Perkin Elmer area detector was set at a distance of 690.7 mm and CeO_2 was used as the calibration material. The exposure time was 90 s for each sample and the background scattering from air and the two layers of kapton tape. The resultant 2D image files were integrated using the Fit2D program to obtain 1D intensity distributions as a function of the wavevector Q, from which the

structure factor $S(Q)$, and the reduced pair-wise distribution function $G(r)$ were derived using the PDFgetX3 program. The composition was assumed to be $Zr_{55}Ni_{25}Al_{20}$ for data analysis.

3.2.5. Molecular dynamics simulation methodology

MD simulations were conducted on cylindrical Zr-Ni-Al metallic glass specimen using Large-Scale Atomic/Molecular Massively Parallel Simulator (LAMMPS) [111]. The interatomic interactions were calculated by employing the embedded atom model (EAM) potential parameterized for the Zr-Ni-Al-Cu system [112]. To construct the samples, first, a 5 nm cube of the alloy with the atomic composition of $Zr_{55}Ni_{25}Al_{20}$ (in the range of our experiments) and periodic boundary conditions (PBCs) along all three dimensions was melted and equilibrated at 2300 K for 10 ns. Then, the liquid alloy was quenched to 50 K with a given cooling rate (e.g. 10^{10} K/s) at zero external pressure using the isothermal–isobaric (NPT ensemble) ensemble. To control the temperature and pressure of the simulations, Nose-Hoover thermostat and barostat were employed [113]. To integrate the equations of atomic motion, the Verlet algorithm [114] was used with the time step of 0.002 ps during the melting/quenching processes. The cylindrical sample for the uniaxial tensile test with diameter of 40 nm and length of 120 nm was then constructed by replicating the metallic glass cube. We applied PBCs in the direction parallel to the central axis of the cylinder (i.e. z direction), while free boundary conditions were applied in other directions. Before applying the tensile loading, the sample was equilibrated at 300 K (similar to the temperature of our experiments). The uniaxial loading was applied by rescaling the simulation box in the z direction with the strain rate of 4×10^{7} s^{-1}. During the loading procedure, the time step of the Verlet algorithm was set to 0.001 ps. The engineering stress was calculated from the Virial atomic stress tensor [115,116]. As a measure of local (atomistic) deformation during loading, we adopted the atomic von Mises strain [117] and used OVITO package for the visualization [118].

In the MD simulations, we examined the following three factors: cooling rate, annealing condition and sample size. To understand the effect of cooling rate (i.e. the effect of fabrication variables), we constructed the tensile samples using glasses obtained with cooling rates of 10^{10} K/s, 10^{11} K/s, 10^{12} K/s, and 10^{13} K/s. Moreover, to study the effect of sub-T_g annealing (i.e. the effect of post-fabrication variables), the sample constructed with the cooling rate of 10^{13} K/s was annealed for up to 400 ns at 850 K (~ $0.8T_g$), and cooled back to 300 K with the same cooling rate. In addition, to study the size effect, tensile samples with diameters of 5, 10, 20, and 40 nm and the same aspect ratio (i.e. ratio of length to diameter) of 3 were prepared using the glass obtained with the cooling rate of 10^{10} K/s.

To characterize the short range order (SRO) present in the MD simulated samples we utilized the Voronoi tessellation method [119,120], whereby around each atom a Voronoi polyhedron is constructed with a certain number of triangular, quadrangular, pentagonal, and hexagonal faces, depending upon the arrangement of its nearest neighbor atoms. The Voronoi index of each atom corresponds to the number of faces in its surrounding Voronoi polyhedron, for example, a Voronoi index of <0,2,8,1> corresponds to a Voronoi polyhedron with 0 triangular faces, 2 quadrangular faces, 8 pentagonal faces, and 1 hexagonal face. With this notation, a Voronoi index of <0,0,12,0> corresponds to the Voronoi cell with the highest possible local symmetry, that is, a regular dodecahedron with 12 nearest neighbor atoms arranged at the vertices of a full-icosahedron (FI) cluster. As an indicator of SRO, we mainly focus on tracking the concentration of the Al-centered full icosahedron cluster (i.e. Al-FI with the Voronoi index of Al <0,0,12,0>) since this icosahedron configuration is known to be prevalent in a variety of metallic glass systems [121,122]. We chose to focus on the Al-centered icosahedron because we found this particular cluster to be most sensitive to changes in processing conditions, such as annealing and utilizing different cooling rates. The average atomic potential energy of the system is another measure we utilized to assess the overall

ordering in the system since a decrease in atomic potential energy signifies atoms in a more ordered, relaxed state.

3.2.6. Virtues and limitations of MD simulations in small-scale mechanics

It is well-known that the spatial and temporal scales in MD simulations are very different from those in experimental techniques due to the restrictions in the technique and computational resources. The samples in current MD simulations typically contain up to tens of million atoms, which corresponds to a ~40 nm-diameter, 120 nm-tall nanopillar. The typical simulation duration (usually tens of nanoseconds), the cooling rate (as high as 10^{10} K/s and above), and the strain rate (on the order of 10^{7} s^{-1}) are several orders different than those of experiments. These limitations generally prevent a quantitative comparison between simulated and experimental results, which should not be the objective of MD simulations. For example, it has been shown that a higher strain rate in MD simulations often leads to a higher yield strength in materials [123]. Therefore, to interpret simulation results, one should mainly focus on the major mechanistic features and trends in the behavior of the samples. If the simulation and experimental results follow the same trend, it would be plausible to use these simulations to reveal the underlying atomistic mechanisms, which are otherwise not obtainable via experimental techniques [124,125]. Based on these guiding principles, MD simulations have been extensively employed, together with experiments, to reveal valuable insight into complicated mechanical properties and behaviors, such as shear banding, crack initiation/propagation, and elastic buckling in a variety of metallic glass and nanoglass systems [63,124-133].

3.3. Results

3.3.1. TEM microstructure and elemental analysis

TEM images and analysis of as-sputtered and annealed Zr-Ni-Al are presented in Figure 16. The film used for this analysis was sputtered for ~20 hours to a thickness of ~4.5 μm. We confirmed this sample to be amorphous, evidenced by the presence of diffuse rings in the diffraction pattern (Figure 16 (a)), as well as the lack of any observable ordering in the high-resolution TEM image (Figure 16 (b)). Energy-dispersive x-ray spectroscopy (EDS) in the TEM was conducted on the cross-section of the as-sputtered film at various distances away from the substrate to determine the stoichiometric ratio of each component and to assess whether sputtering induced any variations in chemical composition with deposition time. The chemical composition based on the EDS data is plotted in Figure 16 (c) and shows that chemical composition is not a function of distance away from the substrate, which indicates that the sputtering process is consistent over time. The horizontal lines shown in Figure 16 (c) are plotted at the average composition for each element, with the legend displaying these average compositions and the standard deviation in that measurement. This plot implies that less than 2 at. % of carbon and oxygen are present in the thin film lamella sample, with the average stoichiometry of Zr/Ni/Al being $Zr_{55}Ni_{29}Al_{16}$.

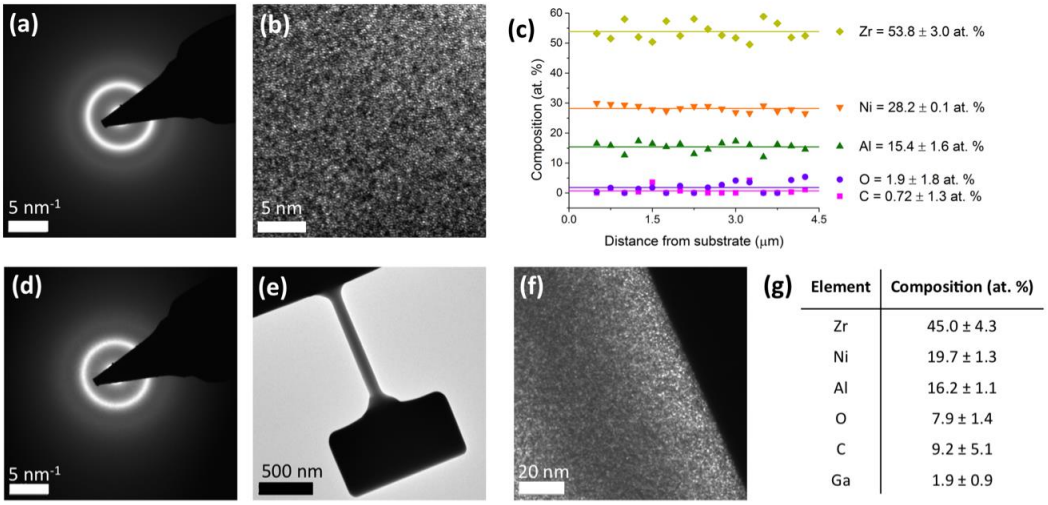

Element	Composition (at. %)
Zr	45.0 ± 4.3
Ni	19.7 ± 1.3
Al	16.2 ± 1.1
O	7.9 ± 1.4
C	9.2 ± 5.1
Ga	1.9 ± 0.9

Figure 16. TEM and EDS elemental analysis on as-sputtered and annealed Zr-Ni-Al metallic glass. Grouped as (a-c) as-sputtered and (d-g) annealed samples, including (a) diffraction pattern from as-sputtered film, (b) high-resolution TEM image of the as-sputtered film, (c) EDS elemental analysis along the depth of the ~4.5 μm thick as-sputtered film, (d) diffraction pattern from test section of the annealed nano-tensile specimen, (e) TEM image of the annealed nano-tensile specimen, (f) dark-field image on the surface edge of the annealed nanomechanical testing specimen, and (g) EDS elemental analysis on annealed nano-tensile specimens with error denoting ± one standard deviation in the measurement.

The microstructure of annealed samples was analyzed by TEM to ensure that crystallization and oxidation had not occurred; these TEM results are shown in Figure 16 (d-g). The TEM image of an entire nanomechanical specimen (Figure 16 (e)) reveals than an amorphous microstructure was retained upon annealing, as evidenced by the diffuse rings in the diffraction pattern (Figure 16 (d)) and the uniform contrast dark-field image (Figure 16 (f)). TEM analysis on post-tension samples indicated no evidence of crystallization upon mechanical deformation and no changes in the amorphous structure observable by TEM. As measured by EDS, the relative amounts of each element after annealing are shown in the chart in Figure 16 (g) and reveal a slightly greater carbon and oxygen content compared with the as-sputtered sample (Figure 16 (c)) with both amounts <10 at. %. This increased carbon and oxygen content stems from extensive SEM imaging during tension experiments and a small surface oxide layer from air exposure. The signal from these surface atoms is amplified for the nano-tensile specimen

because of their high surface-to-volume ratio and the increased sensitivity of EDS to surface atoms. EDS analysis also revealed ~2 at. % Ga present in the annealed specimens, most likely caused by the Ga^+ ions from FIB, with a higher concentration of Ga near the sample surfaces where the ion beam came in direct contact with the sample to remove material. The amount of ~2 at. % Ga is likely an upper bound for the actual amount of Ga present in the sample because EDS is more sensitive to surface atoms. The average stoichiometry of Zr/Ni/Al in the annealed nanomechanical testing specimens corresponds to $Zr_{56}Ni_{24}Al_{20}$ (Figure 16 (g)), which is slightly different than that of the as-sputtered film, which was $Zr_{55}Ni_{29}Al_{16}$ (Figure 16 (c)). This difference in stoichiometry may be caused a slight preference for etching certain elements in the XeF_2 and FIB etching steps. However, as all specimens underwent the same etching procedure, these effects would be consistent among all the nanomechanical testing specimens.

3.3.2. Nanomechanical compression results

In addition to the tensile experiments discussed in detail in this Chapter, we also examined the mechanical properties of the as-sputtered Zr-Ni-Al metallic glass via uniaxial compression experiments on cylindrical nano-compression specimens. Specimen were fabricated by FIB milling of the same ~4.5 μm thick sputtered film analyzed by TEM in Figure 16. The specimens were fabricated with diameters ranging from 225 nm to 1560 nm, and corresponding heights such that the aspect ratio was ~1:3 so as to avoid buckling during compression. The specimens were compressed at a strain rate of 1×10^{-3} s^{-1} using the Hysitron PI-85 nanomechanical testing instrument in-situ in the Versa 3D scanning electron microscope. The resultant compression data is displayed in Figure 17. These specimens exhibited two very distinct regimes of mechanical behavior depending on their size: ductile behavior and homogeneous flow was observed for "small" specimens with initial diameters ≤

555 nm, while shear banding and localized failure was observed for "large" specimens with initial diameters ≥ 890 nm. These differences in mechanical response are apparent from the stress-strain curves, which show uniform plastic loading for the "small" specimens (Figure 17 (a)), and many strain bursts from the catastrophic shear banding events for the "large" specimens (Figure 17 (b)). The post-compression images of the specimens also illustrate the differences in mechanical response with the "small" specimens exhibiting homogeneous deformation near the top of the specimens (Figure 17 (c-d)) and the "large" specimens exhibiting clear shear bands (Figure 17 (e-f)). Overall, the compression data indicates a transition from homogeneous-like flow to shear banding at a specimen diameter between 555 and 890 nm, which is quite a large diameter for observing ductility in metallic glasses.

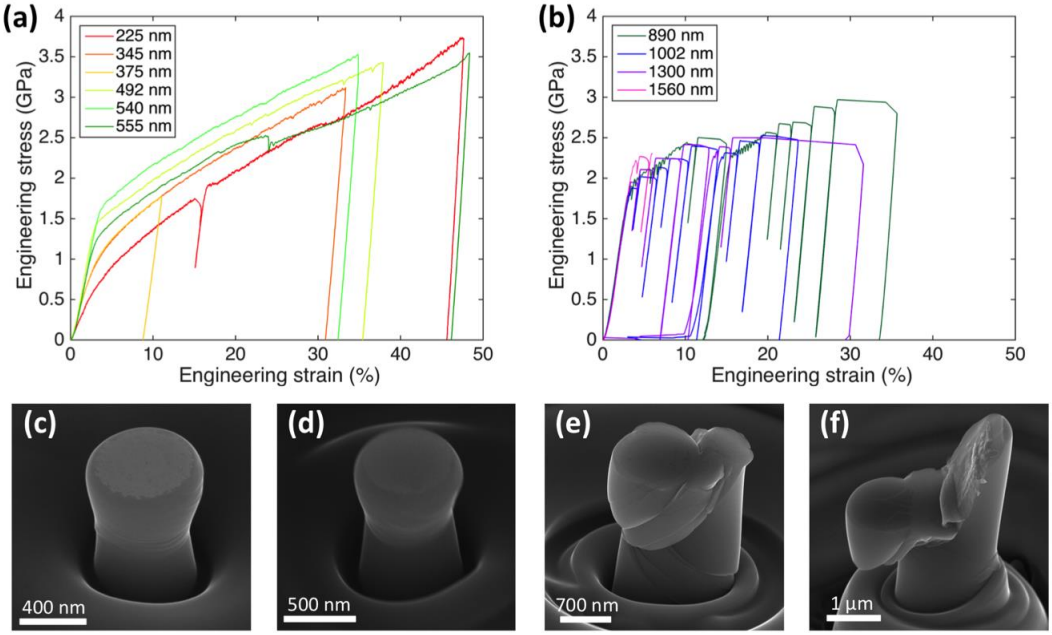

Figure 17. Uniaxial compression experiments on FIB-fabricated Zr-Ni-Al specimens. Engineering stress-strain results on (a) "small" specimens with diameters ≤ 555 nm and (b) "large" specimens with diameters ≥ 890 nm. Post-compression images on specimens with initial diameters of (c) 492 nm, (d) 540 nm, (e) 1300 nm, and (f) 1560 nm.

These promising compression results motivated the more rigorous tensile experiments discussed in this chapter. We chose to focus on tension testing due to some of the inevitable

limitations of compression, such as the lack of a well-defined failure behavior under compression. For example, under tension a specimen will eventually fracture and the amount of plasticity in the stress-strain response can be unambiguously quantified, while such a clear fracture behavior and thus measures of plasticity does not occur under compression. Furthermore, the top-down FIB milling utilized to fabricate the specimen pictured in Figure 17 (c-f) results in tapered samples, which can become especially pronounced as the specimen diameter becomes smaller and makes fabrication of sub-100 nm specimens impossible. This tapering may effect shear band nucleation and make stress analysis difficult. Tension is also of particular interest to metallic glasses because monolithic bulk metallic glasses show no tensile ductility at room temperature but can sometimes exhibit compressive plasticity. Therefore, achieving tensile ductility in a nano-sized metallic glass demonstrates a new mechanical behavior that is completely unattainable in bulk systems of metallic glass.

3.3.3. Nanomechanical tension results

Figure 18 and Figure 19 display the tensile stress-strain response of the as-sputtered and annealed samples arranged by specimen dimensions and grouped into four width categories: ~90 nm, ~110 nm, ~150 nm, and ~200 nm. For each width category, Figure 18 and Figure 19 each show three representative engineering stress-strain curves, one representative true stress-strain curve, and one representative SEM image of a tested specimen around the time of failure. We observed two distinct regimes of mechanical behavior in the as-sputtered: "small" specimens with width categories < ~200 nm failed by pronounced localized necking and reached true strains in excess of 100%. The "large" specimens in the ~200 nm width category failed by shear banding and exhibited marginal ductility. The transition from localized necking (Figure 18 (a-c)) to shear banding (Figure 18 (d)) can be seen in the SEM images of the specimens around the time of failure; this transition is even more apparent from the in-

situ videos of the tensile experiments. For example, the 212 nm-wide as-sputtered sample (Video 3 (a, b)) fails catastrophically via shear banding, and the 114 nm-wide as-sputtered sample (Video 4 (a, b)) shows localized necking with the material drawing down to a point.

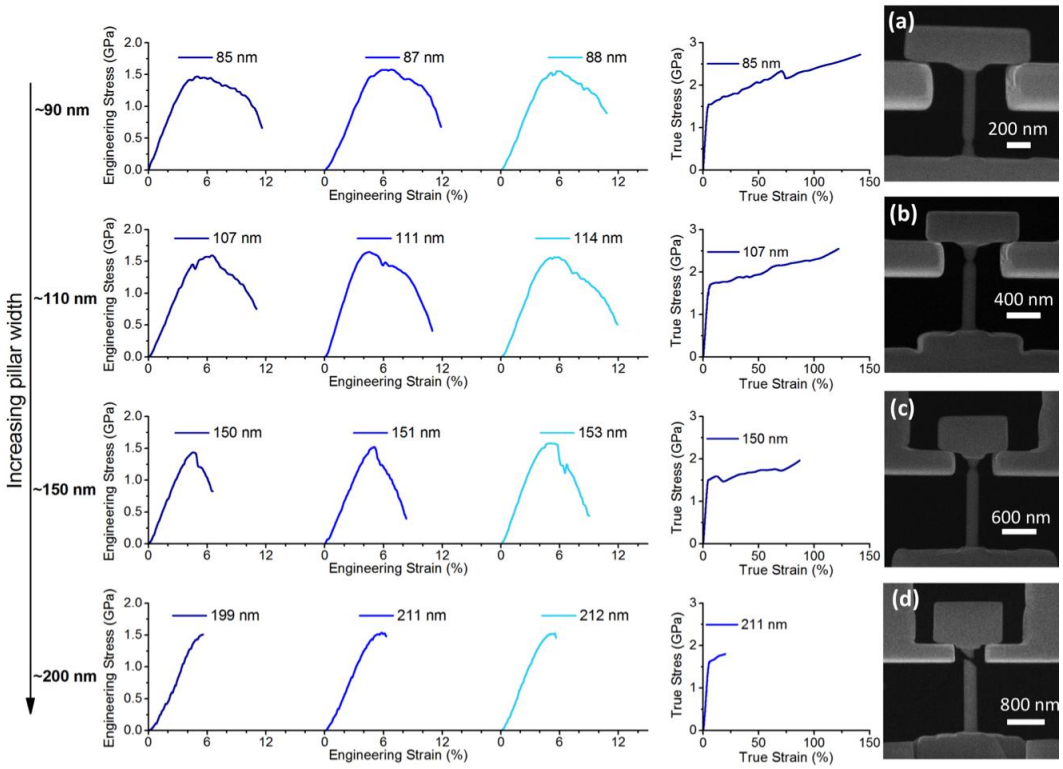

Figure 18. Uniaxial tensile experiments on the as-sputtered Zr-Ni-Al metallic glass samples. (Left) engineering stress-strain data, (center) true stress-strain data, and (a-d) SEM images from in-situ videos around the time of sample failure. The data is grouped by specimen size with ~90 nm wide specimens in the top row, ~110 nm wide specimens in the top-middle row, ~150 nm wide specimens in the bottom-middle row, and ~200 nm wide specimens in the bottom row.

The annealed specimens (Figure 19) also show two distinct regimes of mechanical behavior: the "small" specimen width category < ~110 nm failed by noticeable localized necking and reached true strains around 100%, "large" specimen width categories ≥ ~110 nm failed by shear banding with virtually non-existent ductility. The transition from localized necking (Figure 19 (a)) to shear banding (Figure 19 (b-d)) can be seen in the SEM images from the specimens around the time of failure. Analogous to the as-sputtered samples, the transition from localized necking to shear banding is unambiguous in the in-situ videos: the 209 nm-

wide annealed sample (Video 5 (a, b)) catastrophically shear bands at failure, the 109 nm-wide annealed sample (Video 6 (a, b))shear bands after some post-elastic deformation, and the 93 nm-wide annealed sample (Video 7 (a, b)) exhibits pronounced localized necking. We found the main difference between the as-sputtered and the annealed specimens to be the critical transition width at which the mechanical behavior switches from ductility with significant localized necking to shear banding. For the as-sputtered specimens, this transition occurred somewhere between 150 and 200 nm, and for the annealed specimens, this transition occurred at around 100 nm.

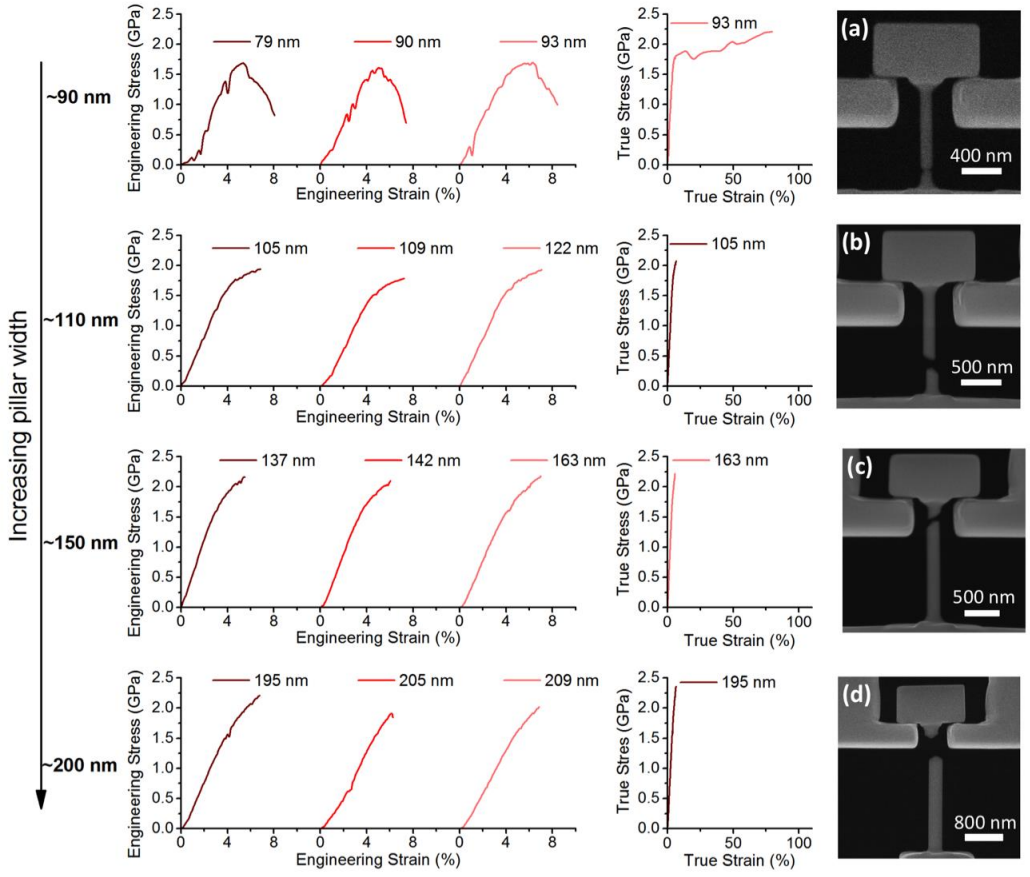

Figure 19. Uniaxial tensile results on annealed Zr-Ni-Al metallic glass. (Left) engineering stress-strain data, (center) true stress-strain data, and (a-d) SEM images from in-situ videos around the time of sample failure. The data is grouped by specimen size with ~90 nm wide specimens in the top row, ~110 nm wide specimens in the top-middle row, ~150 nm wide specimens in the bottom-middle row, and ~200 nm wide specimens in the bottom row.

Beyond these two regimes of mechanical behavior, localized necking versus shear banding, we also observed differences within each regime of mechanical behavior as a function of specimen width. For example, the annealed specimens in width categories ≥ 110 nm all failed by shear banding, with an accompanying loss of ductility for larger and larger samples. As measured by engineering plastic strain, the ~110 nm annealed specimens exhibited 3.2% more plasticity than the ~150 nm annealed specimens, which exhibited 35% more plasticity than the ~200 nm annealed specimens. The shear-banding mechanism is not suppressed in samples of widths above the critical dimension but may require higher forces to initiate when specimen widths approach the critical dimension. A similar trend was observed in the localized necking regime for the as-sputtered specimens: all as-sputtered specimens in width categories < 200 nm failed by localized necking, with smaller specimens exhibiting more plasticity. For example, as measured by engineering plastic strain, the ~110 nm as-sputtered specimens exhibited 45% more plasticity than the ~150 nm as-sputtered specimens.

The summary of measured mechanical properties of the as-sputtered and annealed specimens is displayed in Figure 20. Again, we grouped the mechanical properties by specimen width into categories of ~90 nm, ~110 nm, ~150 nm, and ~200 nm. Some natural variation in specimen size for each category was caused by FIB fabrication; this variation is represented by the horizontal error bars in Figure 20, which correspond to the standard deviation within each size grouping. The vertical error bars indicate the standard deviation in each measured mechanical property within each category of specimen width. We quantified the ductility in the specimens by measuring the plastic strain (ε_p), defined as the total strain at fracture minus the strain at the yield point. Figure 20 (a) contains the engineering plastic strain, $\varepsilon_{p,engineering}$, and indicates that some plasticity is present in all samples tested, with $\varepsilon_{p,engineering}$ ranging from 1.8% to 8.0%. Figure 20 (b) contains the true plastic strain, $\varepsilon_{p,true}$, which is sensitive to

necking: the specimens with $\varepsilon_{p,true}$~100-150% all exhibited obvious necking, while specimens with $\varepsilon_{p,true}$< ~10% exhibited almost no necking with failure by shear banding.

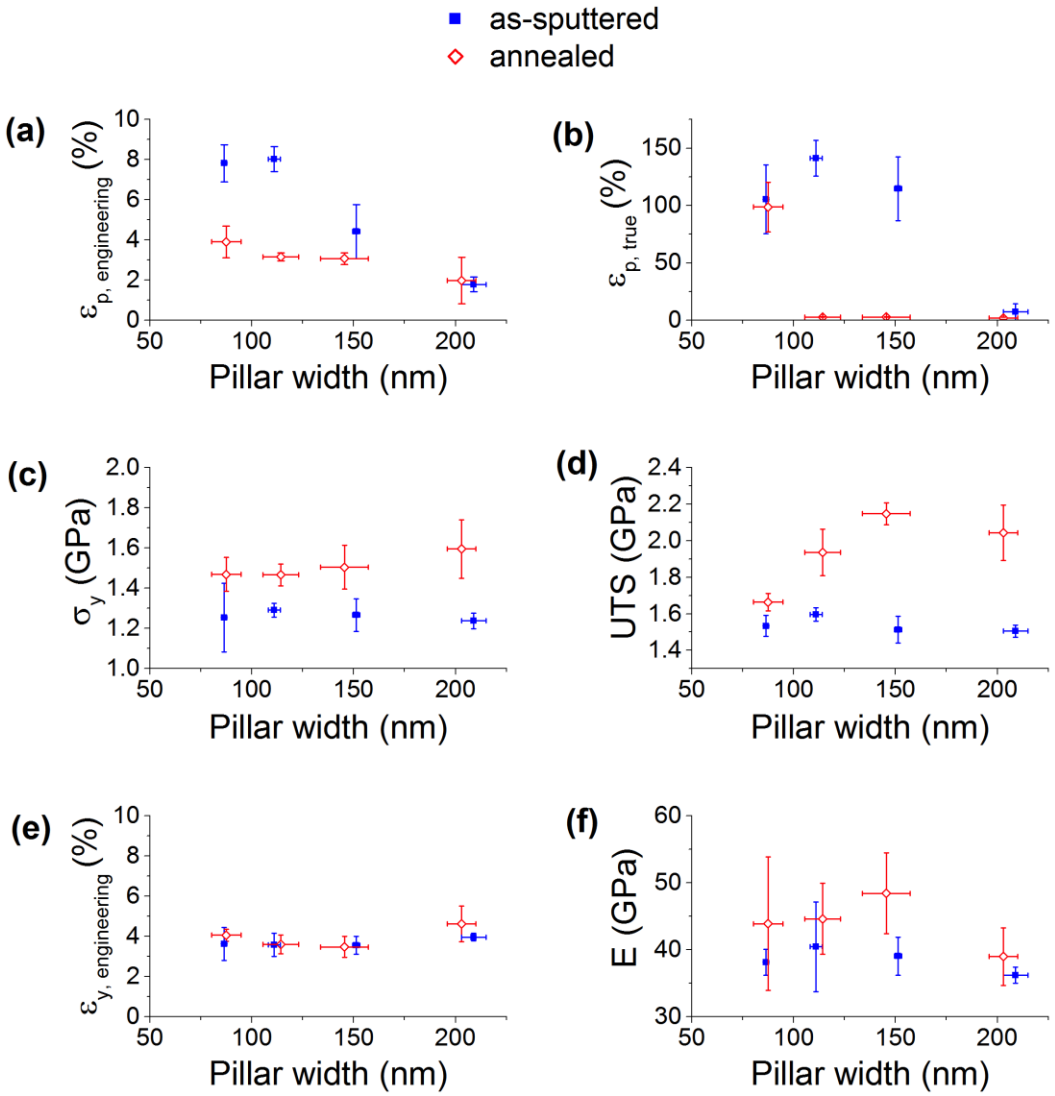

Figure 20. Mechanical properties of as-sputtered and annealed nano-tensile specimens. (a) Engineering plastic strain, (b) true plastic strain, (c) yield strength, (d) ultimate tensile strength, (e) engineering yield strain, (f) elastic modulus. The vertical error bars denote ± one standard deviation in the measured property and the horizontal error bars denote ± one standard deviation in the pillar widths measured for each size grouping (~90 nm, ~110 nm, ~150 nm, ~200 nm).

Measures of strength are included in Figure 20 (c) for yield strength, σ_y, and Figure 20 (d) for ultimate tensile strength, UTS. It appears that the yield strength does not show a significant dependence on specimen size, but was highly influenced by annealing: the as-sputtered

specimens exhibited on average σ_y = 1.26 ± 0.08 GPa and the annealed specimens exhibited on average σ_y = 1.51 ± 0.11 GPa, which indicates that annealing resulted in a ~20% increase in yield strength. The UTS appears to increase dramatically with annealing and with increasing the size of the annealed specimens; however, since the UTS was calculated from engineering stresses, it is dramatically higher for samples that did not neck. Necking leads to a significant decrease in the cross-sectional area in the necked region, which means the sample is not able to accommodate total load as effectively as a sample that fails without such a localized narrowing. The UTS is commonly a more representative reflection of whether the samples undergo necking (low UTS) or fail by shear banding without necking (high UTS).

Figure 20 (e) contains the yield strain, $\varepsilon_{y,engineering}$, which appears to be nearly constant and independent of both sample size and processing conditions. The average yield strain for all samples is 3.79 ± 0.59%. The consistency of the yield strain amongst all specimens indicates the elastic limit of this metallic glass is purely an intrinsic property that is not dependent upon specimen size, fabrication method (sputtering), or post-processing (annealing). As elastic modulus was measured as the slope of the stress-strain curve up to the point of yielding, or simply the yield strength divided by the yield strain, this consistency in yield strain also indicates that any changes in the elastic modulus are due almost entirely to changes in yield strength, not yield strain. The elastic modulus measurements are shown in Figure 20 (f) and are also roughly independent of specimen size, with the average modulus of 38.3 ± 3.84 GPa for the as-sputtered specimens and 44.6 ± 6.74 GPa for the annealed specimens, which represents a ~17% increase upon annealing. This increase is consistent with the ~20% increase in yield strength of Figure 20 (c). A large standard deviation indicated by the error bars in the elastic modulus measurements is common in uniaxial tension experiments at the nanoscale because the modulus is measured from the slope of the loading portion of the nanomechanical data [99-101], which is susceptible to experimental artifacts like a slight misalignment between

the grips and the sample, an imperfect initial contact, and the atomic-level roughness on the tensile grips and specimen head. The relative changes in the modulus are useful for showing the general trend of modulus increasing by ~17% upon annealing; the absolute values of the measured moduli are likely lower than the actual moduli because of these artifacts.

3.3.4. Synchrotron XRD results

To shed light onto the emergence of substantial ductility in excess of 100% true strain in the as-sputtered nano-sized Zr-Ni-Al metallic glass and the dramatic changes in mechanical response upon annealing, we conducted synchrotron XRD measurements on the as-sputtered and the annealed Zr-Ni-Al metallic glass samples. Figure 21 (a) displays the resultant structure function $S(Q)$ as a function of the scattering vector Q, which contains noticeable changes in the first and second peaks between the as-sputtered and annealed samples. Figure 21 (b) shows the zoomed-in first peak, which increases in intensity by 7.4% from $S(Q_1)$=2.425 in the as-sputtered sample to $S(Q_1)$=2.604 in the annealed sample and shifts by 1.7% from Q_1=2.597 Å^{-1} in the as-sputtered sample to Q_1=2.641 Å^{-1} in the annealed sample. Q_1 is inversely proportional to the mean atomic spacing [134], which implies that a larger Q_1 in the annealed sample corresponds to a smaller average atomic spacing compared with the as-sputtered sample. The position of Q_1 is related to the mean atomic volume; the variation in volume upon annealing can be estimated according to Yavari et al. [135] by

$$\frac{V_{annealed}}{V_{as-sputtered}} = \left(\frac{Q_1^{as-sputtered}}{Q_1^{annealed}}\right)^3 \tag{14}$$

where $V_{annealed}$ and $V_{as-sputtered}$ are the mean atomic volumes in the annealed stated and as-sputtered states, respectively. Using equation (14) with the measured values of $Q_1^{as-sputtered}$ = 2.597 Å and $Q_1^{annealed}$ = 2.641 Å, we calculate a ~4.9% lower atomic volume in the annealed sample compared with the as-sputtered sample, indicative of a significant reduction in free

volume due to annealing. Figure 21 (c) contains the second peak in $S(Q)$, which increases in intensity by ~1.6% from $S(Q_2)$ = 1.210 in the as-sputtered sample to $S(Q_2)$ = 1.230 in the annealed sample, as well as a peak split caused by the annealing giving rise to an additional peak at a ~5.2 Å^{-1}, which reflects enhanced local ordering. The heights of the higher order peaks in $S(Q)$ decay rapidly as Q increases, which render measurements of relative changes inaccurate.

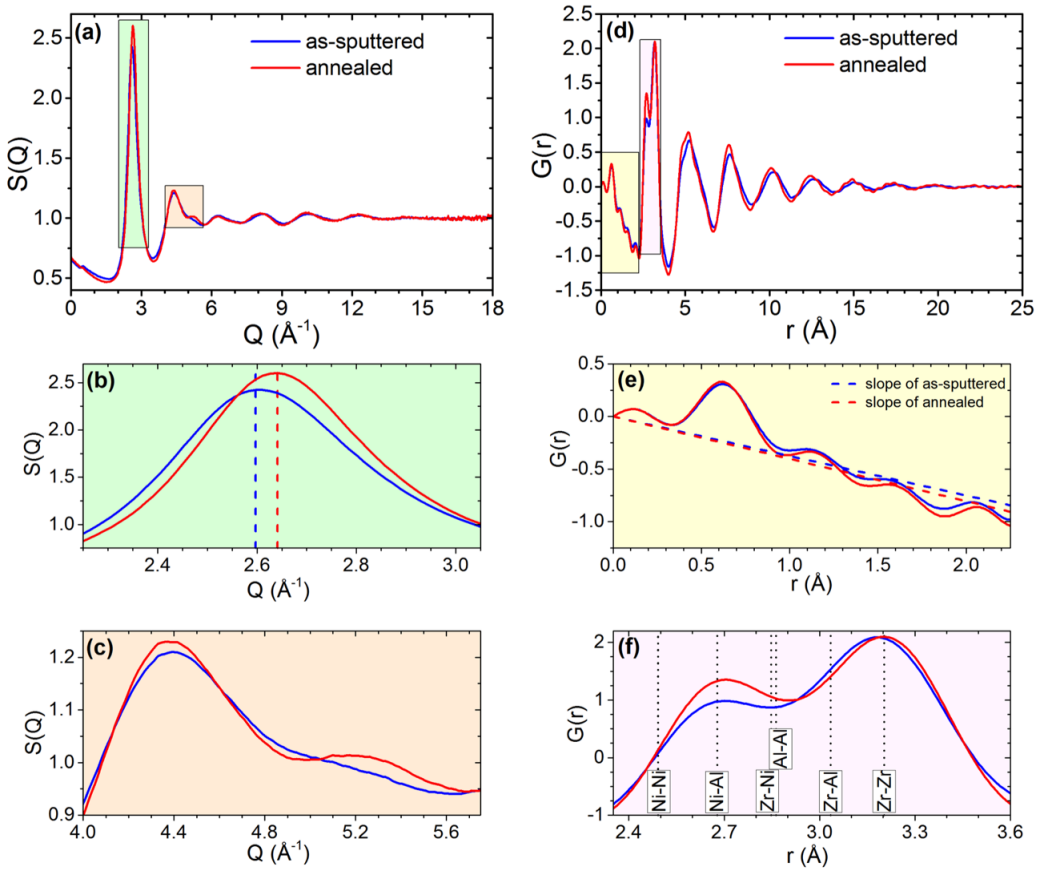

Figure 21. Synchrotron XRD results on as-sputtered and annealed at 625 K Zr-Ni-Al metallic glass. (a) Structure factor, (b) zoomed-in region on the principal peak of the structure factor shown in (a) with dashed lines denoting the peak positions, (c) zoomed-in region on the second peak of the structure factor shown in (a). (d) Reduced pair distribution function, (e) zoomed-in region of the reduced pair distribution function shown in (d) for $r \leq$ 2.25 Å with dashed lines denoting the slope of the curve in this low-r region, (f) zoomed-in region on the first nearest-neighbor peak of the reduced pair distribution function shown in (d) with dashed lines denoting metallic bond distances shown in Table 1.

Figure 21 (d) displays the reduced pair distribution function, $G(r)$, defined as

$$G(r) = 4\pi r\rho_0(g(r) - 1) \quad (15)$$

where r is the distance, ρ_0 is the average number density, and $g(r)$ is the pair distribution function. The pair distribution function $g(r)$ tends to r at small r because atoms cannot overlap, which forces $G(r)$ to behave as $-4\pi r\rho_0$ as $r \longrightarrow 0$. At low r, the slope of $G(r)$ is proportional to the average number density of the material. We measured the slope of $G(r)$ for r < 2.25 Å (Figure 21 (e)) and found it to increase by 7.2% as a result of the annealing, which corresponds to a 7.2% increase in density and a concomitant loss of free volume from annealing. Figure 21 (f) contains a zoomed-in region of $G(r)$ focused on the peaks corresponding to the first nearest neighbor shell of atoms. These peaks appear to undergo significant changes from ex-situ annealing and are important in understanding changes in short-range order. In the as-sputtered state, the main peak at ~3 Å is split into two maxima: one sub-peak at ~2.7 Å and another sub-peak at ~3.2 Å. Upon annealing, the first sub-peak remains at ~2.7 Å and increases in intensity by 37.3% from $G(r)$ = 0.984 in the as-sputtered state to $G(r)$ = 1.351 in the ex-situ annealed state, while the second sub-peak at ~3.2 Å is largely unchanged, increasing marginally from $G(r)$ = 2.089 in the as-sputtered state to $G(r)$ = 2.098 in the annealed state. This indicates a change in the types of atoms within the nearest neighbor shell, where atoms associated with bond lengths of ~2.7 Å become more prevalent and atoms associated with bond lengths of ~3.2 Å exhibiting no significant change. Based on the atomic radii of each constituent in the Zr-Ni-Al metallic glass, metallic bond lengths can be calculated [136], with results shown in Table 1, and denoted by the dashed lines in Figure 21 (f). This plot reveals that upon annealing, the Ni-Al and Zr-Zr bonds become more prevalent because the first sub-peak located at around the Ni-Al bond distance intensifies and the second sub-peak shifts closer towards the Zr-Zr bond distance. Zr atoms represent the majority of all atoms in the Zr-Ni-Al glass in this work, with Ni and Al being the minority

atoms; the observed changes in bond prevalence suggest that upon annealing the minority atoms (Ni and Al) come together significantly while the majority atoms (Zr) also come together slightly. This leads the atomic-level structure in the annealed state to contain more minority-minority (Ni-Al) and majority-majority (Zr-Zr) atom interactions but less majority-minority (Zr-Al or Zr-Ni) atom interactions.

Table 1. Metallic bond lengths, obtained from published metallic bond radii in [136]

Bond	Length (Å)
Ni-Ni	2.492
Ni-Al	2.678
Zr-Ni	2.848
Al-Al	2.864
Al-Zr	3.034
Zr-Zr	3.204

The peaks in $G(r)$ located beyond the first main peak also change considerably as a result of annealing. Table 2 summarizes the peak positions of these medium-range order (MRO) peaks in the as-sputtered and annealed samples and shows that (1) all peaks shift to shorter distances (by ~1%) consistent with an overall densification, and (2) the intensity increases by ~18-48%, which corresponds to more atoms at certain set radial distances and fewer atoms distributed randomly. These measurements imply that annealing leads to a dramatic increase in coordination number and medium-range order.

Table 2. Analysis of the MRO peaks in *G(r)*

Peak Location in *G(r)*			Peak Intensity in *G(r)*		
As-sputtered	Annealed	Change	As-sputtered	Annealed	Change
5.24	5.19	-0.95%	0.669	0.787	17.7%
7.64	7.59	-0.65%	0.468	0.605	29.2%
10.2	10.1	-1.31%	0.209	0.269	29.2%
12.6	12.4	-1.04%	0.107	0.158	48.1%

3.3.5. Molecular dynamics simulation results

We employed molecular dynamics (MD) simulations to gain insight into the mechanisms of annealing-induced atomic ordering and structural relaxation revealed by the synchrotron XRD measurements. Due to lack of long-range order in metallic glasses, their atomic structure can only be characterized in a statistical manner. Indeed, the structure factor and pair distribution function obtained experimentally are one-dimensional entities indicating the possibility of finding another atom at a distance r from a given central atom. In contrast, MD simulations are able to reproduce the atomistic configuration of metallic glasses and characterize their three-dimensional structure, which is not otherwise possible experimentally. As such, MD is almost a unique technique in exploring correlations between microstructure, atomic-level details, and mechanical behavior of metallic glasses under different conditions. Here, we investigated the effect of structural relaxation on the deformation and failure mode of metallic glasses by adjusting the sample cooling rate, and the specific contributions of thermal energy by adjusting the annealing time at a sub-T_g temperature. We also investigated the size effect by performing simulations on different diameter samples. Details of our simulation methodology are provided in section 3.2.5.

Figure 22 (a) shows the engineering stress-strain curves at room temperature (300 K) for the glassy specimens obtained with different cooling rates of 10^{10} K/s to 10^{13} K/s, in order of magnitude increments. For each of these samples, Figure 22 (b-e) present the snapshots of atomic von Mises shear strain, ε^{vM}, calculated at different stages of the applied strain, ε, with respect to the unloaded sample. The loading stage of each snapshot is indicated by an open circle in the stress-strain curve of the corresponding cooling rate in Fig 7(a). According to Figure 22 (a), the sample with the cooling rate of 10^{10} K/s exhibits a pronounced drop in the stress level after the ultimate tensile strength (UTS); this can be attributed to formation and propagation of a dominant shear band as seen in Figure 22 (b), which implies a brittle failure

mode at room temperature in the glassy sample obtained with the slowest cooling. In contrast, Figure 22 (a) also demonstrates that increasing the cooling rate above 10^{10} K/s leads to an altering of the deformation mode toward more ductile (plastic) behavior and almost an ideal plastic flow in the sample formed with the cooling rate of 10^{13} K/s. This is in agreement with Figure 22 (c-e), indicating a homogeneous distribution of atomic deformation in these samples. As such, Figure 22 (a-e) clearly shows a transition in the room-temperature deformation and failure mode from localized shear banding (in the sample formed with the slowest cooling rate) to homogeneous plastic flow (in samples formed with faster cooling rates).

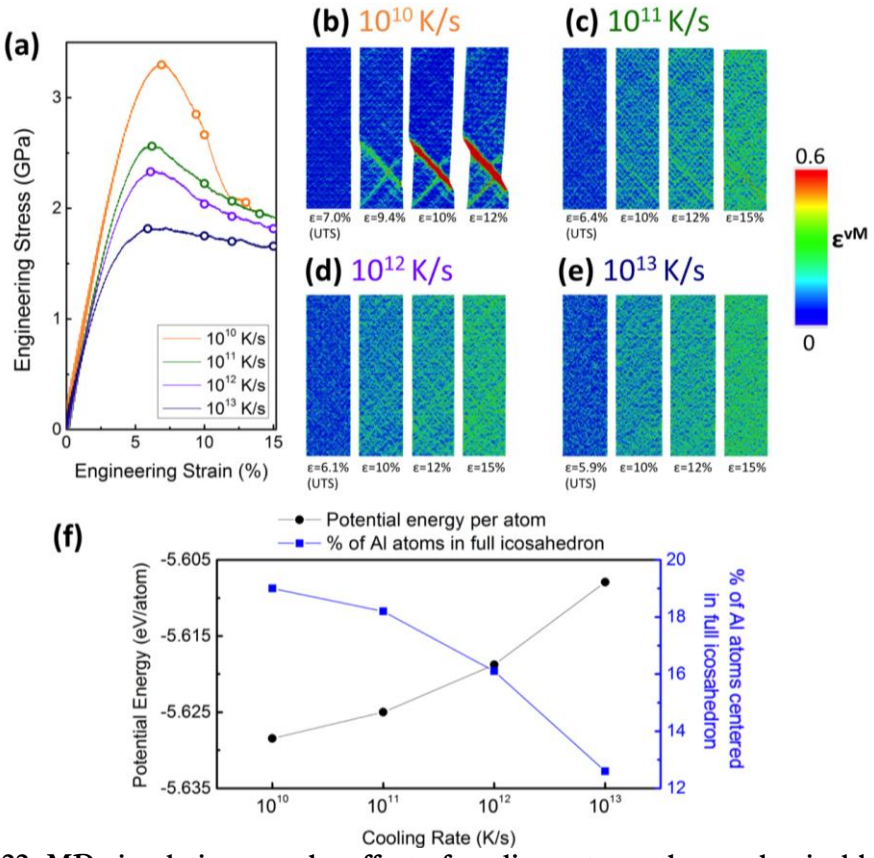

Figure 22. MD simulations on the effect of cooling-rate on the mechanical behavior and atomic structure of Zr-Ni-Al metallic glass. The specimens have diameters of 40 nm and heights of 120 nm. (a) Tensile engineering stress versus strain for samples formed with cooling rates denoted in the legend. (b-d) Analysis of the atomics von Mises shear strains (ε^{vM}) in the samples formed with the cooling rates of (b) 10^{10} K/s, (c) 10^{11} K/s, (d) 10^{12} K/s, and (e) 10^{13} K/s. (f) Effect of cooling rate on the average atomic potential energy (PE) of the system (left axis) as well as the fraction of Al-centered full-icosahedra clusters (right axis).

We further consider the effect of cooling rate on atomic structure by investigating the SRO clusters and average potential energy per atom. Figure 22 (f) demonstrates that a faster cooling rate leads to a more disordered structure as evidenced by a decrease in the fraction of Al-FI clusters and by an increase in the system's average atomic potential energy at room temperature. In other words, increasing the cooling rate results in a glass with a less relaxed structure consisting of more liquid-like clusters (i.e. excess free volume with irreversible dynamics). This reduction in full-icosahedra clusters at faster cooling rates corresponds to a destruction of the stiff backbone of the glass, which may be a key factor responsible for the homogeneous plastic deformation observed in samples formed at higher cooling rates.

We performed further simulations to investigate the effect of sub-T_g annealing on the structure and mechanical response of the metallic glass. To this end, we selected the sample obtained with the cooling rate of 10^{13} K/s, whose tensile deformation commenced in a homogeneous fashion (see Figure 22 (a, e)). In order to determine the appropriate temperature to conduct the annealing for the MD studies, it was necessary to first determine the glass transition temperature, T_g, of the MD-formed metallic glass. Towards that aim, during the quenching process of forming the MD samples, the potential energy per atom was monitored as a function of temperature for cooling rates of 10^{10} K/s, 10^{12} K/s, and 10^{13} K/s, as shown in Figure 23. As in Caprion et al. [137], we determined T_g as the crossover between extrapolations of the high and low temperature curves of potential energy. The resultant T_g values are denoted by dashed lines in Figure 23, with values of ~950 K for the cooling rate of 10^{10} K/s, ~1000 K for the cooling rate of 10^{12} K/s, and ~ 1050 K for the cooling rate of 10^{13} K/s. As the MD annealing was performed on the sample originally formed with a cooling rate of 10^{13} K/s, we conducted the annealing at ~80% of ~1050 K, i.e. ~850 K. We chose this annealing temperature to be consistent with the experimental annealing performed at ~80% of the experimental T_g taken from literature [109].

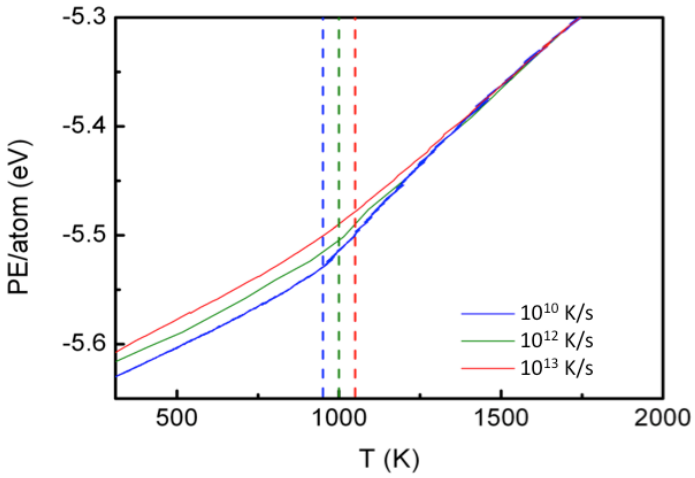

Figure 23. MD simulations of potential energy behavior during quenching. Variation of potential energy as a function of temperature during the formation of $Zr_{55}Ni_{25}Al_{20}$ metallic glass quenched from 2300 K with cooling rates of 10^{10} K/s, 10^{12} K/s, and 10^{13} K/s. The vertical dashed-lines denote the glass transition temperature (T_g) of the alloy.

The annealing simulation was conducted for up to 400 ns; the average potential energy per atom and the fraction of Al-FI clusters were monitored during the annealing process. Figure 24 illustrates the effect of annealing on the mechanical properties and atomic-level structure of the simulated Zr-Ni-Al glass. We observe that annealing the sample that was originally formed at a cooling rate of 10^{13} K/s leads to a 77% increase in the ultimate tensile strength after 200 ns of annealing time (Figure 24 (a)) and shifts the mechanical deformation from homogeneous extension of the as-quenched sample to brittle behavior and shear banding, as illustrated in Figure 24 (b-c). Figure 24 (a) also includes the stress-strain responses of the as-quenched samples originally formed at cooling rates of 10^{13} and 10^{10} K/s, which are provided to show that annealing the sample originally quenched at a cooling rate of 10^{13} K/s leads to a stress-strain response similar to that of the as-quenched sample formed at a cooling rate of 10^{10} K/s. Figure 24 (d) shows a plot of average potential energy per atom and percentage of Al atoms centered in full icosahedron, i.e. Al-FI, versus annealing time. This figure illustrates that increasing annealing time from 0 ns to 400 ns brings about atomic ordering of the system, as evidenced by a 0.2% (~0.01 eV) decrease in the average potential

energy per atom and a 38% increase in the fraction of Al atoms located in the central position of full-icosahedra clusters. These results support that slower cooling rates and greater annealing times lead to the creation of samples with more relaxed and well-ordered microstructures, which exhibit stronger and more brittle behavior, than samples with more disordered structures obtained by cooling at faster rates, which exhibit more ductile responses.

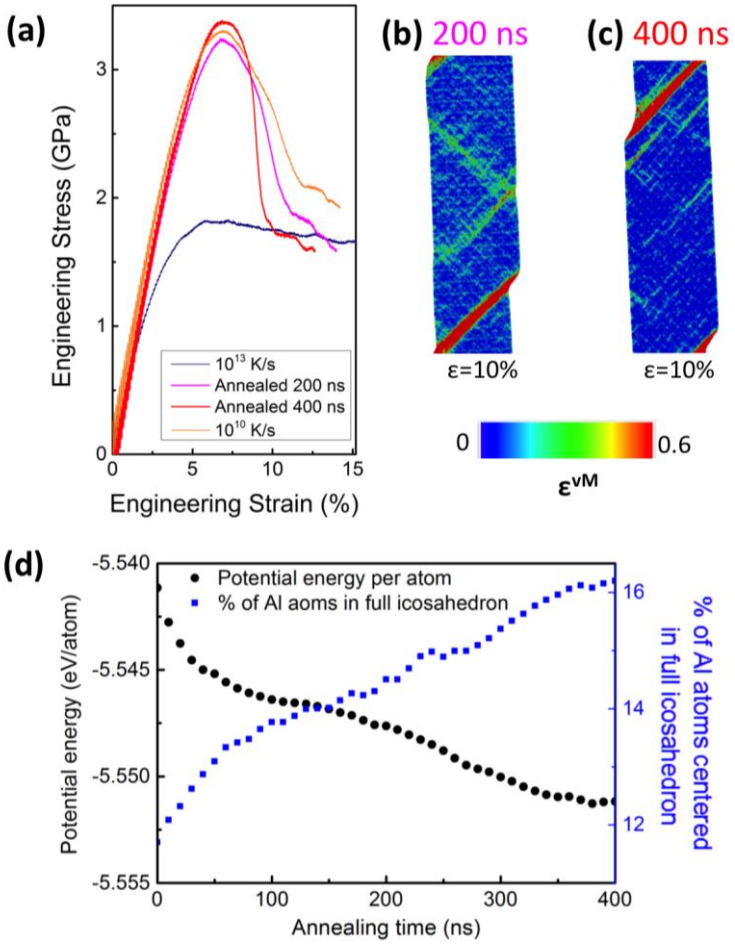

Figure 24. MD simulations on the effect of annealing on the mechanical behavior and atomic structure of Zr-Ni-Al metallic glass. Specimens have diameters of 40 nm and heights of 120 nm. The annealing was conducted at T=850K (80% of simulated T_g). (a) Tensile engineering stress-strain response of the initial as-quenched sample formed with a cooling rate of 10^{13} K/s, after annealing for 200 ns, after annealing for 400 ns, and for comparison the sample formed with a cooling rate of 10^{10} K/s. (b-c) Visualization of atomic von Mises shear strains of the samples annealed for (b) 200 ns and (c) 400 ns. (d) Structural evolution of the metallic glass during annealing at 850 K as measured by the average atomic potential energy (PE) of the system (left axis) as well as the fraction of Al-centered full-icosahedra clusters (right axis).

Previous studies have shown that the structural relaxation during sub-T_g annealing is mainly attributed to localized atomic rearrangements (i.e. β-relaxation), which are manifested in processes such as enhancement in short-range ordering and/or annihilation of free volume [138,139]. In general, the temperature dependence of β-relaxation follows the Arrhenius relation [139]. Previous experimental and theoretical studies suggested that the activation energy of such processes is on the order of 0.1 to 1 eV [140-142]. As such, the estimated relaxation time for such processes at 0.8 T_g is on the order of sub-nanosecond to tens of nanoseconds. This implies that the 400 ns time used in our annealing simulations at 0.8 T_g should allow ample structural relaxations of the metallic glass samples through localized β-relaxation. This is the primary reason why there is the same trend in the strengthening and embrittlement between our simulations and experiments.

Figure 25 illustrates how sample size can have a significant influence on mechanical response. In this figure, MD simulations of tensing different diameter nanopillars reveal that atomic von Mises strains localize into an obvious shear band in the 40 nm diameter sample (Figure 25 (b)). As the sample diameter is reduced to 20 nm the deformation becomes less localized but still exhibits shear banding (Figure 25 (c)), decreasing the sample diameter to 10 nm changes the failure mechanism to necking (Figure 25 (d)), and reducing the sample size to 5 nm leads to even more pronounced necking (Figure 25 (e)). Figure 25 (a) shows the simulated engineering stress-strain data and also demonstrates the shift in failure mechanism as the 40- and 20-nm diameter samples exhibit a sudden drop in stress after yielding due to shear band formation, while the 10- and 5-nm diameter samples exhibit gradual decreases in stress after yielding due to the gradual decrease in cross-sectional area of the necked region. The substantial fluctuations in the stress-strain response of the 5 and 10 nm samples after yielding are likely caused by the stronger effect of atomistic fluctuations in the small samples after each localized atomic yielding event.

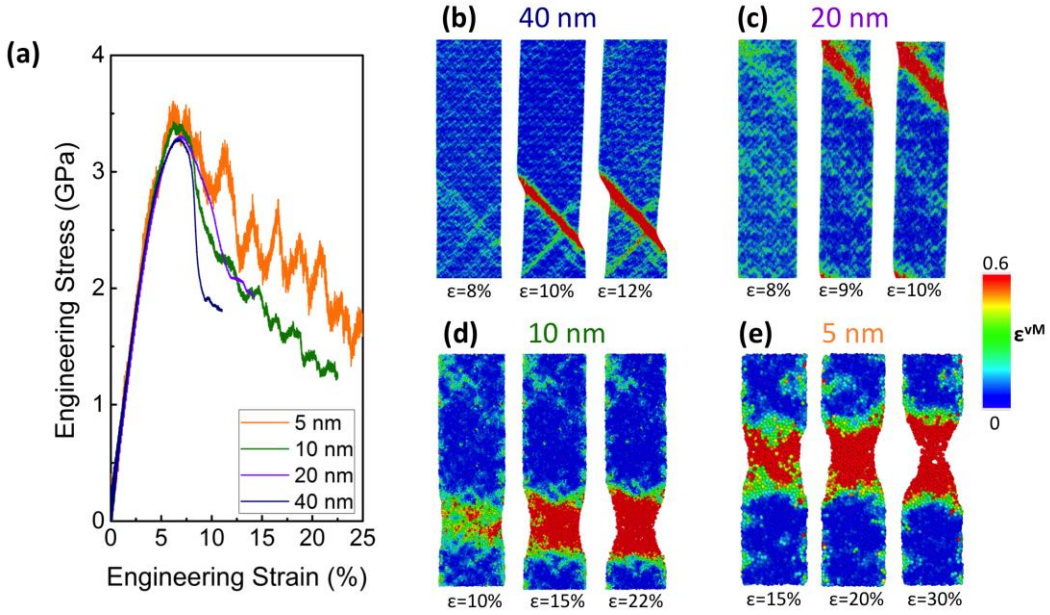

Figure 25. MD simulations on the effect of sample size (i.e. nanopillar diameter) on the mechanical behavior of the Zr-Ni-Al metallic glass. The height of the nanopillars was selected such that the aspect ratio was constant at a value of 3 for height to diameter. (a) Tensile engineering stress versus strain for samples with diameters denoted in the legend. (b-e) Analysis of the atomic von Mises shear strain (ε^{vM}) of the nanopillar samples with the diameters of (b) 40 nm, (c) 20 nm, (d) 10 nm, and (e) 5 nm indicates a transition from brittle shear banding to ductile necking by decreasing the sample size.

3.4. Discussion

3.4.1. Structural relaxation effects

The ductility observed in the as-sputtered metallic glass specimens is substantial, attaining true strains of ~150% and exhibiting visible tensile necking down to a point even in specimens as large as ~150 nm. This represents a significant departure from findings in previous studies, see for example [24,40,41,44] where nano-tensile metallic glass samples were formed by a variety of other non-sputtering processes. This departure may be attributed to the relatively unexplored effect of the sputtering process on the microstructure of the formed metallic glass. Previous studies on small-scale tension of metallic glass nanopillars have utilized various non-sputtering fabrication methods, including thermoplastic molding, which led to almost no plasticity even for sub-100 nm $Pt_{57.5}Cu_{14.7}Ni_{5.3}P_{22.5}$ specimens [44], electrodeposition, which

led to plastic strains of 2% in ~100 nm $Ni_{80}P_{20}$ specimens [24], and copper-mold casting, which led to plastic strains of 23-45% for 100 nm $Zr_{52.5}Cu_{17.9}Al_{10}Ni_{14.6}Ti_5$ specimens [41]. One study on the mechanical properties of small-scale *sputtered* metallic glass was conducted on $Pd_{77}Si_{23}$ metallic glass under compression, which revealed a suppression of failure localization into catastrophic shear bands for specimens with diameters up to 400 nm [38]. This 400 nm diameter is substantially larger than typical diameters reported for the size-induced brittle-to-ductile transition, on the order of 100 nm, and is consistent with the compressive deformability observed in our Zr-Ni-Al samples with diameters up to 555 nm. An early study on sputtered metallic glasses also supports the notion that sputtering produces a metallic glass with lower density in a more disordered state with much higher effective quenching rates [143]. This suggests that sputtering may be a method of metallic glass fabrication to create ductile metallic glasses of a variety of chemical compositions, due to the excess free volume imparted during the sputtering process.

The results of this work reveal that the observed substantial ductility in the as-sputtered nano-sized Zr-Ni-Al stems from the sputtering process creating a metallic glass in a substantially unrelaxed structural configuration with a large amount of residual free volume (i.e. liquid like atomic clusters with irreversible dynamics) in the vitrified state. Annealing these sputtered metallic glasses increased the atomic mobility and induced a relaxation process with structural rearrangements that annihilated some excess free volume, according to free volume theory [144]. This work demonstrates that the original metallic glass fabrication method, i.e. sputtering, and post-processing, i.e. annealing, dramatically affect the atomic-level structure, and hence, mechanical behavior, and failure mode in small-scale metallic glasses. This suggests that the design of systems containing metallic glasses must carefully consider the desired mechanical properties and select the fabrication method, the chosen size, and the post-processing conditions accordingly. The annealing in the current work was done for a time

period of 24 hours. It is likely that more moderate annealing would allow some of the benefits from annealing such as increased strength while maintaining significant ductility. The two systems of the current work: (1) as-sputtered and (2) annealed for 24 hours at 625 K, represent two extremes of possible behavior. By exploring and adjusting the annealing and sputtering conditions, as well as the sample dimensions, it may be possible to obtain metallic glass with specifically desired mechanical properties, in a "materials by design" paradigm.

3.4.2. Sample size effects

Both nano-tensile experiments and simulations revealed a consistent trend in the transition from shear banding to necking with reduced sample diameter: in experiments, this transition occurred between 150 and 200 nm for as-sputtered samples and at ~100 nm for annealed samples, in simulations the transition occurred between 10 and 20 nm. The smaller diameter necessary for the brittle-to-ductile transition in simulations is in agreement with several other MD studies of size effects in nano-sized metallic glasses [145,146] and is commonly attributed to the substantially higher strain rates used in the MD simulations (4×10^{7} s^{-1} in MD compared to 1×10^{-3} s^{-1} in experiments). Faster strain rates have been associated with an increased propensity towards shear banding and a loss of ductility [42,123,147]. Besides, this smaller diameter for the brittle-to-ductile transition in simulations has also been attributed to the lack of surface imperfections such as surface roughness in simulated metallic glass samples as compared to experimental samples [115].

The size-induced ductility may be explained, in part, by surface effects: as the sample becomes smaller, the effect of the surface becomes more significant, as reported in the work of Chen et al. [24]. Surface atoms contain broken bonds and thus cannot form clusters with high local symmetries, such as full icosahedra, which means there is zero concentration of full icosahedra on surfaces and surfaces are structurally liquid. As the sample becomes smaller, the

fraction of total atoms in this highly disordered surface state becomes larger, which means their contribution to mechanical behavior also becomes larger. The novelty of this work is that our results provide a direct link between the disorder in the atomic-level structure, quantified by synchrotron XRD experiments, and the commencement of deformation and failure, as well as confirmation that a larger fraction of atoms in the highly disordered state of surface atoms contributes to the ubiquitously observed emergent ductility in nano-sized metallic glasses.

The surfaces of the metallic glass specimens in this study may also be important in explaining the size-induced ductility because the specimens were fabricated using Ga^+ ion irradiation from a FIB. The influences of this Ga^+ ion irradiation on small-scale-specimens have been thoroughly explored in the last decade [71,148,149]. In particular, ion beam irradiation of metallic glasses has been shown to introduce defects, increase free volume, and cause the growth of nanocrystallites in the amorphous matrix [150-152]. We did not observe any nanocrystallites in the TEM analysis of the Zr-Ni-Al nano-tensile specimens; it is difficult to accurately assess defects in amorphous materials or changes in free volume with TEM. According to Monte Carlo based simulations conducted with The Stopping and Range of Ions in Matter (SRIM) software, glancing angle irradiation of $Zr_{55}Ni_{25}Al_{20}$ with an assumed bulk density of 6.33 g cm^{-3} by 30 keV Ga^+ ions results in ~78% of the implanted Ga present within the first 10 nm of the free surface of the specimen, and ~98% of the implanted Ga present within the first 20 nm of the free surface of the specimen, as shown in Figure 26. This implies that the majority of implanted Ga is located very close to the surfaces of specimens. It is possible that the presence of Ga near the surfaces and Ga bombardments from FIB may influence the mechanical response of nano-sized metallic glasses, which have been shown to exhibit enhanced ductility and a slight suppression of shear banding upon FIB-induced Ga-ion irradiation [23,24,44]. This effect would be more pronounced for smaller specimens, which would have a correspondingly larger fraction of the specimen exposed to FIB; therefore, FIB

processing may be a contributing factor in the observed size effect. However, because samples of the same size were fabricated with identical FIB conditions, the differences between the as-sputtered and annealed sample sets are likely not due to FIB effects. As discussed in section 3.2.1, the annealing was performed from a larger ~3 μm thick film of material prior to any FIB exposure and then after annealing FIB was used to fabricate specimens. This methodology prevented any possible annealing-induced changes to the resultant FIB damage. This makes a direct comparison between Figure 18 (samples FIB-fabricated from the as-sputtered film) and Figure 19 (samples FIB-fabricated from the annealed film) justified. The large difference in ductility between the samples shown in Figure 18 and Figure 19 are due to differences from the samples being in an as-sputtered or annealed state, and likely cannot be attributed to FIB processing. Nevertheless, it should be noted that as all specimens in this study were FIB-fabricated, there is no reference state without FIB exposure. Therefore, even the differences between specimens could be influenced by the disorder introduced by FIB and the limits of disorder allowed by the material. The possible effects of FIB do not significantly influence the takeaway message of this work, which is to demonstrate a comparison between the as-sputtered and annealed small-scale metallic glass specimens. This comparison illustrates the annealing leads to an increase in atomic-level ordering and loss of free volume, which leads to a loss of ductility. In this work, we are less interested in the absolute mechanical response and are focused on the relative comparison between the as-sputtered and the annealed specimens, which experienced identical FIB exposure.

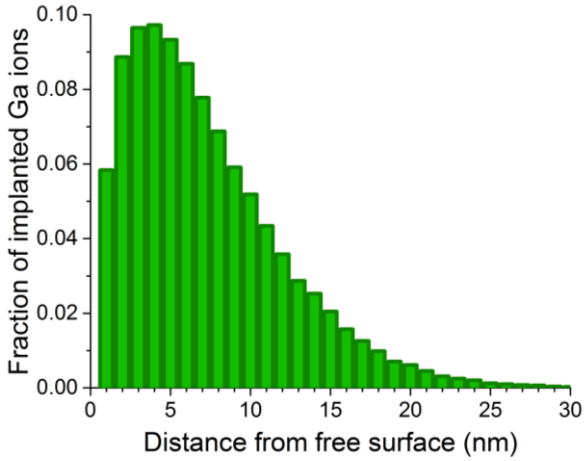

Figure 26. SRIM simulation of Ga-ion implantation resulting from FIB fabrication. The plot displays the fraction of implanted Ga ions as a function of distance from the free surface of $Zr_{55}Ni_{25}Al_{20}$ metallic glass exposed to 30 keV glancing angle Ga-ion irradiation. Each bar covers a 1 nm range of depth.

Several previous studies reported a range of explanations for the dependence of metallic glass ductility on sample size. For example, Chen et al. and Volkert et al. [24,38] have rationalized the observed size effect in terms of energetics and postulated that for a sample with a characteristic dimension d, the total elastic strain energy stored in a sample scales with the sample volume or $\sim d^3$, while the surface energy that a shear band has to overcome to propagate scales with the cross-sectional area of the sample or $\sim d^2$. Therefore below a critical diameter, the elastic energy ($\sim d^3$) is less than the shear banding energy ($\sim d^2$) and it is energetically unfavorable for a shear band to form and propagate. Another reason for size-induced ductility is that the very ductile specimens in this study may be smaller than the critical size of a shear band. One study suggested that for a shear band to fully develop and propagate, its nucleus would have to be ~50-500 nm [14] and another study suggested that embryonic shear bands, that is, shear bands prior to their catastrophic propagation, require a certain running distance in order to become critical [41]. Small specimens, like those studied in this work, may not provide a sufficient nucleation zone or running distance to allow for propagation of shear bands. Others have attributed the observations of size-induced ductility

in metallic glasses to a competition between the energy required for crack-like shear band propagation and that for homogeneous flow [38,40]. Volkert et al. and Jang et al. argue that analogous to Griffith's criterion for crack-propagation, the critical stress necessary to propagate a pre-existing crack-like shear band is [38,40,153]

$$\sigma = \sqrt{\frac{2^{3/2}\Gamma E}{ad}} \tag{16}$$

where Γ is the shear band energy per unit area, E is the elastic modulus, a is the aspect ratio (height/diameter) of the sample, and d is the sample diameter. Thus the critical stress necessary to propagate a shear band decreases with increasing sample size. In larger samples, this critical stress is less than the stress for driving homogeneous flow, so shear bands are inevitable. In smaller samples, like those of the current work, the critical stress for shear bands is greater than the stress for homogeneous flow, so it is favorable for many shear transformation zones to activate throughout the sample, resulting in more homogeneous deformation and ductility [38,40].

In the context of the described existing state of the art knowledge on deformation and energetics of nano-sized metallic glasses, our work demonstrates that the critical size for the emergence of ductility is not fixed for a given metallic glass; it is a strong function of the free volume distribution and the atomic-level energy state. By adjusting the fabrication method and post-processing steps, it is possible to push this critical size to induce ductility to even larger length scales. The parameters yet to be explored include changing the metallic glass composition and modifying the sputtering conditions, like power, argon gas pressure and flow rate, RF versus DC sputtering, co-sputtering Zr, Ni, and Al instead of sputtering from an alloyed target, etc. Optimizing these parameters along with others that have been shown to increase ductility, such as ion irradiation [44,154] and utilizing chemistries with a low ratio of

the elastic shear modulus to the bulk modulus [50,51], may allow for the formation of a grossly disordered metallic glass with exceptional ductility.

Metallic glasses were originally discovered by rapidly quenching metallic alloys to suppress crystallization and bring about a disordered arrangement of atoms. We were able to achieve unique properties in nano-sized metallic glasses by increasing their atomic-level disorder via sputter deposition. Forming metallic glasses by sputtering allowed us to increase the effective quenching rate and to achieve one of the highest-yet reported ductility values in small-scale metallic glasses, which sets them even further apart from crystalline metals and alloys. Controlling the atomic-level disorder enables us to elicit new mechanical properties, such as enhanced ductility, while maintaining the high strength and elasticity intrinsic to metallic glasses.

3.5. Conclusions

In-situ tensile experiments conducted inside a SEM demonstrate substantial ductility in nano-sized sputtered Zr-Ni-Al metallic glasses. The observed ductility is larger than that reported for other metallic glasses, reaching >10% engineering plastic strains, >150% true plastic strains, and necking down to a point during tensile straining in relatively large samples, of widths up to 150 nm. The ductility was highly dependent on specimen size and annealing conditions, with the greatest ductility of ~150% true strain observed in ~90 nm wide as-sputtered specimens, and all annealed specimens of equivalent dimensions exhibiting substantially less ductility. Molecular dynamics simulations, TEM microstructural analysis, and synchrotron XRD characterization techniques were used in concert to assess and to explain the observed mechanical behavior in the framework of free volume reduction and the concomitant increase in short- and medium- range order that occurred upon annealing. These

findings illustrate the key role that the presence and distribution of free volume plays in governing the mechanical deformation, and in particular, ductility.

This work demonstrates the importance of not only the sample dimension but also the original metallic glass fabrication method (sputtering) and post-processing conditions (annealing) in tuning the mechanical properties of a metallic glass for a desired set of properties, potentially for a chosen application. The emergence of tensile ductility and necking in the as-sputtered Zr-Ni-Al with widths up to ~150 nm points towards sputtering as a promising technique for fabricating metallic glasses, particularly as thin coatings. Sputtering is well suited for deposition of thin coatings, and this work shows that the thinness of a sputtered metallic glass coating has the additional benefit of enhanced size-induced ductility that can be observed at relatively large critical dimensions, such as ~150 nm shown in this work. Future work will be aimed at optimizing the sputtering parameters and other conditions that have been shown to influence ductility, such as utilizing systems containing a low ratio of the elastic shear modulus to the bulk modulus [50,51] and post-processing by ion irradiation [44,154]. Such a thorough exploration of parameter space will lead to developing processing techniques for the creation of optimally disordered metallic glasses with maximized ductility at even larger critical dimensions. Creating such ductile metallic glasses at larger length scales would increase the feasibility of utilizing metallic glasses in structural and technological applications, which require not only the high strength, elasticity, and corrosion resistance intrinsic to metallic glasses, but also the tensile ductility, which has been very difficult to achieve.

Chapter 4. Brittle-to-deformable transition in metallic glass nanolattices via decreased wall thickness

Adapted from:

R. Liontas and J.R. Greer. "Brittle-to-deformable transition in metallic glass nanolattices via decreased wall thickness" (in preparation).

Building upon the promising finding in the previous chapter, that sputter-deposited Zr-Ni-Al metallic glass exhibits ductility, this material was chosen as the constituent material to make up 3D architected nanolattices. The nanolattices are constructed from hollow beams of sputtered Zr-Ni-Al metallic glass, where the wall thickness of the beams is on the nanoscale and the overall nanolattice dimension is tens of microns. By keeping the wall thickness in that nanoscale range, where Zr-Ni-Al metallic glass exhibited a "smaller is more deformable" size effect, shown in Chapter 3, we hoped to proliferate such a beneficial nanoscale size effect to the larger ~32 μm nanolattices.

This chapter details a systematic investigation into the effect of wall thickness on the mechanical response of metallic glass nanolattices. Hollow metallic glass nanolattices are fabricated from the same sputtered Zr-Ni-Al metallic glass studied in the nanopillar geometry of Chapter 3. Metallic glass nanolattices with different wall thicknesses are fabricated by varying the sputter deposition time, resulting in nanolattices with median wall thicknesses of ~88 nm, ~57 nm, ~38 nm, ~30 nm, ~20 nm, and ~10 nm. Uniaxial compression experiments conducted inside a SEM reveal a transition from brittle, catastrophic failure in thicker-walled nanolattices to deformable, gradual layer-by-layer collapse in thinner-walled nanolattices. As the nanolattice wall thickness is varied, large differences in nanolattice deformability are apparent from the severity of the first strain burst, nanolattice recovery after compression, and

in-situ images obtained during compression experiments. The brittle-to-deformable transition that occurs as the nanolattice wall thickness is decreased stems from the "smaller is more deformable" material size effect in nano-sized metallic glasses. This work demonstrates that such a nanoscale size effect can be proliferated to larger materials through the use of nanolattices as long as the wall thickness of the nanolattice beams is kept in that "smaller is more deformable" size regime.

4.1. Motivation

While the finding of substantial ductility in sputtered Zr-Ni-Al metallic glass nanopillars discussed in Chapter 3 is of fundamental interest, individual nanopillars are not practical engineering materials. Larger, potentially more useful metallic glass materials benefiting from the "smaller is more deformable" size effect may be envisioned through nano-architecting, that is, maintaining a key dimension of the architected material at the nanoscale without limiting the overall macroscopic dimensions of the material. Here we utilize nano-architecting by fabricating hollow metallic glass nanolattices: materials composed of hollow beams of metallic glass, where the wall thickness of the metallic glass beams is in the "smaller is more deformable" nanoscale size range, but the entire nanolattice structure is tens of microns and could be arbitrarily large when experimental practicalities are neglected.

The field of nano-architected materials is relatively new and has recently grown due to advancements in nanoscale fabrication methods, such as direct-laser-writing two-photon lithography [155-157]. These technological advances in fabrication techniques have enabled the creation of architected structural metamaterials, or nanolattices, with hierarchical ordering ranging from angstrom and nanometer length scales in material microstructure and wall thickness to micron and millimeter scales in macroscale architecture [158]. Existing work on nanolattices has primarily focused on hollow ceramic nanolattices [159-163], due to the ease

of depositing conformal coatings of ceramic materials by atomic layer deposition (ALD) and the inertness of these ceramic materials to oxygen plasma, which has thus far been the plasma of choice for etching away the internal polymer scaffold to result in hollow nanolattices. One of the key findings from these studies is that by optimizing the wall thickness-to-radius ratio of the nanolattice beams, hollow alumina nanolattices can recover to their original shape after compression in excess of 50% strain [161]. There have also been a few studies on hollow Au nanolattices [164,165], which demonstrated that strength and stiffness can be increased by an order of magnitude by tuning nanolattice geometry while maintaining a constant relative density [165].

A summary of previous work on architected metallic glasses is provided in section 1.2.4. Stochastic metallic glass foams have been widely studied due to ease of fabricating such structures by incorporating gas into metallic glass during processing [166,167] or by creating a two-phase mixture of (1) metallic glass and (2) another material, which can be subsequently removed [168-170]. These fabrication techniques produce metallic glass foams containing a distribution of pore sizes. While stochastic metallic glass foams have exhibited improved ductility [56-58], the randomness of the architecture significantly reduces mechanical performance [59-61]. Periodically architected metallic glass foams can be designed for optimal mechanical performance but difficulty in fabrication, particularly in 3D, has resulting in only a few studies on the subject. Existing studies on periodically architected metallic glass are discussed in section 1.2.4 with the results demonstrating high energy absorption [54], enhanced plasticity [62], and improved mechanical performance over stochastic metallic glass foams [61]. Importantly, these previous studies on periodically architected metallic glass involve dimensions far from the nanoscale size range of nanolattices in this work, with [61] using ~1 mm unit cells and 20-70 μm wall thicknesses, [54] utilizing cm-sized unit cells and ~0.4 mm wall thickness, and [62] using mm-sized unit cells and wall thicknesses ~60-600 nm.

In designing periodically nano-architected metallic glasses, both the periodic and nanoscale aspects are key to take advantage of both structural and material size effects.

Experimental difficulty in fabricating hollow metallic glass nanolattices has resulted in a dearth of studies on the subject. The only study to date on metallic glass nanolattices [63] did not consider several important factors in nanolattice fabrication and characterization. The reported oxygen plasma etch time to remove the nanolattice polymer core was 2.5 hours [63], which is more than an order of magnitude less that previous reports of 50-75 hours [161]. Careful inspection of SEM images in [63] suggests that the polymer core was not removed. Further, the nanolattices of that study were composed of $Cu_{60}Zr_{40}$ metallic glass [63], which visibly oxidizes (changing in color from shiny silver to charred black) when placed in oxygen plasma for just a couple minutes. It is then likely that the metallic glass nanolattices in that study at least partially oxidized and were not hollow. In addition, the wall thickness of the nanolattices in [63] was assumed to be given by the deposition rate when sputtering onto a flat substrate. As this chapter will demonstrate, the deposition rate onto nanolattices can be an order of magnitude slower than that onto a flat substrate. Sputtering onto nanolattices also results in significant variation of the wall thickness within individual nanolattices, which necessitates detailed cross-sectional cuts and image analysis to determine the wall thickness distribution, as done for example in a previous study on sputtered Au nanolattices [164]. The methodology choices in the only previous study on metallic glass nanolattices [63] to date warrant a more rigorous study on conclusively hollow metallic glass nanolattices with more accurately measured wall thicknesses.

4.2. Methods

4.2.1. Fabrication of hollow metallic glass nanolattices

Hollow metallic glass nanolattices were fabricated through the multi-step process shown schematically in Figure 27. The basic steps in this nanolattice fabrication process were originally established for other material systems as detailed in [159-161,164]. First, polymer scaffolds were fabricated utilizing the direct-laser-writing two-photon lithography process developed by Nanoscribe GmbH. The 3D geometry of the polymer scaffold was chosen as repeating ~7 μm octahedron unit cells connected at their vertices, as shown in Figure 29 (a). Octahedron unit cells were selected as they represent a fundamental, commonly studied geometry [160,162,164,165] and thus serve as a good base unit cell for one of the first studies on metallic glass nanolattices. Further, the lack of additional beams in an octahedron, as opposed to octet [171] geometry, allows the unit cells to be more open, which facilitates better conformality in the sputter-deposited metallic glass coating. The ~7 μm size was chosen to maximize unit cell size to further facilitate openness of the unit cells for sputter deposition while not utilizing overly long beams, which were found to become wavy and unstable when written with the Nanoscribe. Ideally, the overall nanolattice dimensions would be maximized in order to limit edge effects and make the nanolattice more representative of larger materials with this same repeating unit cell structure. Experimental practicalities, including writing time of the polymer scaffolds with Nanoscribe, hydrogen plasma penetration into the nanolattices during etching, and the maximum load achievable in the nanomechanical testing system, limited the size of the nanolattices. Considering these experimental practicalities, each nanolattice was designed to be 5 unit cells wide by 5 unit cells long by 5.5 unit cells tall, for total dimensions of ~32 μm long, ~32 μm wide, and ~36 μm tall.

This geometry was imported into NanoWrite, the program that interfaces with the Nanoscribe two-photon lithography instrument. In the two-photon lithography process, IP-

Dip photoresist was exposed to a 780-nm femtosecond pulsed laser, which was focused to a small volume (i.e. a voxel, or volume resolution element) containing sufficient energy to initiate cross-linking of the photoresist through two-photo absorption. This voxel was traced in three dimensions according to the nanolattice geometry imported into NanoWrite to create the polymer scaffold. Due to the elliptical nature of the voxel, writing circular beams required tracing the elliptical voxel in a circular motion to result in beams composed of an approximately circular cross-section with diameter ~800 nm. Following lithography, the samples were developed by 30-minute immersion in propylene glycol methyl ether acetate, cleaned in isopropyl alcohol, and then dried in a critical point dryer.

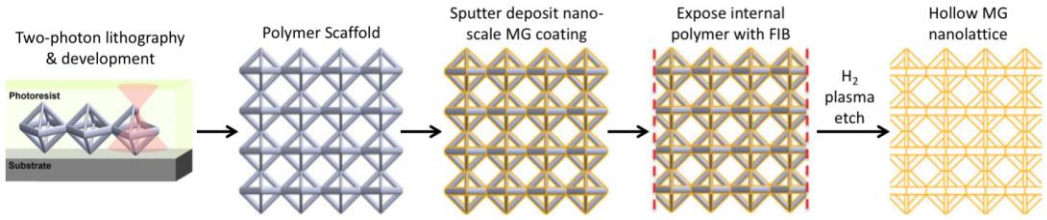

Figure 27. Fabrication of hollow metallic glass (MG) nanolattices. Fabrication involves utilizing two-photon lithography to write a polymer scaffold which is coated with a nanoscale thickness of metallic glass by sputter deposition. Then FIB is used to remove the outside edges of the metallic glass coating, which exposes the internal polymer scaffold so that it can be subsequently etched away by hydrogen plasma. This process results in a nanolattice structure composed of hollow beams of metallic glass, where the wall thickness of the beams is on the nanoscale. Adapted from [160] with permission.

Amorphous Zr-Ni-Al was sputtered to coat these polymer scaffolds under the same conditions discussed in section 3.2.1, namely by sputtering an alloyed $Zr_{56}Ni_{22}Al_{22}$ target (ACI Alloys, Inc.) with a base pressure less than 1×10^{-6} Torr using a DC power supply at 100 W with resultant voltage of 320-390 V, under 3 mTorr argon in a magnetron sputter deposition system (ATC Orion sputtering system, AJA International, Inc.). The sputter deposition time was varied at times of 15, 30, 45, 60, 120, and 240 minutes in order to vary the thickness of the metallic glass coatings on the polymer scaffolds.

After sputtering, focused-ion beam (FIB) milling was used to expose the internal polymer scaffold so that it could be subsequently etched away by hydrogen plasma. For this step, the FIB was operated at 30 keV and 1-3 nA in order to remove the metallic glass coating on two opposite faces of each nanolattice, exposing the internal polymer scaffold. The samples were then placed in a hydrogen plasma system (Zepto Plasma System, Diener) operating at 100 W and 0.7 mbar to etch away the internal polymer scaffold, resulting in hollow beam nanolattices with beam walls consisting of nanoscale thicknesses of the sputtered metallic glass. The hydrogen plasma etching process took several weeks to completely remove the internal polymer scaffold. Due to the long nature of this process, the nanolattices were periodically removed from the plasma machine and imaged via SEM to monitor the etching progress. Changes in contrast as the polymer was etched were readily apparent from SEM images; a visible front of contrast change proceeded from the FIBed edges towards the center of the nanolattice as the polymer etching front advanced, as shown in Figure 28. The nanolattices were kept in hydrogen plasma until all visible traces of polymer were removed.

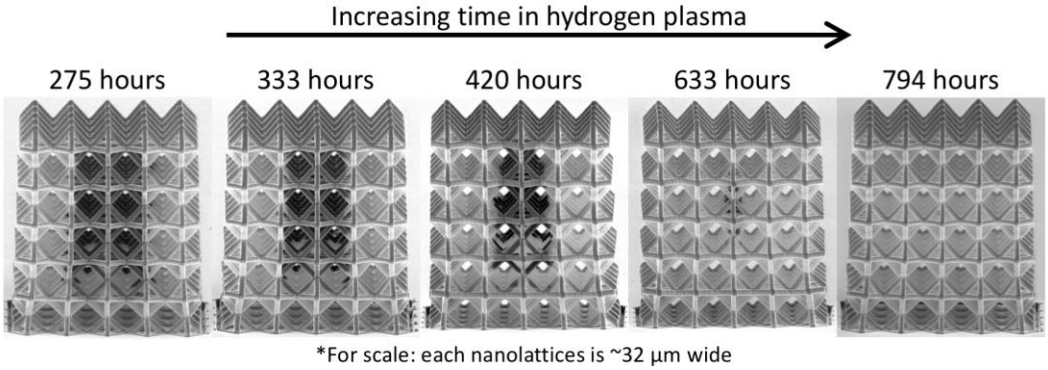

Figure 28. Nanolattices after various times in hydrogen plasma. The darker region is the un-etched section of metallic glass beams still containing a polymer core and the lighter region is the etched section of hollow metallic glass beams with polymer removed. The etch progression is apparent from the disappearance of the darker region with increased time in hydrogen plasma. Images were taken at ~85° tilt of the SEM stage.

4.2.2. Wall thickness analysis

The sputter deposition discussed previously involved the bombardment of argon ions onto the $Zr_{56}Ni_{22}Al_{22}$ sputtering target in order to cause the target atoms to be ejected and deposit largely in a line-of-sight manner onto the nanolattices. This directional nature of sputter deposition results in a metallic glass coating on the nanolattices that is inherently non-conformal, with larger wall thicknesses on the top surfaces and outer unit cells of the nanolattices. To assess the variation in wall thickness resulting from the anisotropic sputter deposition process, FIB was used to remove regions of the nanolattices and expose various cross-sections of the nanolattices from which the wall thickness of each side of each exposed beam could be measured via SEM. One such resultant cross-section is shown in Figure 29 with higher magnification images from each unit cell arranged from top to bottom, illustrating the variation in wall thickness that results from top to bottom in the nanolattices. These cross-sectional cuts and the corresponding measurements were performed at six different locations in each measured nanolattice, ranging from the outermost side to the most interior unit cells in order to assess the variation in wall thickness that occurs from outside to inside. From each cross-sectional cut, ~20 measurements of wall thickness were performed on beams favorably oriented with the ~52° tilt of the SEM stage utilized for FIB operation. With these six cross-sectional cuts and 20 measurements for each cut, there was a representative sample of ~120 wall thickness measurements spanning the entire nanolattice from which the median and average wall thickness were determined. This measurement procedure was conducted on nanolattices fabricated with the longer sputter deposition times of 60, 120, and 240 minutes. For the shorter sputter deposition times of 15, 30, and 45 minutes, it was difficult to measure the wall thickness accurately by SEM; therefore, the wall thickness was estimated by assuming a linear variation between 0 and the wall thickness resulting from the 60-minute sputter deposition.

4.2.3. Microstructural analysis

The microstructure of the metallic glass nanolattices was examined by transmission electron microscopy (TEM). The TEM sample was prepared from a nanolattice fabricated by sputter deposition for the shortest time of 15 minutes, with wall thickness ~10 nm, after all the fabrication steps shown in Figure 27. The nanolattice was transferred to the post of a TEM grid (PELCO, FIB lift out TEM grid) using a micromanipulator, secured with silver conductive epoxy (H2OE EPO-TEK, Ted Pella, Inc.) allowed to cure at room temperature, and thinned with FIB. TEM was performed using a 200 keV TEM (TF20, FEI Co.).

4.2.4. Uniaxial compression experiments

In-situ uniaxial compression experiments on individual nanolattices were performed quasi-statically at a constant nominal strain rate of 1×10^{-3} s^{-1} in the InSEM, a combined SEM (Quanta SEM, FEI Co.) and nanoindenter (Nanomechanics, Inc.). The nanoindenter was fitted with a boron-doped diamond 170-μm flat punch. After accounting for response from the load frame and support spring, the raw load and displacement due to deformation of the nanolattice were recorded at a data acquisition rate of 100 Hz. Using this load (P) and displacement (Δl) data, engineering stress and strain were calculated using the initial nanolattice height (l_0) and footprint area (A_0) according to

$$\sigma_E = \frac{P}{A_0} \tag{17}$$

$$\varepsilon_E = \frac{\Delta l}{l_0} \tag{18}$$

where σ_E is the engineering stress and ε_E engineering strain. The initial nanolattice height and footprint area were measured by SEM images of each nanolattice prior to testing. Elastic modulus was calculated from the slope of the loading curve, using stress-strain data from the initial linear region after any initial loading instabilities. The yield strength was determined by

offsetting the linear fit of the elastic modulus by 0.02% strain and finding the intersection of that offset line with the stress-strain data. The average elastic modulus and average yield strength for each nanolattice wall thickness were calculated from a minimum of 20 sets of compression data. The size of the first strain burst was measured for each data set using MATLAB to find the range of strain around the first strain burst over which the stress was continually decreasing.

Conducting compression experiments with the InSEM system allowed simultaneous compression and visualization, which facilitated a deeper understanding of the deformation behavior of individual nanolattices. The compression experiments were conducted under identical SEM imaging conditions, namely 2 keV, spot size 3, and a magnification of 6000x. There was no discernible difference in the mechanical behavior of the nanolattices observed when the electron beam was off, thus any effects of the electron beam can be considered negligible.

4.3. Results

4.3.1. Characterization of nanolattices

The Nanoscribe system of writing the polymer scaffolds of the nanolattices resulted in consistent, repeatable structures, with a typical SEM image of a hollow metallic glass nanolattice after all fabrication steps shown in Figure 29 (a). The beams of this nanolattice are hollow with the walls of the beams composed of the metallic glass. In this image, one of the trenches created from the FIB step of fabrication, depicted in Figure 27, is visible in the bottom right side of Figure 29 (a).

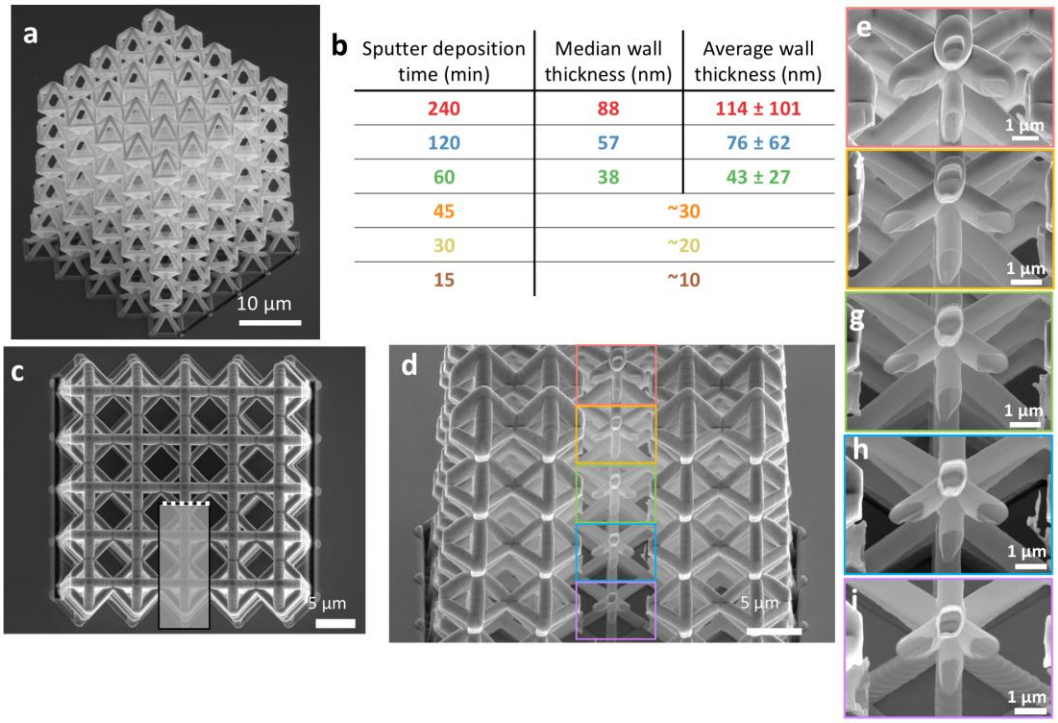

Figure 29. Nanolattice geometry and wall thickness. (a) SEM image of a nanolattice taken at 50° stage tilt. The sputter deposition used to fabricate the nanolattices resulted in significant variation in metallic glass wall thickness as indicated in table (b) which notes the median and average wall thicknesses ± one standard deviation for the different sputter deposition times. Sputter deposition times of 45 minutes and less resulted in nanolattice beams with walls too thin to reliably measure via cross-sectional cuts and SEM imaging, and hence the wall thicknesses for those deposition times are approximate. (c) Top-down image of a nanolattice fabricated by sputter deposition for 240 minutes with rectangle denoting the region removed by FIB to expose the cross-sectional SEM images shown in (d-i). The images in (e-i) are higher magnification images of the unit cells in (d) arranged in top-down order with (e) the top unit cell and (i) the bottom unit cell.

As discussed in section 4.2.2, the wall thickness of the beams varies substantially within a single nanolattice due to the directional nature of sputter deposition. Figure 29 (c-j) contain SEM images demonstrating the process of utilizing FIB to remove regions of the nanolattice and expose cross-sections from which wall thicknesses may be measured. All the images shown in Figure 29 (c-j) were obtained from a nanolattice fabricated for the longest sputter deposition time of 240 minutes, which resulted in the largest wall thickness variation within the nanolattice. Figure 29 (c) shows a top-down image of the nanolattice with the gray

rectangle denoting the region of the nanolattice that was removed by FIB and the white dotted line denoting the exposed cross-section, which is shown in Figure 29 (d). Higher magnification images of each unit cell in this cross-section are shown in Figure 29 (e-i) arranged in order from (e) the top unit cell closest to sputter target to (i) the bottom-most unit cell closest to the substrate. There is a visible decrease in wall thickness of the nanolattice beams in moving from the top to bottom unit cells.

In particular, the top surfaces of the top-most unit cells exhibit significantly larger wall thicknesses, compared to the lower unit cells. The top surfaces are expected to have thicker walls as these surfaces were directly in line-of-sight of the sputtered target atoms. The 240-minute sputter deposition, which resulted in an 88 nm median wall thickness and 114 nm average wall thickness, resulted in wall thicknesses on the top surfaces of the top beams around ~900 nm, which is similar to observed film thickness of ~1 μm on the surrounding flat substrate. For the sputter deposition time of 240 minutes, there is an order of magnitude difference between the median wall thickness of the nanolattice beams (~88 nm) and the thickness of a thin film deposited on a flat substrate (~1 μm). This demonstrates the large error introduced by assuming the sputter deposition rate onto the complex 3D geometry of a nanolattice is equal to the sputter deposition rate onto a film, which was the assumption used in the only previous study on metallic glass nanolattices to date [63].

In this chapter, the time of sputter deposition was varied to produce nanolattices with a range of wall thicknesses. The wall thickness was measured by the cross-sectional analysis discussed in section 4.2.2 and illustrated in Figure 29 (c-i). The table shown in Figure 29 (b) notes the resultant median and average wall thicknesses for sputter deposition times of 60, 120, and 240 minutes. As discussed in section 4.2.2, sputter deposition times of 15, 30, and 45 minutes resulted in walls too small to reliably measure via SEM. Thus, the wall thicknesses shown in Figure 29 (b) for those sputter deposition times are estimated by assuming the wall

thickness varies linearly between 0 and the wall thickness resulting from the 60-minute sputter deposition. The average wall thickness measurements are shown with plus/minus one standard deviation in the measured wall thicknesses. The average wall thickness is skewed by the large wall thickness measurements from the top surfaces of the nanolattices, which usually do not undergo significant deformation during compression. Therefore, the median wall thickness, which is more representative of the wall thickness for the beams undergoing deformation, will be used to refer to each set of data. It should be emphasized that the median wall thickness is a reference point utilized mostly as a matter of convenience in referring to each set of data. In reality, each sputter deposition time results in a distribution of wall thicknesses throughout an individual nanolattice, with that distribution shifting to larger wall thicknesses with increased sputter deposition time. Measured wall thickness distributions are displayed in Figure 30 for sputter deposition times of 240, 120, and 60 minutes, which correspond to median wall thickness of 88, 57, and 38 nm, respectively. The distributions of wall thickness for different sputter deposition times exhibit significant overlap but do shift to larger wall thicknesses with increased sputter deposition time.

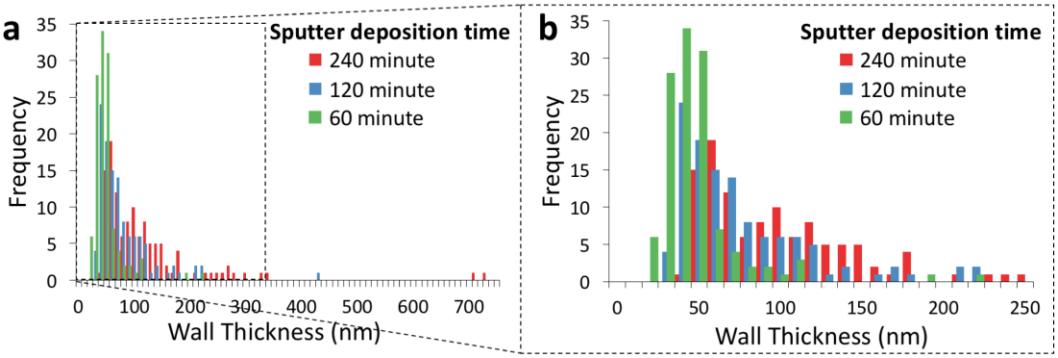

Figure 30. Histogram of wall thickness measurements for nanolattices fabricated by sputter deposition for 240, 120, and 60 minutes. (a) Histogram displayed over the entire range of measured wall thicknesses from 0-750 nm. (b) Histogram zoomed in to the wall thickness range of 0-250 nm to make the distributions at small wall thicknesses more visible. Sputter deposition times of 240, 120, and 60 minutes correspond respectively to nanolattice median wall thicknesses of 88, 57, and 38 nm.

Figure 31 displays TEM images collected from a nanolattice with a ~10 nm wall thickness (sputter deposition time of 15 minutes) after all the fabrication steps of Figure 27. A low-magnification TEM image showing an entire unit cell of that nanolattice is displayed in Figure 31 (a). The FIB thinning discussed in section 4.2.3 to prepare the nanolattice for TEM resulted in some changes to the shape of the beams and arrangement of unit cells in the nanolattice structure. Figure 31 (b) contains the diffraction pattern obtained from the region of the nanolattice marked with a star in Figure 31 (a). The diffuse rings in the diffraction pattern confirm the amorphous structure of the nanolattice walls after all fabrication steps, thereby confirming the hollow nanolattices are indeed composed of metallic glass. This amorphous microstructure is further corroborated by the lack of ordering observed in the high resolution TEM image (Figure 31 (c)) obtained from the same region of the nanolattice marked with the star in Figure 31 (a). Many other regions in the nanolattice were examined via TEM and were found to exhibit similar characteristic amorphous diffraction patterns and images with no evidence of nanocrystallites. The stoichiometry of the deposited metallic glass corresponds to $Zr_{54}Ni_{28}Al_{18}$ as measured by EDS. This composition is slightly different than that of the nanopillars in the previous chapter, which had a measured composition of $Zr_{55}Ni_{25}Al_{20}$. The minor difference in composition may be due to the use of a new Zr-Ni-Al alloyed sputtering target in this work, which may have contained a slightly different composition than the sputtering target used to deposit the metallic glass previously in Chapter 3. Compositions of the nanopillars in Chapter 3 and the nanolattices of this chapter are sufficiently close that given the variability in EDS it cannot be concluded that the samples are compositionally different.

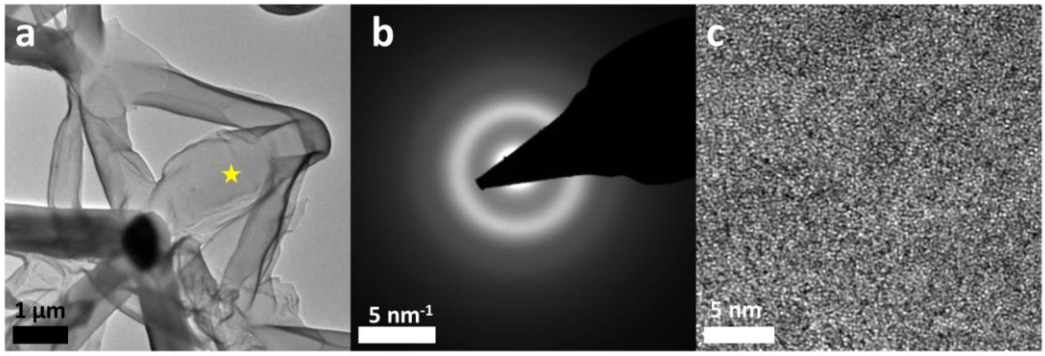

Figure 31. Microstructural analysis by TEM performed on a section of a Zr-Ni-Al nanolattice. (a) TEM image of a particular unit cell in that nanolattice. The (b) diffraction pattern and (c) high resolution TEM image were obtained from the region centered around the yellow star marked in (a).

4.3.2. Compression experiments on nanolattices of various wall thicknesses

Figure 32 (a) contains representative engineering stress versus strain data obtained via uniaxial compression to ~67% strain on nanolattices with wall thicknesses ranging from ~10 nm to ~88 nm. The nanolattices with thicker walls (~57 nm and ~88 nm) were difficult to compress to exactly 67% strain due to the presence of frequent strain busts involving sudden jumps in strain corresponding to failure of the nanolattice layers. One such strain burst can be observed between points I and II in Figure 32 (a). The stress-strain data for the thick-walled nanolattices (wall thicknesses of ~57 nm and ~88 nm in Figure 32 (a)) exhibit large catastrophic strain bursts indicative of brittle failure. For thinner-walled nanolattices the mechanical response becomes more deformable, as demonstrated by a decrease in the size of the strain bursts and an increase in the smoothness and continuousness of the stress-strain data. The nature of deformation is also apparent from the in-situ images shown in Figure 32 (I-IV) for the ~88 nm wall thickness nanolattice, which exhibits catastrophic destruction of nanolattice layers from large strain bursts, and Figure 32 (I′-IV′) for the ~20 nm wall thickness nanolattice, which exhibits gradual layer-by-layer collapse and folding up of nanolattice layers on top of each other.

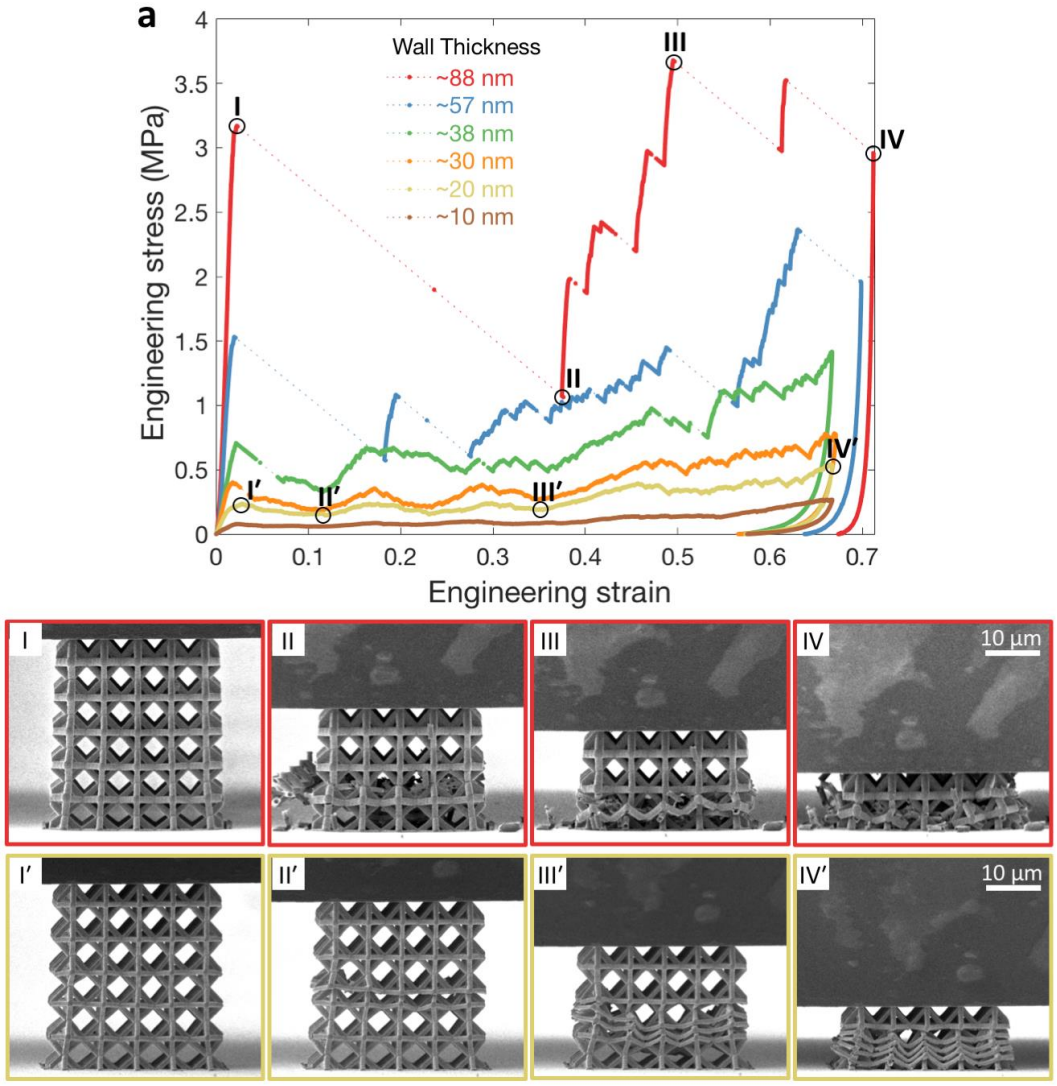

Figure 32. Representative engineering stress-strain data obtained via uniaxial compression to ~67% strain. One representative stress-strain curve for each wall thickness is shown in (a) with data points connected with dotted lines. In-situ images obtained during compression at the points marked in (a) are shown in (I-IV) for the nanolattice with a wall thickness ~88 nm and in (I′-IV′) for the nanolattice with a wall thickness ~20 nm.

These differences in mechanical response are also visualized through Figure 33 (a-f), which display all the stress-strain data grouped by wall thickness under compression to various strains. Figure 33 (a-f) are particularly helpful for visualizing details of the stress-strain data for thinner-walled nanolattices, which are at the low end of the engineering stress scale used in Figure 32 (a). A minimum of 14 nanolattices were compressed for each wall thickness and the

breadth of the data displayed in Figure 33 for each wall thickness demonstrates the consistency and repeatability of these experiments.

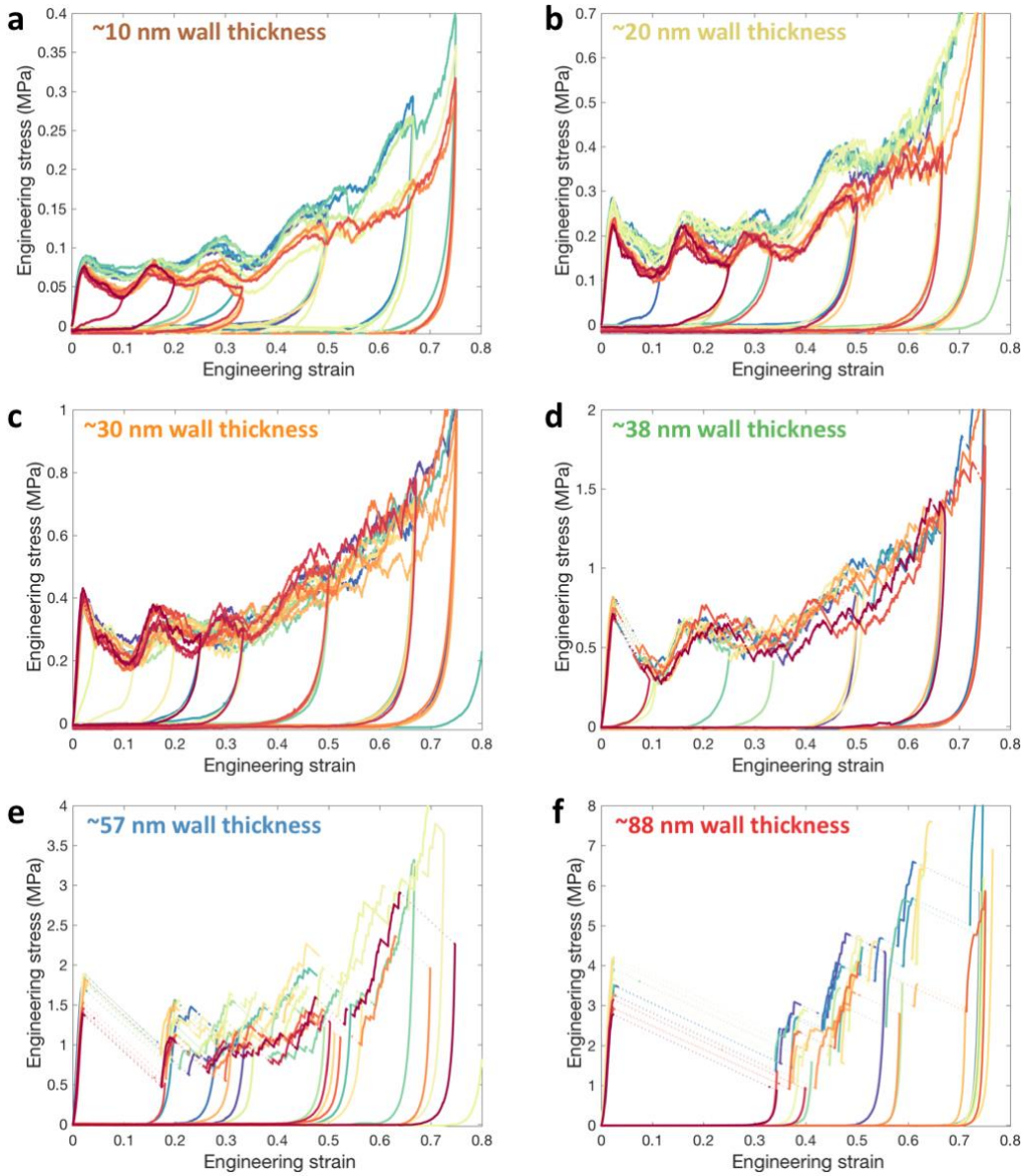

Figure 33. Stress-strain data grouped by nanolattice wall thickness, under compression to a range of strains. The wall thickness of the nanolattice beams for each grouping are (a) 10 nm, (b) 20 nm, (c) 30 nm, (d) 38 nm, (e) 57 nm, and (f) 88 nm. Data points are connected with dotted lines.

The stress-strain data of the thinnest-walled nanolattices, wall thicknesses of ~10 nm (Figure 33 (a)) and ~20 nm (Figure 33 (b)), involve smooth, continuous deformation. The smoothness of deformation in these thin-walled nanolattices can be observed in videos obtained from compression experiments, as shown in Video 8 for the ~10 nm wall thickness and Video 9 for the ~20 nm wall thickness. The presence of three humps in the stress-strain curves over strains ranging from 0-0.4 indicates gradual layer-by-layer collapse. Each hump corresponds to the failure of an individual layer; as an individual layer is strained, it carries load until reaching a peak stress and then the layer collapses gradually, folding up, and the stress decreases. The appearance of layer-by-layer collapse is illustrated in Figure 34, which shows a nanolattice with a wall thickness of ~10 nm after compression to 67% strain and unloading. The layers neatly fold up underneath each other and there is no catastrophic damage to the nanolattice after compression; the beams are still intact with the general structure of the unit cells still apparent.

The failing of individual layers in layer-by-layer collapse always involves the collapse of the beams in the bottom half of each unit cell first while the beams in the top-half of each unit cell are largely unchanged after compression. This likely occurs due to variation in wall thickness that comes about from the directional nature of sputter deposition, which results in thicker-walled beams in the top half of each unit cell. The thinner bottom beams of each unit cell more readily deform than their thicker counterparts, and hence most failure of individual layers is localized to the bottom beams, as visualized in Figure 34.

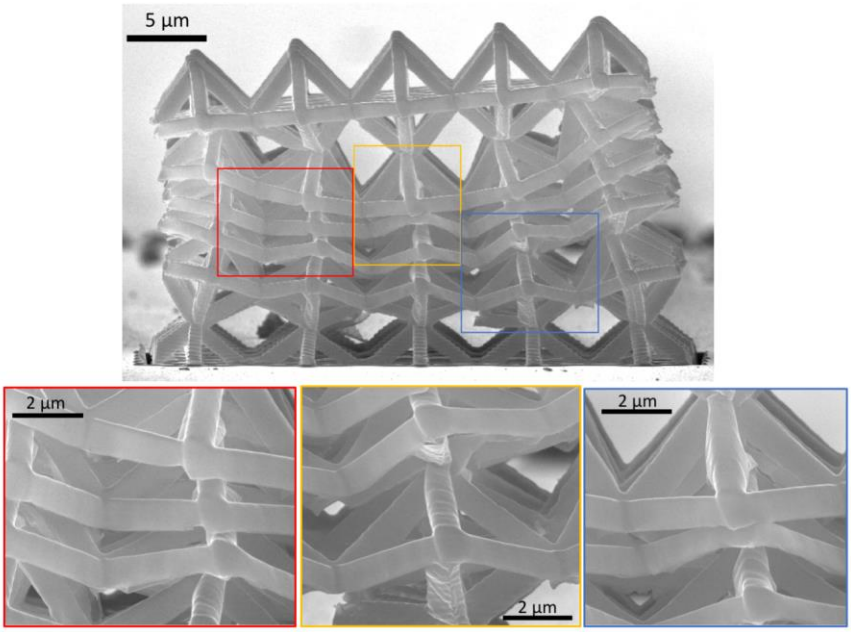

Figure 34. SEM images of a nanolattice with a ~10 nm wall thickness after compression to 67% strain. The colored rectangles in the top image denote the regions for the higher magnification images below. The nanolattice exhibits gradual layer-by-layer collapse. The failed layers neatly fold up and the general structure of the layers is still apparent after compression.

As the wall thickness of the nanolattice beams is increased, the stress-strain response becomes more discontinuous as shown in the stress strain data for the nanolattices with a wall thickness of ~30 nm (Figure 33 (c)) and those with a wall thickness of ~38 nm (Figure 33 (d)). These changes in the mechanical response can be visualized from videos obtained during the compression experiments. Video 10 shows the response of a ~30 nm wall thickness nanolattice and Video 11 shows the response of a ~38 nm wall thickness nanolattice. These intermediate wall thickness nanolattices exhibit some remnants of the characteristic humps of layer-by-layer collapse observed in the thinnest-walled nanolattices (Figure 33 (a, b)); however the humps are not as pronounced, and there is the addition of small strain bursts to the stress-strain data. The strain bursts occur due to rapid failure events, such as a beam breaking or layer of unit cells failing. These rapid failure events often occur too quickly for the nanoindenter to capture data at the 100 Hz data acquisition rate used, resulting in the observed

discontinuities in the stress-strain data. The largest strain burst for these intermediate wall thickness nanolattices occurs immediately after elastic loading and involves some partial failure of a nanolattice layer in a catastrophic manner, unlike the gradual collapse of nanolattice layers observed for the thinnest walled nanolattices, Figure 33 (a, b). After the first failure event in these intermediate wall thickness nanolattices, the deformation commences through smaller strain burst, sometimes referred to as flow serrations in metallic glasses. Each serration can be thought of as a relaxation event associated with the formation of a shear band, recorded as a small strain burst in the stress-strain data. After a single shear band activates and terminates, the nanolattice can be deformed further through successive shear banding events that occur upon subsequent loading.

The thickest-walled nanolattices, wall thicknesses of ~57 nm (Figure 33 (e)) and ~88 nm (Figure 33 (f)), exhibit large discontinuities in the stress-strain data that occur due to sudden failure events and large catastrophic strain bursts that are characteristic of brittle failure. These large failure events can be observed in the videos of compression experiments for the ~57 nm wall thickness nanolattice (Video 12) and the ~88 nm wall thickness nanolattice (Video 13). The catastrophic nature of the failure in these thick-walled nanolattices is also illustrated in Figure 35, which depicts a nanolattice with a wall thickness ~88 nm after compression to 33% strain and unloading. The two layers in the middle of the nanolattice have catastrophically failed with the original structure of those unit cells destroyed and no longer intact as it is for the thinner walled nanolattices, such as the nanolattice shown in Figure 34.

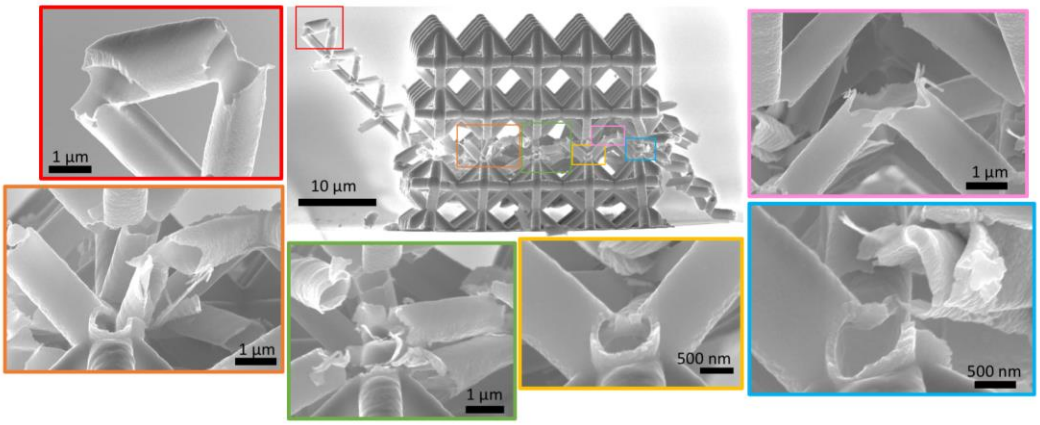

Figure 35. SEM images of a nanolattice with a ~88 nm wall thickness after compression to 33% strain. The colored rectangles in the top-middle image denote the regions for the surrounding higher magnification images. Failure is localized to the two rows of unit cells near the middle of the nanolattice and primarily occurs at the nodes. The failed layers are destroyed and largely unrecognizable after compression.

As the wall thicknesses of the nanolattice beams are varied, the significant changes in the resultant stress-strain responses, particularly after yielding, demonstrate that the wall thickness largely dictates the nature of post-elastic deformation. Following elastic loading, some nanolattices undergo gradual deformation, while others exhibit a sudden failure event or strain burst. By measuring the size of this first strain burst observed after elastic loading, this aspect of post-elastic deformation can be quantified. As illustrated in Figure 33, the nature of this first strain burst is determined by the wall thickness; the thinnest-walled nanolattices, Figure 33 (a, b), exhibit gradual deformation with no strain burst after elastic loading, the nanolattices with intermediate wall thicknesses, Figure 33 (c, d), exhibit a small strain burst following elastic loading, and the thickest-walled nanolattices, Figure 33 (e, f), exhibit a very large strain burst after elastic loading.

Figure 36 depicts these dramatic differences in the first strain burst as the wall thickness of the nanolattice beams is varied. Figure 36 (a-h) contain representative SEM images of the nanolattices that exhibit a first strain burst immediately before and after the strain burst occurs. These images illustrate the regions within the nanolattices that fail as a consequence of the

first strain burst event. The ~30 nm wall thickness nanolattices (Figure 36 (a, b)) fail in the fourth row of unit cells with only a partial collapse of that layer, the ~38 nm wall thickness nanolattices (Figure 36 (c, d)) also fail in the fourth row of unit cells with a larger partial collapse of that layer, the ~57 nm wall thickness nanolattices (Figure 36 (e, f)) fail with complete destruction of the entire fourth row of unit cells, and the ~88 nm wall thickness nanolattices (Figure 36 (g, h)) fail with complete destruction of the entire third and fourth rows of unit cells. The stress-strain data corresponding to the SEM images of Figure 36 (a-h) are included immediately below the SEM images for more quantitative assessment of the stress and strain changes during the first strain burst.

Figure 36 (b, d, f, h) illustrate that failure almost always initiates in the fourth row of unit cells from the top. This likely occurs because the anisotropic sputter deposition results in this row of unit cells having the thinnest walls. The wall thickness of nanolattice beams generally decreases from top to bottom in the nanolattice, however there is a small increase in wall thickness for the bottom layers due to redeposition from the thin film growing on the substrate surface during sputter deposition. The fourth row of unit cells, which is towards the bottom of the nanolattice but not so far down as to have redeposition from the thin film on the substrate, has the thinnest walls, thereby deforming most easily.

Figure 36 (i) displays the average size of the first strain burst as a function of the wall thickness of the nanolattice beams. The average strain burst size was obtained for each wall thickness by measurement from the stress-strain data of individual nanolattices, with a minimum of 16 sets of stress-strain data measured for each wall thickness. The error bars in Figure 36 (i) denote plus/minus one standard deviation. As the thinnest-walled nanolattices (~10 nm and ~20 nm wall thicknesses) had gradual deformation with no strain bursts, the size of the strain burst for nanolattices with those wall thicknesses is shown as 0 in Figure 36 (i).

For the thicker-walled nanolattices (~30 nm wall thickness and greater) as the wall thickness increases, the size of the strain burst increases linearly, as displayed in Figure 36 (i).

It should be noted that the absolute size of the strain burst will depend on the details of the compression test method and controls as well as the dynamics of the mechanical testing instrument used. As all nanolattices in this work were compressed utilizing an identical test method and testing instrument, a direct comparison can be made between the sizes of the strain bursts in the different nanolattices. However, the sizes of these strain bursts may vary with other mechanical testing instruments and test methods; hence, care should be taken in comparing strain burst size in this study with that in another study using disparate testing conditions and instrumentation.

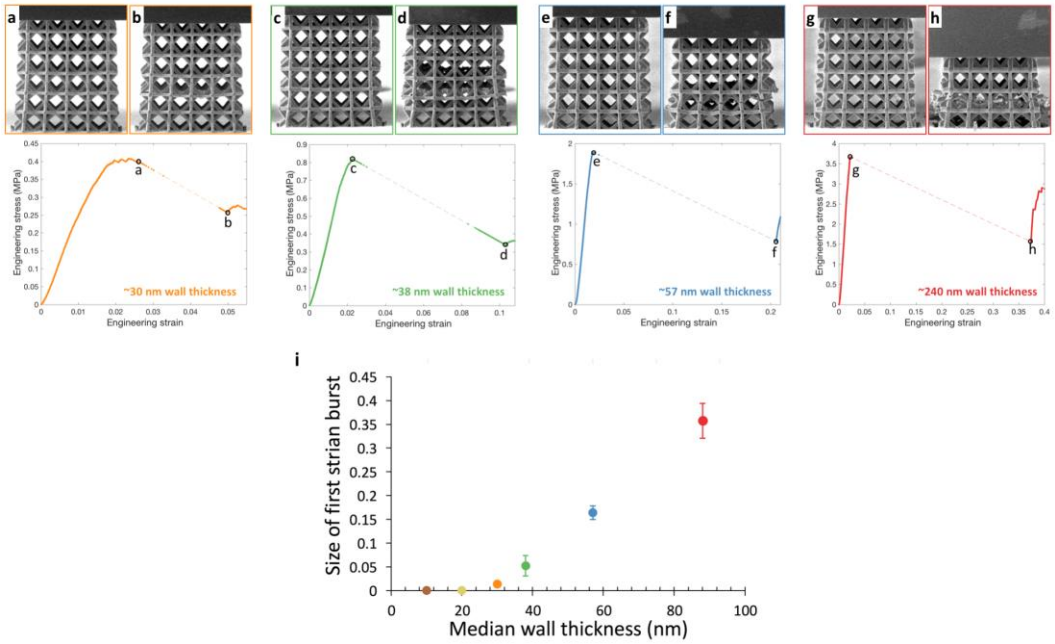

Figure 36. First failure event analysis for nanolattices with different wall thicknesses. Following elastic deformation, thicker-walled nanolattices (~30 nm wall thickness and larger) each exhibit a pronounced strain bursts as demonstrated by the in-situ images shown in (a-h) and the corresponding stress-strain data shown below the images for median wall thicknesses of (a, b) ~30 nm, (c, d) ~38 nm, (e, f) ~57 nm, and (g, h) ~88 nm. The size of the strain burst was measured for at least 16 nanolattices of each wall thickness and the average strain burst size as a function of wall thickness is plotted in (i) with the error bars denoting ± one standard deviation in each measurement.

Another way to assess the nature of post-elastic deformation is by considering nanolattice recovery following compression and unloading. Figure 37 shows the differences in recovery between the thinnest-walled nanolattices, Figure 37 (a, b), and the thickest-walled nanolattices, Figure 37 (c, d), after compression to 33% strain. As discussed previously, the thinnest-walled nanolattices undergo gradual layer-by-layer collapse and the general structure of individual unit cells largely stays intact upon layer collapse. These layers more readily recover, as visualized in Figure 37 (b), than those of the thickest-walled nanolattices, which exhibited catastrophic failure and destruction of the structure making up the failed layers. As the failed layers are nearly completely destroyed by compression, not much recovery is observed for the thickest-walled nanolattices, as shown in Figure 37 (d).

Nanolattices compressed to 33% strain were chosen for measure of recovery because the first strain burst in nanolattices with the thickest walls, Figure 33 (f), resulted in compression to a minimum strain of ~33% as 2 of the 5.5 rows of unit cells failed simultaneously. In addition, it was desirable to measure recovery from a strain that underwent significant plasticity, yet not too much strain that the original nanolattice structure was completely destroyed. The multiple large strain bursts observed in the thickest-walled nanolattices, Figure 33 (e, f), resulted in deformed regions of nanolattices that had little visible resemblance to the original nanolattice structure. Our aim in considering recovery was to investigate the recovery of the nanolattice to a form bearing some resemblance to the initial nanolattice structure, not to investigate the recovery of destroyed and unrecognizable nanolattice fragments.

After compression to 33% strain and unloading, the recovery was measured for a nanolattice of each wall thickness. Recovery was defined as the distance the nanolattice recovered ($\Delta l_{recovered}$) normalized by the distance the nanolattice was compressed ($\Delta l_{compressed}$),

$$recovery = \frac{\Delta l_{recovered}}{\Delta l_{compressed}} \tag{19}$$

where $\Delta l_{recovered}$ is the height of nanolattice immediately after unloading ($h_{after\ unloading}$) less the height of the nanolattice under the maximum compressive strain ($h_{max\ compression}$),

$$\Delta l_{recovered} = h_{after\ unloading} - h_{max\ compression} \quad (20)$$

These recovery measurements are shown in Figure 37 (e) with the emergence of a general trend that recovery decreases linearly with wall thickness. As we chose to focus on recovery after compression to 33% strain, there were limited stress-strain data sets available, and hence the plot in Figure 37 (e) contains only a single data point for each wall thickness.

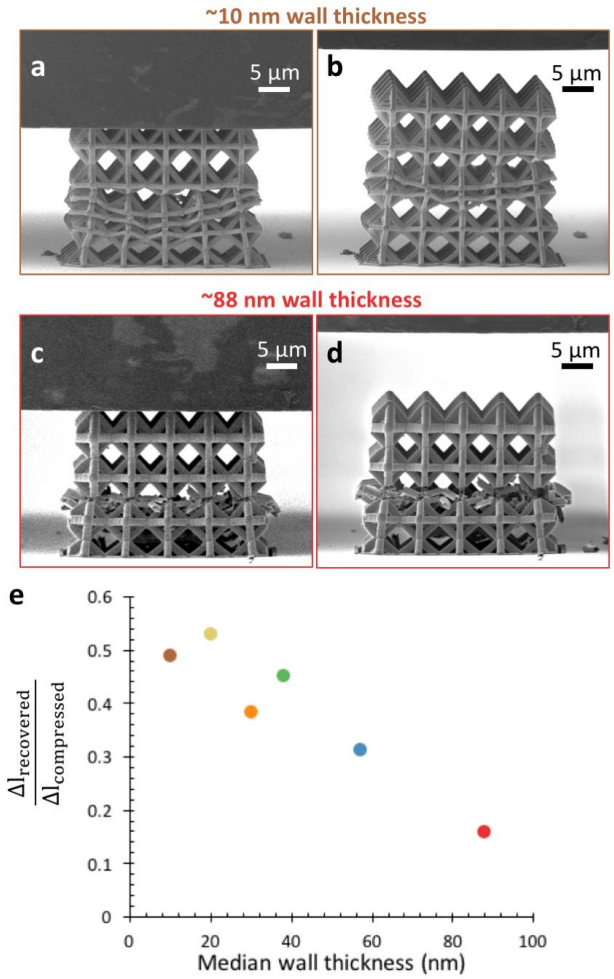

Figure 37. Nanolattice recovery after compression to 33% strain. SEM images shown for nanolattices with a wall thickness of (a, b) ~10 nm and (c, d) ~88 nm. The left images (a) and (c) show the nanolattices at the maximum strain of the compression experiment (~33%) just before unloading. The right images (b) and (d) show the nanolattices immediately after the compression experiment. (e) Plot of recovered height normalized by the compression distance for nanolattices compressed to 33% strain.

Other mechanical properties of interest, the elastic modulus (E) and yield strength (σ_y), were measured by considering the stress-strain response of the nanolattices at low strains. The same stress-strain data plotted in Figure 33 is plotted in Figure 38 over the low strain region of 0-0.05 to illustrate the region of interest for determination of elastic modulus and yield strength. As in the plots of Figure 33 (a-f), the plots in Figure 38 (a-f) contain stress-strained data grouped by median wall thickness but with the data shown over the strain range of 0-0.05 to make the low-strain data more visible. Figure 38 (a-f) each contain a dotted horizontal line denoting the average measured yield strength and a dashed line with slope denoting the average measured elastic modulus for the particular wall thickness of the figure. Methodology for determination of E and σ_y is provided in section 5.2.4.

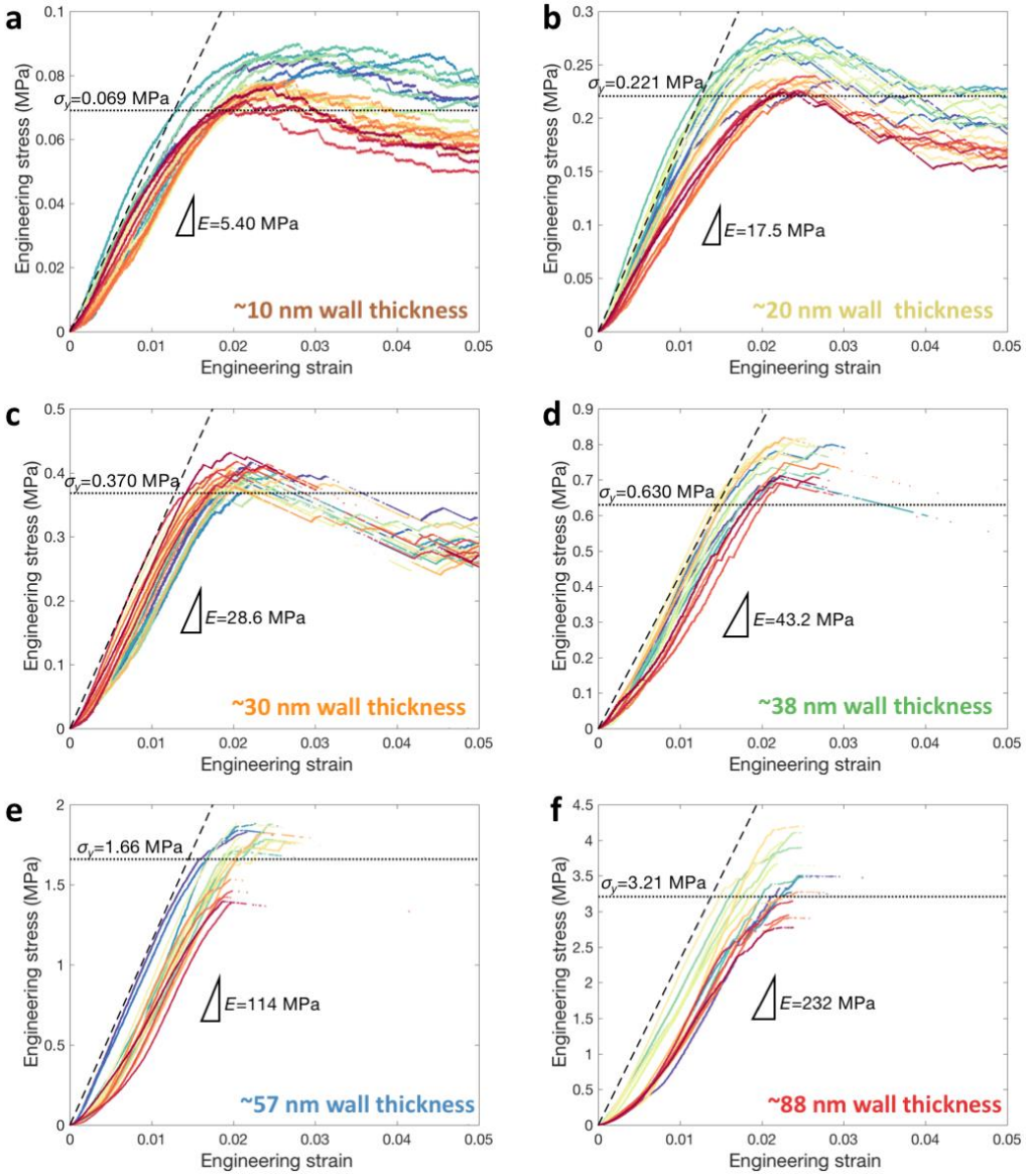

Figure 38. Engineering stress-strain data displayed from 0-0.05 strain with elastic modulus and yield strength measurements. The data is grouped by wall thickness of nanolattice beams with wall thicknesses of (a) 10 nm, (b) 20 nm, (c) 30 nm, (d) 38 nm, (e) 57 nm, and (f) 88 nm. The horizontal dotted lines indicate the average yield strength and the slope of the dashed lines indicate the average elastic modulus for each wall thickness. The presence of large strain bursts in the thicker-walled nanolattices of (d-f) results in large stretches of strain with no data captured, and hence the data appears to cut off at ~0.03 strain.

The average elastic modulus and yield strength for each nanolattice wall thickness, which are noted in Figure 38 (a-f), are plotted in Figure 39 (a, b) as a function of nanolattice relative density. The error bars in these figures denote plus/minus one standard deviation in the

measured property for that wall thickness. Due to the logarithmic scales of the plot, some of the error bars are within the marker size and thus do not appear. Nanolattice relative density was estimated using SolidWorks models of the nanolattice geometry with a uniform wall thickness assumed to be the median wall thickness for each sputter deposition time, as noted in Figure 29 (b).

Although Figure 39 (a, b) show elastic modulus and yield strength plotted as a function of relative density, it should be noted that the large variation in wall thickness in the sputtered nanolattices (discussed in sections 4.2.2 and 4.3.1) makes an accurate determination of a single relative density for each nanolattice unreliable. The relative density is expected to be lower in the regions of the nanolattice with thinner walls, such as the interior and lower regions of the nanolattice, and higher in the regions of the nanolattice with thicker walls, such as the top and outer sides. There are also local variations in wall thickness within a single unit cell (top beams have thicker walls than bottom beams) and within a single beam (the top surfaces of beams have thicker walls than bottom surfaces). Consequently, the relative densities plotted in Figure 39 should only be taken as approximate estimates for the relative densities of the nanolattices.

Plots of elastic modulus and yield strength as a function of relative density are frequently utilized as figures of merit in evaluating and comparing the mechanical properties of cellular solids. Such plots are useful as classic cellular solids theory relates the cellular solid strength (σ) and elastic modulus (E) to relative density ($\bar{\rho}$) through the following scaling relations,

$$E \propto \bar{\rho}^{m} \tag{21}$$

$$\sigma \propto \bar{\rho}^{n} \tag{22}$$

where the exponents m and n depend solely on the fundamental deformation mechanism of the cellular solid architecture, involving either bending or stretching of the lattice beams upon loading [55,172,173]. Stretching-dominated structures scale with $m = n = 1$, stochastic foams scale with $m = 3$ and $n = 2$, and bending-dominated structures scale as $m = 2$ and $n = 1.5$

[55,171,172,174]. The octahedron unit cells of the current work are bending-dominated and would be then expected to exhibit a scaling with relative density ($\bar{\rho}$) that follows the relations,

$$E \propto \bar{\rho}^2 \tag{23}$$

$$\sigma \propto \bar{\rho}^{1.5} \tag{24}$$

As noted in Figure 39 (a, b), the observed scaling of the metallic glass nanolattices in this study are

$$E \propto \bar{\rho}^{1.68} \tag{25}$$

$$\sigma \propto \bar{\rho}^{1.74} \tag{26}$$

The measured experimental scaling exponents of equation (25) and (26) are within the range of the predicted theoretical scaling exponents of equations (23) and (24). However, as the relative densities of the experimental nanolattices were calculated by simply using the median wall thickness as equal to the wall thickness throughout a nanolattice, the relative densities are unreliable, and therefore the scaling exponents that result are also unreliable. Even if the overall relative density of a nanolattice was found in an accurate manner, inevitable variation in relative density throughout a sputtered nanolattice complicates the scaling behavior. Unfortunately, not many conclusions can be drawn from the scaling behavior of nanolattices fabricated by sputtering or other techniques that lead to such large variation in relative density throughout individual nanolattices.

It is instructive to display the elastic modulus and yield strength as a function of density in what are commonly known as material property charts or Ashby plots, which are helpful in materials selection. Such plots are shown in Figure 39 (c, d) with the elastic modulus and yield strength of the metallic glass nanolattices from this chapter overlaid on the property space of existing materials. As can be observed in Figure 39 (c, d), the metallic glass nanolattices fall in the same material property space as foams and span a large range of densities.

For comparison, the elastic modulus and yield strength of bulk sputtered $Zr_{54}Ni_{28}Al_{18}$ metallic glass are also plotted in Figure 39 (c, d) as marked with stars. The bulk yield strength

was determined from the nano-tensile experiments in Chapter 3, which resulted in an average yield strength of 1.26 GPa as shown in Figure 20 (c). The nano-tensile experiments did not show any size dependence of strength so we assume this value is representative of the bulk strength. While the elastic modulus of the as-sputtered metallic glass was also found using the nano-tensile results shown in Chapter 3, the elastic modulus obtained from nano-tensile experiments underestimates the elastic modulus significantly as discussed in section 3.3.3. Therefore, the elastic modulus for the as-sputtered metallic glass was instead determined by nanoindentation on a ~1 μm thin film of the sputtered metallic glass, which resulted in an elastic modulus of 130 GPa utilizing the Oliver-Pharr method [175].

The density used for the plots in Figure 39 (c, d) was calculated by multiplying the assumed bulk density of $Zr_{54}Ni_{28}Al_{18}$ (6481.7 kg m^{-3}) by the nanolattice relative density, determined by SolidWorks models as described above. The anisotropic nature of sputter deposition leads to variation in wall thickness throughout each nanolattice which makes accurate determination of relative density difficult, as discussed above. Therefore, the densities plotted for the metallic glass nanolattices in Figure 39 (c, d) should be taken only as estimates useful for showing the approximate location of the metallic glass nanolattices in material property space relative to other materials.

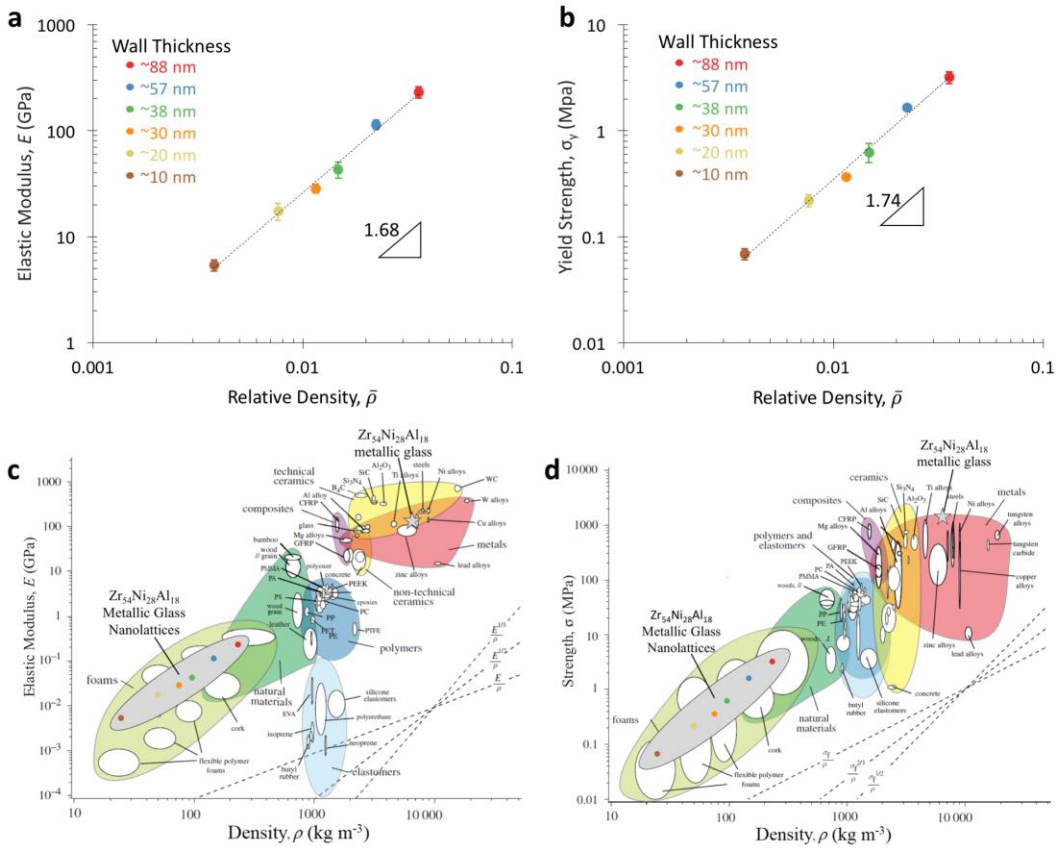

Figure 39. Elastic modulus and strength versus density of metallic glass nanolattices. (a) Elastic modulus and (b) yield strength are plotted versus relative density with the error bars denoting ± one standard deviation in the measured property. (c, d) Material property plots of elastic modulus and strength versus density for existing materials. The hollow metallic glass nanolattices are shown in the gray oval with each point corresponding to the average measured property from all the nanolattices of a certain sputter deposition time. The properties of bulk $Zr_{54}Ni_{28}Al_{18}$ metallic glass (the constituent material of the nanolattices) are also plotted for reference and marked with a star. The directional nature of sputter deposition makes the relative density and density values unreliable and should thus only be taken as approximate. (c, d) are modified from [172] with permission.

4.4. Discussion

The nanolattices in this study exhibit a mechanical response that is a result of a combination of structural effects from the nanolattice geometry and material size effects from the constituent metallic glass. In order to gain a complete understanding of why the observed brittle-to-deformable transition occurs as wall thickness is reduced, it is important to evaluate

whether structural effects, material effects, or some combination of the two are relevant in determination of the nanolattice mechanical response.

4.4.1. Nanolattice structural effects

The arrangement of the metallic glass in the highly ordered, repeating structure of octahedron unit cells necessitates the consideration of potential failure mechanisms resulting from the structure. Following the work of Meza et. al [161], failure of the nanolattice structure (without consideration for the metallic glass material size effect) will result from the combinations of three potential mechanisms: material yielding, local shell buckling, and Euler beam buckling. These failure mechanisms can be defined from [176] as:

$$\sigma_{yield} = \sigma_y \tag{27}$$

$$\sigma_{shell} = \frac{E}{\sqrt{3(1-\nu^2)}}\left(\frac{t}{r}\right) \tag{28}$$

$$\sigma_{beam} = \frac{\pi^2 EI}{(kL)^2 A_{beam}} \tag{29}$$

where σ_y, E, and ν are the yield strength, elastic modulus, and Poisson's ratio of the constituent metallic glass, respectively. k is a constant based on the boundary condition of the beam, which can be taken as ~0.6 for the octahedron geometry of this work [177]. L is the beam length, t is the beam's wall thickness, A_{beam} is the cross-sectional area of the beam, and I is the area moment of inertia for the beam. For the thin-walled approximately circular beams of this work, these parameters are given by

$$A_{beam} = 2\pi rt \tag{30}$$

$$I = \pi r^3 t \tag{31}$$

Substituting equations (30) and (31) into equation (29) we find the buckling failure criterion for the beams is given by

$$\sigma_{beam} = \frac{25}{18}\pi^2 E\left(\frac{r}{L}\right)^2 \tag{32}$$

As discussed by Meza et. al [161], for the nanolattice structures there are two failure mechanisms: yielding versus local shell buckling and yielding versus Euler beam buckling. These failure mechanisms may act in combination or independently. Yielding will occur under tension and buckling will occur under compression [161]. The complex stress-state in the hollow beam nanolattice structure leads to certain beams and regions under compression while other beam and regions are under tension [161]. For example, in the octahedron unit cells making up the nanolattices of this work, the four horizontal beams are largely under tension while the eight vertical beams are largely under compression. Further, the bending of hollow beams near the nodes leads to complex stress-states near the nodes involving local compression and tension on different sides of individual beams. Assuming the compressive and tensile stresses in the nanolattice are roughly equal, which is reasonable for beams in bending [161], the critical transition criteria between the failure mechanisms can be found by setting the failure equations equal to each other, such that equation (27) is set equal to equation (28), to find the transition between yielding and local shell buckling,

$$\sigma_{yield} = \sigma_{shell} \longrightarrow \left(\frac{t}{r}\right)_{crit} = \frac{\sigma_y}{E}\sqrt{3(1-\nu^2)} \tag{33}$$

Similarly, equation (27) is set equal to equation (32) to find the transition between yielding and Euler beam buckling,

$$\sigma_{yield} = \sigma_{beam} \longrightarrow \left(\frac{r}{L}\right)_{crit} = \frac{3}{5\pi}\sqrt{\frac{2\sigma_y}{E}} \tag{34}$$

The above equations (33) and (34) are only functions of the constituent properties for the bulk Zr-Ni-Al metallic glass, which makes up the nanolattices. As discussed in section 4.3.2 in reference to the material property charts of Figure 39, the bulk properties for yield strength and elastic modulus of the sputtered metallic glass were measured as 1.26 GPa and 130 GPa respectively. Poisson's ratio for the metallic glass was assumed to be 0.36 as Poisson's ratio for Zr-based metallic glasses have been reported to range from 0.35-0.37 [178]. Substituting

these values for the mechanical properties of the metallic glass into equations (33) and (34), the critical local shell buckling transition is found to occur at $(t/r)_{crit} = 0.016$ and the critical Euler beam buckling transition is found to occur at $(r/L)_{crit} = 0.027$. Considering only these structural effects, nanolattice structures with geometrical values of wall thickness (t), beam radius (r), and beam length (L) such that (t/r) and (r/L) are greater than these critical ratios would be expected to fail by yielding with no structural buckling.

Considering local shell buckling, the nanolattices with the thinnest walls (median wall thickness ~10 nm) would be most susceptible to shell buckling. These thinnest-walled nanolattices have (t/r)=(10 nm/400 nm)=0.025, which is greater than the critical value for shell-buckling of $(t/r)_{crit} = 0.016$, and therefore no nanolattices in this work would be expected to exhibit local (shell) buckling. Considering Euler beam buckling, the nanolattices of the geometry in this study contain (r/L) = (0.4 μm/4.9 μm) = 0.081, which is greater than the critical value for Euler beam buckling of $(r/L)_{crit} = 0.027$, and thus no nanolattices in this work would be expected to exhibit Euler beam buckling. These calculations reveal that the structure of the nanolattices in this work is such that local shell buckling and Euler beam buckling are suppressed, and the only mechanism of failure is yielding. As a result, the metallic glass material of the nanolattice, as opposed to the structure of the nanolattice, determines the dominant failure behavior.

4.4.2. Material size effects in metallic glasses

The structural analysis in section 4.4.1 demonstrates that the geometry of the structure is not within the range where Euler beam buckling or local (shell) buckling is expected. This indicates the observed changes in deformation behavior from brittle catastrophic failure in thick-walled nanolattices to deformable ductile-like behavior in thin-walled nanolattices are due to the constituent metallic glass material of the nanolattice. The observed brittle-to-ductile

transition that occurs as the wall thickness of nanolattice beams decreases is analogous to the brittle-to-ductile transition that has been frequently observed as the sample diameter is reduced in metallic glass nanopillars. As discussed in sections 1.2.2 and 3.4.2 the "smaller is more ductile or deformable" size effect frequently observed in metallic glass nanopillars has predominantly been rationalized by the high surface-to-volume ratio in nanopillar samples, which increases the energetic cost of a shear band compared to homogeneous deformation [24,38,40]. The new insight from the work in this chapter is the proof of concept that this beneficial size effect can indeed be proliferated to larger potentially more useful structures, such as nanolattices, as long as a high surface-to-volume ratio is maintained by keeping the metallic glass nanolattice wall thickness small.

4.5. Summary and outlook

In summary, we have demonstrated the fabrication of hollow metallic glass nanolattices with the constituent metallic glass deposited by sputtering. The sputter deposition was conducted for various times to result in nanolattices with different wall thicknesses, with the nanolattice median wall thickness ranging from 10 nm in the thinnest-walled nanolattices to 88 nm in the thickest-walled nanolattices. Uniaxial compression experiments performed inside of an SEM revealed a brittle-to-deformable transition as the nanolattice wall thickness is reduced. Thick-walled nanolattices exhibited large catastrophic strain bursts involving failure of multiple nanolattice layers simultaneously. Thin-walled nanolattices exhibited no strain bursts, instead undergoing smooth continuous deformation, with gradual layer-by-layer collapse and substantial recovery upon unloading. Structural analysis indicates all nanolattices in this study are outside the regime of Euler beam buckling or local (shell) buckling, indicating the failure mode in the nanolattices of this study can be attributed to the constituent metallic glass material and not the nanolattice structure. The observed brittle-to-deformable transition

as wall thickness is reduced can be understood in terms of the "smaller is more ductile or deformable" size effect that has frequently been observed in individual metallic glass nanopillars.

4.5.1. Implications for nano-architected metallic glass

The work discussed in this chapter is one of the first studies aimed towards understanding the mechanical behavior of metallic glass nanolattices and serves as proof of concept that the "smaller is more deformable" size effect first observed in metallic glass nanopillars can be extended to larger systems through nano-architecting. This work also demonstrates that metallic glass nanolattices can be thought of as having tunable mechanical properties where parameters such as the wall thickness can be adjusted to achieve a desired mechanical response. In this study, we were able to transition the mechanical response from catastrophic layer failure to a deformable, gradual layer-by-layer collapse by reducing the wall thickness of the nanolattices. This reduction in wall thickness also came with a significant sacrifice in strength. Hence, adjusting the wall thickness of metallic glass nanolattices is not able to tune the resultant mechanical response in a way the reaches the desirable property space of deformable and strong. Further optimization for parameters such as nanolattice geometry, metallic glass deposition method (particularly to create a more uniform wall thickness within each nanolattice), and constituent metallic glass may result in metallic glass nanolattices with improved mechanical properties and elucidate additional knobs for tuning the mechanical response of nano-architected metallic glass. With new knobs we may be able to reach new property spaces and design metallic glass nanolattices that are both deformable and strong.

The material property charts illustrate that the metallic glass nanolattices fall within the existing property space for foams and do not reach new property space in the desirable region of low density with high modulus and strength. The focus of this work was on understanding

whether the "smaller is more deformable" size effect can be proliferated to these larger nanolattice structures. However, the actual nanolattice geometry was not optimized and the structural analysis conducted in section 4.4.1 demonstrated that structural effects were not contributing to the enhanced deformability of the metallic glass nanolattices. Ordered periodic cellular solids have been shown to have higher elastic modulus and compressive yield strength compared to stochastic foams [61] and also even compared to bulk materials [179]. Therefore, it is likely that with further optimization of the structure, such as using a stretching (as opposed to bending) dominated structure or utilizing beam geometries that favor buckling and deformability with thicker, stronger walls, both material size effects and structural effects could combine to enhance the mechanical response. In this way, it may be possible to design metallic glass nanolattices reaching the untapped target region in material property space of low density with high modulus and strength.

Chapter 5. Irradiation enhances deformability and strengthens metallic glass nanolattices

Adapted from:

R. Liontas, Y. Wang, J.R. Greer. "Irradiation enhances deformability and strengths metallic glass nanolattices" (in preparation).

We present experiments investigating the effects of 12 MeV Ni^{2+} ion irradiation on hollow metallic glass nanolattices. Upon irradiation, nanolattices with median wall thicknesses of 57 nm and less exhibited a significant contraction of the nanolattice structure; only the thickest-walled nanolattices, those with a median wall thickness of ~88 nm, were able to withstand irradiation without significant contraction. Compression experiments were only conducted on these thickest-walled nanolattices, which did not exhibit major structural contraction upon irradiation. These nanolattices responded favorably to irradiation as measured by mechanical properties, with an average increase in yield strength of 35.7% and a significant enhancement in deformability. Enhanced deformability upon irradiation was apparent from the nanolattices' accommodation of larger strains before any kind of failure event, as well as the presence of smaller strain bursts and stress drops throughout the stress-strain response. Further, the structure of the irradiated nanolattices was largely intact after compression, with SEM images demonstrating a layer-by-layer like collapse as opposed to the catastrophic failure with complete destruction of the failed layers observed in the as-fabricated nanolattices. This work points to irradiation as a promising technique to improve the mechanical response of metallic glass nanolattices. However, caution must be taken as the significant contraction observed in the thinner-walled nanolattices suggests such low density materials may only respond favorably to a certain threshold of irradiation.

5.1. Motivation

This chapter builds upon and unites the irradiation of metallic glass nanopillars discussed in Chapter 2, the tunable nature of metallic glass mechanical response discussed in Chapter 3, and the effect of wall thickness on deformation mechanisms in metallic glass nanolattices discussed in Chapter 4. Chapter 4 revealed that deformability in metallic glass nanolattices can be brought about by reducing the wall thickness of the nanolattice beams, which also led to a substantial loss in strength, as shown in Figure 39 (b). The open question is then how to achieve deformable and strong metallic glass nanolattices. The takeaway message from Chapter 3, that metallic glasses have tunable mechanical properties influenced by such factors as fabrication conditions, critical dimension, and annealing, suggests that further tuning may lead to strong, deformable metallic glass nanolattices. The finding of Chapter 2, that the ductility of metallic glasses can be improved by irradiation without a sacrifice in strength, suggests a specific tuning pathway to achieve strong, deformable metallic glass nanolattices: start with a thick-walled strong metallic glass nanolattices and irradiate to bring about deformability.

While studies into the effects of irradiation on metallic glasses have been common (see section 1.2.1), studies involving the effects of irradiation on cellular solids have been quite limited. Most studies to date have focused on evaluating the radiation tolerance of stochastic nanoporous Au and Ag foams [180-184], where the abundance of surfaces in porous materials have the potential to serve as sinks for radiation-induced defects. Such studies report a window in parameter space of dose rate and ligament diameter where these metallic foams exhibit radiation tolerance [180]. Outside that window, the irradiated metallic nanofoams can exhibit ligament melting and breaking if the ligaments are too small and an accumulation of defects, particularly stacking fault tetrahedra, if the ligaments or the dose rate are too large [180-182].

To the author's knowledge, this is the first study on effects of irradiation in any type of metallic glass cellular solid. As metallic glasses are amorphous, there are no crystalline defects as in metals. Thus, the mechanism of free surfaces serving as sinks for radiation-induced defects, discussed in previous studies on metallic nanofoams [180-184], no longer applies. While metallic glass nanolattices, like nanoporous metals, have an abundance of free surfaces, the disparate atomic structure between metallic glasses and crystalline metals means the current study is embarking into unexplored material space, where mechanisms are still unknown.

5.2. Methods

5.2.1. Fabrication of hollow metallic glass nanolattices

The hollow metallic glass nanolattices of this study were fabricated using an identical process to that discussed in section 4.2.1. As in Chapter 4, the sputter deposition was varied at times of 15, 30, 45, 60, 120, and 240 minutes to achieve the same wall thicknesses shown in Figure 29 (b). Only the thickest-walled nanolattices, those fabricated with the longest sputter deposition time of 240 minutes, were able to undergo irradiation without significant collapse or contraction of the nanolattice structure. Therefore, only those nanolattices fabricated with that longest sputter deposition time of 240 minutes, which corresponds to a median wall thickness of ~88 nm, are the main focus of this chapter. These ~88 nm wall thickness nanolattices exhibited the most catastrophic failure of all the wall thicknesses investigated in Chapter 4. Unless noted otherwise, all results and discussions that follow are referring to the ~88 nm median wall thickness nanolattices, not the thinner-walled nanolattices which significantly contracted upon irradiation.

5.2.2. Irradiation conditions

The nanolattices were irradiated using the tandem ion accelerator at the Ion Beam Materials Laboratory located at Los Alamos National Laboratory. The goal of this study was to investigate irradiation effects and the general influence of bombardments with minimal implantation of the irradiation ions. The ion irradiation was conducted with Ni^{2+} as the chosen ion. As the metallic glass of the nanolattices is $Zr_{54}Ni_{28}Al_{18}$, irradiating with Ni is self-ion irradiation. The irradiation was performed top down, as shown in Figure 40 (a). Irradiation conditions were chosen to ensure that nearly all Ni^{2+} ions passed through the nanolattices to facilitate study of irradiation effects, as opposed to implantation effects. The energy of the Ni^{2+} ions was 12 MeV and the irradiation was conducted to reach a fluence of 6×10^{14} ions cm^{-2} at a dose rate of 1.6×10^{10} ions cm^{-2} s^{-1}. The irradiation was performed at room temperature with the sample stage cooled by gas flow. The temperature of the stage was 25°C prior to irradiation and was monitored throughout the irradiation procedure. During irradiation, the stage reached a maximum temperature of only 27°C, though it is still possible the irradiation caused some local heating in the nanolattice samples.

The Stopping and Range of Ions in Matter (SRIM) Monte Carlo-based simulation software was utilized to evaluate the Ni^{2+} ion penetration and resultant damage from the irradiation, with calculation results displayed in Figure 40 (b, c). These SRIM calculations were conducted using the Kinchin-Pease model, the assumed bulk density for $Zr_{54}Ni_{28}Al_{18}$ (6.4817 g cm^{-3}), and the default threshold displacement energy of 25 eV for Zr, Ni, and Al. From the SRIM calculations, the resultant Ni concentration and displacements per atom (dpa) profiles were obtained as a function of the penetration depth into bulk amorphous $Zr_{54}Ni_{28}Al_{18}$ (left vertical axis on the plots in Figure 40). As shown in the Ni concentration plot, Figure 40 (b), the Ni ions penetrate to reach a peak concentration of 0.0067 at. % at a penetration depth of about 4 μm into bulk amorphous $Zr_{54}Ni_{28}Al_{18}$. As shown in the dpa plot, Figure 40 (c), the

resultant dpa reaches a maximum of ~1 dpa. The ion concentration and dpa in Figure 40 (b, c) are plotted against both the penetration depth into bulk amorphous $Zr_{54}Ni_{28}Al_{18}$ (left vertical axes) and the penetration depth into $Zr_{54}Ni_{28}Al_{18}$ nanolattices (right vertical axes).

To obtain the penetration depth into the nanolattices, the penetration depth into bulk was divided by the estimated relative density of the 240-minute sputter deposited nanolattices, which was 0.05. The relative density of the nanolattice was calculated from SolidWorks models with the specified nanolattice dimensions discussed in section 4.2.1 and a wall thickness of 114 nm, the average wall thickness of the as-fabricated nanolattices formed by 240-minute sputter deposition, as shown in Figure 29 (b). For this calculation the average wall thickness was chosen instead of the median wall thickness because the average is more representative of the relative density of the total nanolattice. In contrast, the median is more representative of the wall thickness relevant for the sections of nanolattice undergoing mechanical deformation. Considering the concentration and dpa profile plots as a function of penetration depth into the nanolattice (Figure 40 (b, c) right vertical axes), it is apparent that the majority of the incoming Ni^{2+} ions penetrate well beyond the depth of the nanolattices. The maximum concentration of Ni^{2+} resulting from the irradiation is 1.1×10^{-4} at. %. in the depth range of the nanolattices (0-36 μm on the right vertical axis). The average dpa in the depth range of the nanolattices is 0.246 ± 0.064. The peak Ni concentration and dpa are low due to the low fluence of 6×10^{14} ions cm^{-2} utilized in this study. The fluence was kept at this low level in an effort to prevent the low density nanolattice structures from being destroyed by the high energy irradiation.

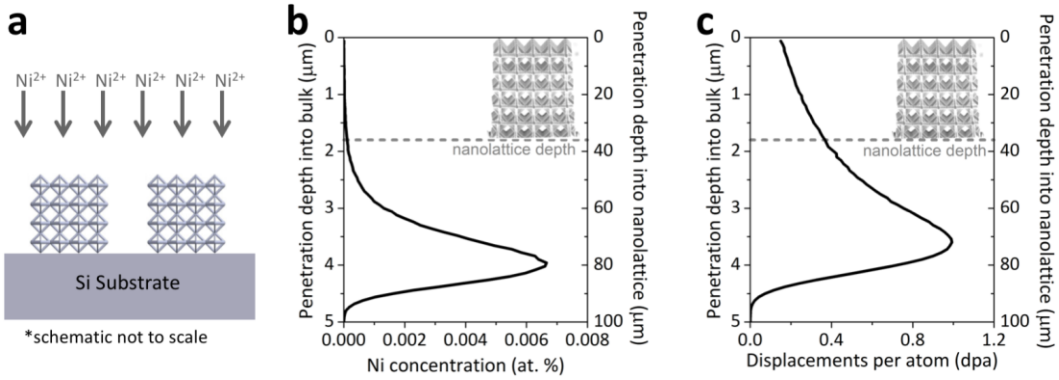

Figure 40. Irradiation schematic and SRIM calculations for Ni^{2+} into $Zr_{54}Ni_{28}Al_{18}$ nanolattices. (a) schematic showing the top-down direction of the irradiating Ni^{2+} ions with respect to the nanolattices and Si substrate. (b) Ni concentration resulting from the Ni^{2+} ion irradiation as calculated by SRIM. (c) Irradiation damage as measured by displacements per atom (dpa) calculated by SRIM.

5.2.3. Characterization conditions

A similar SEM-FIB cross-section procedure as that used to assess nanolattice wall thickness in Chapter 4 was utilized on irradiated nanolattices to assess changes in the nanolattice geometry upon irradiation. As discussed in section 4.2.2, this SEM-FIB cross-section procedure involved using FIB to remove regions of the nanolattices, thereby exposing various cross-sections from which the wall thickness and inner beam dimensions of the exposed beams could be measured via SEM. These cross-sectional cuts and the corresponding measurements were performed at six different locations in each measured nanolattice, ranging from the outermost edge to the most interior unit cells in order to assess the variation in geometry from outside to inside. For each cross-sectional cut, ~20 measurements of wall thickness were obtained on beams favorably oriented with the ~52° tilt of the SEM stage utilized for FIB operation. With these six cross-sectional cuts and 20 measurements for each cut, there was a representative sample of ~120 wall thickness measurements spanning the entire nanolattice from which the median and average wall thicknesses were determined. Similarly, the vertical (major) axes and horizontal (minor) axes of the slightly elliptical shaped beams making up the nanolattices were also measured for each of the six cross-sectional cuts.

From each cross-sectional cut, ~5 measurements of each beam axis were obtained on beams favorably oriented with the ~52° tilt of the SEM stage utilized for FIB operation. With these six cross-sectional cuts and 5 measurements from each cut, there was a representative sample of ~30 beam axis measurements on each of the vertical and horizontal beam axes spanning the entire nanolattice from which the average beam dimensions were determined. This identical measurement procedure was conducted on nanolattices in the as-fabricated and irradiated states to facilitate direct comparison.

XRD was performed on as-fabricated, irradiated, and annealed samples, which each were on a substrate of (100) Si. For each of these samples, Zr-Ni-Al metallic glass had been sputter deposited for 240 minutes, which led to a film thickness of ~1 μm on the Si substrate. In addition to the sputtered film on the substrate, the as-fabricated sample contained 17 nanolattices, which had undergone all the fabrication steps shown in Figure 27, and the irradiated sample contained 34 nanolattices, which had also undergone all fabrication steps shown in Figure 27 in addition to irradiation under the conditions described in section 4.2.1. The annealed sample contained only the ~1 μm thin film of sputtered metallic glass with no nanolattices. The annealed sample was prepared by annealing the sputtered thin film sample in a Carbolite tube furnace at 850 K (~$1.1T_g$) for 3 hours under a 5 LPM flow of Ar to prevent oxidation. The annealed sample was used as a reference point for expected crystallization peaks to evaluate whether crystallization had occurred in the as-fabricated or irradiated samples. The XRD used was a Bruker D2 Phaser using Cu Kα x-rays.

The microstructure of an irradiated metallic glass nanolattice was examined by transmission electron microscopy (TEM). The TEM sample was prepared from a nanolattice fabricated by sputter deposition for 240 minutes, after all the fabrication steps shown in Figure 27 and irradiation under the conditions discussed in section 5.2.2. The nanolattice was transferred to the post of a TEM grid (PELCO, FIB lift out TEM grid) using a

micromanipulator, secured with silver conductive epoxy (H2OE EPO-TEK, Ted Pella, Inc.) and allowed to cure at room temperature. Unit cells of the nanolattice were then removed by FIB to expose single beam walls of the irradiated nanolattice for examination by TEM. TEM was performed using a 300 keV TEM (TF30, FEI Co.).

5.2.4. Uniaxial compression experiments

The uniaxial compression experiments in this chapter were conducted in an identical manner as those in Chapter 4, which were discussed in detail in section 4.2.4. In this chapter, the size of the first stress drop occurring after elastic loading was also measured. The size of the first strain burst and the corresponding stress drop were measured for each data set using MATLAB to find the range of strain and stress around the first strain burst over which the stress was continually decreasing. The range of strain over which the stress was continually decreasing was taken as the strain burst size, and the range of stress over which the stress was continually decreasing was taken as the stress drop size.

The mechanical data shown in this chapter were taken from a single sample of nanolattices all fabricated on the same Si chip to ensure that each nanolattice on that sample underwent identical fabrication steps. Prior to irradiation, nanolattices on that sample were compressed to obtain the mechanical data in the "as-fabricated" state referred to in this chapter, and some nanolattices were left untested. Then that sample was irradiated and those untested nanolattices were then compressed to obtain the mechanical data in the "irradiated" state referred to in this chapter. This enabled direct comparison between "as-fabricated" and "irradiated" nanolattices which underwent identical fabrication conditions. The average elastic modulus, yield strength, strain burst, and stress drop were calculated from a minimum of 10 sets of compression data for each of the "as-fabricated" and "irradiated" nanolattice groups.

5.3. Results

5.3.1. Changes in nanolattice structure upon irradiation

As discussed in section 5.2.1, hollow metallic glass nanolattices for irradiation were fabricated with the same sputter times (15, 30, 45, 60, 120, 240 minutes) and resultant wall thicknesses (10, 20, 30, 38, 57, 88 nm) of Chapter 4. However, only the thickest walled nanolattices (240-minute sputter deposition, ~88 nm median wall thickness) were found to endure the irradiation without dramatic contraction of the nanolattice structure. Figure 41 (b-f) displays the SEM images of the thinner-walled nanolattices (~57 nm median wall thickness and less) following irradiation. For comparison, Figure 41 (a) contains an image of a typical nanolattice before irradiation to illustrate the dramatic changes in nanolattice structure that occurs upon irradiation. The contraction is most severe in the thinnest walled nanolattices (wall thickness ~10 nm) pictured in Figure 41 (b) and becomes less severe as the nanolattice wall thickness is increased from (b) to (f). As all of the thinner-walled nanolattices pictured in Figure 41 (b-f) underwent such significant contraction, they were not further characterized or compressed. The focus of the remainder of this chapter, including characterization and all mechanical experiments, will be on the ~88 nm median wall thickness nanolattices, which did not exhibit such a significant contraction upon irradiation.

The observed contraction in nanolattices upon irradiation suggests that irradiation induced the metallic glass nanolattices to enter a liquid-like state. In this liquid-like state, the nanolattices may have exhibited some flow behavior, where capillary forces caused the thinner walled nanolattices beams to contract. A detailed analysis of irradiation-induced flow is beyond the scope of this work. Further, the variation of wall thickness within each nanolattice complicates quantification of the flow behavior through a viscosity measurement.

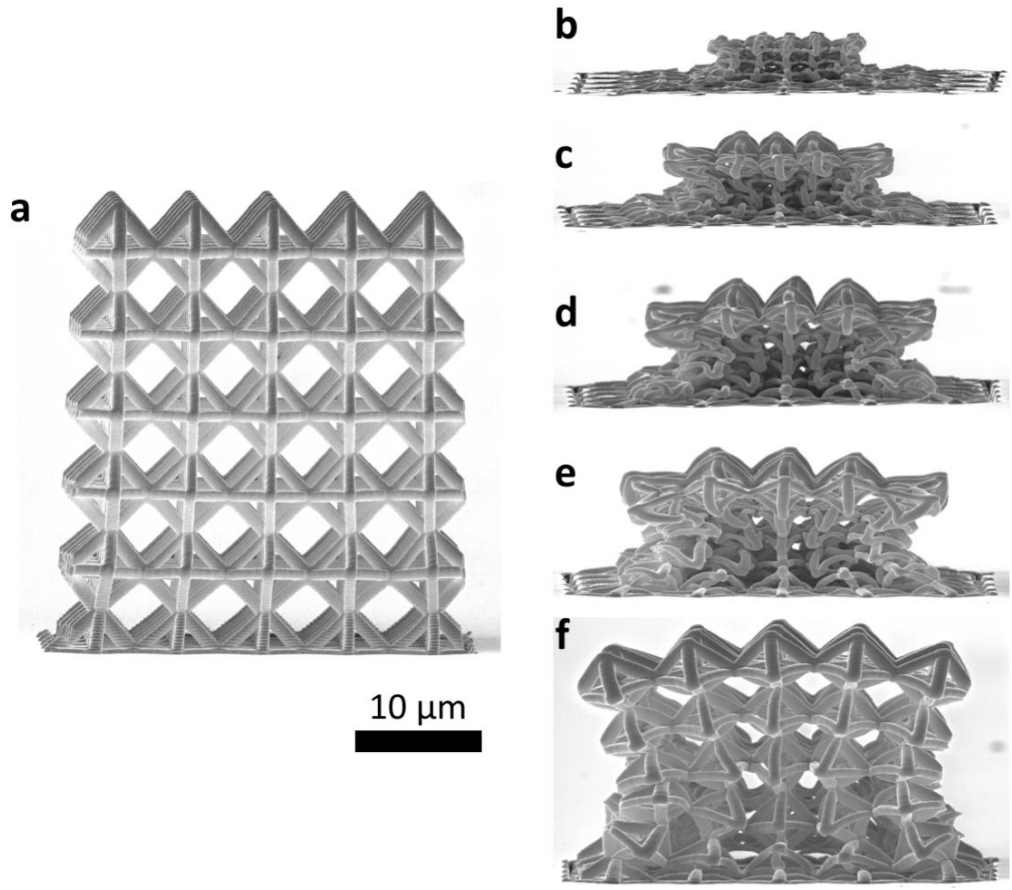

Figure 41. Contraction of thinner-walled nanolattices upon irradiation. SEM images of nanolattices were taken with a ~87° stage tilt and the 10 µm scale bar applies to all images. (a) Typical nanolattice with ~38 nm median wall thickness prior to irradiation. (b-f) Nanolattices after exposure to irradiation have undergone various degrees of contraction. The original wall thicknesses of the nanolattices prior to irradiation were (b) 10 nm, (c) 20 nm, (d) 30 nm, (e) 38 nm, (f) 57 nm. The contraction becomes less severe as the wall thickness is increased from (b) to (f).

Following irradiation, the ~88 nm median wall thickness nanolattices, which did not undergo the dramatic contraction of the thinner walled nanolattices pictured in Figure 41, were thoroughly imaged by SEM to evaluate any slight changes in the nanolattice structure resulting from irradiation. Some of these images are displayed in Figure 42, from a top-down view and from a side view with the nanolattices tilted to ~87°. Viewed from top-down and from the side, it appears that the outer nanolattice beams increased in size upon irradiation. From the side view, there is also some contraction in the overall nanolattice structure upon

irradiation, although it is not nearly as severe as the contraction in the thinner-walled nanolattices pictured in Figure 41. Measurements from SEM images reveal that the nanolattice width is largely unchanged upon irradiation; however the average nanolattice height decreases by 13.6% upon irradiation from 36.4 ± 0.12 μm in the as-fabricated nanolattices to 31.5 ± 0.18 μm in the irradiated nanolattices. The apparent changes in nanolattice structure upon irradiation warrant the SEM-FIB cross-sectional measurement procedure, discussed in section 5.2.3, to evaluate changes in both the inner beam dimensions and the wall thickness throughout the nanolattices as a result of irradiation.

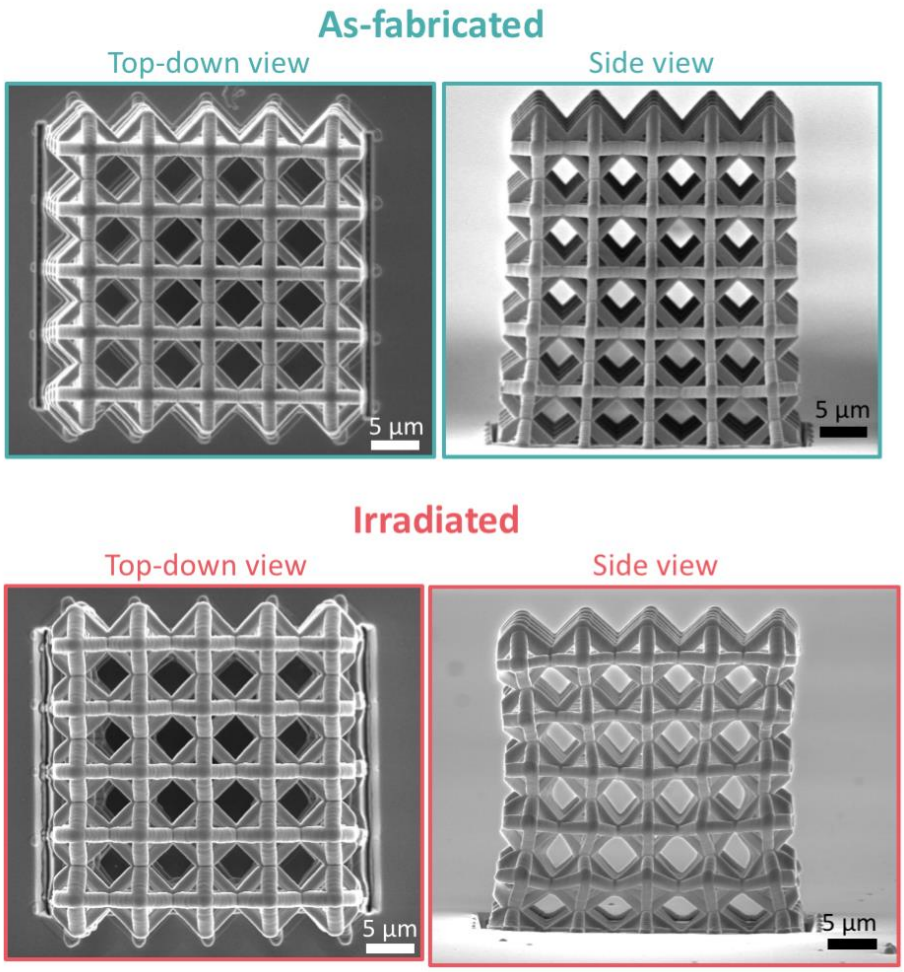

Figure 42. SEM images of representative nanolattices in the as-fabricated and irradiated states. Views are shown from the top-down and the side. The original median wall thickness of the as-fabricated nanolattices and the irradiated nanolattices prior to irradiation was ~88 nm.

Cross-sectional SEM images from the nanolattices in the as-sputtered and irradiated states are displayed Figure 43. These images were obtained by using FIB to remove outer unit cells and expose the internal beams of the nanolattices, as discussed in section 5.2.3. The images are taken with the ~52° stage tilt convenient for FIB operation. These images demonstrate that the internal nanolattice beams have thinner walls than the outer beams and the wall thickness also decreases in going from top to bottom in the nanolattice. These variations in wall thickness are due to the line-of-sight nature of sputter deposition discussed in sections 4.2.2 and 4.3.1. From these images, it also appears that the internal nanolattice beams exhibited some distortion and contraction upon irradiation. The high energy 12 MeV Ni^{2+} ion irradiation may have caused a redistribution of material within the nanolattice whereby beams on the outside surfaces (visible in Figure 42) gained material and those internal beams (visible in Figure 43) lost material. Images from the cross-sectional cuts, such as those shown in Figure 43 (g-l), illustrate that the thinner beams which are towards the bottom and inside of the nanolattices were most affected structurally by irradiation and contracted slightly while the thicker beams on the outside and top of the nanolattice were able to resist changes in irradiation, preventing the overall nanolattice structure from undergoing the significant contraction observed in the thinner-walled nanolattices pictured in Figure 41.

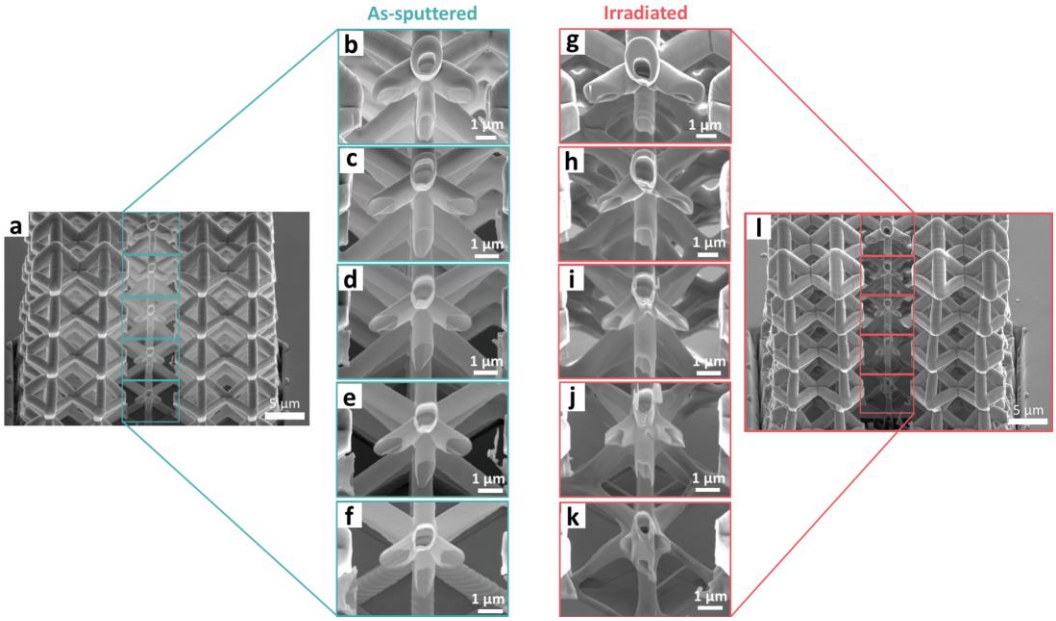

Figure 43. Cross-sectional SEM images obtained from the most interior column of unit cells in the nanolattice structures. The images were obtained with the SEM stage at a ~52° tilt. (a) As-fabricated nanolattice whose individual unit cells are shown in the higher magnification images in (b-f) arranged in top-down order, with (b) the topmost unit cell and (f) the bottommost unit cell, closest to the substrate. (l) Irradiated nanolattice whose individual unit cells are shown in the higher magnification images in (g-k) arranged in top-down order, with (g) the topmost unit cell and (k) the bottommost unit cell, closest to the substrate. The original median wall thickness of the as-fabricated nanolattices and the irradiated nanolattices prior to irradiation was ~88 nm.

The wall thickness measurements obtained from the six cross-sectional cuts performed on each nanolattice led to the measured wall thickness distributions shown in Figure 44. Despite the apparent structural changes in the nanolattices upon irradiation, the distributions of wall thickness for the as-fabricated and irradiated nanolattices are quite similar. Table 3 displays the resultant median and average wall thicknesses, which move in opposite directions upon irradiation: the median wall thickness decreases from 88 nm to 85 nm upon irradiation, while the average wall thickness increases from 114 nm to 117 nm upon irradiation. This is consistent with the qualitative observations of the nanolattice images in Figure 42 and Figure 43, involving the thinner interior nanolattice beams appearing to lose material and the thicker outer nanolattice beams appearing to gain material in a "rich get richer, poor get poorer" effect. Prior to irradiation, the thick outer nanolattice beams skew the average wall thickness high,

and upon irradiation the increase in wall thickness of these already thick beams further increases the resultant average wall thickness. The thinner interior nanolattice beams making up a majority of the nanolattice largely influence the median wall thickness, and upon irradiation the decrease in wall thickness of these thinner beams decreases the resultant median wall thickness. This thickening of thick walls and thinning of thin walls is also consistent with increase in the standard deviation of the wall thickness measurements from 101 nm to 120 nm upon irradiation, as shown in Table 3.

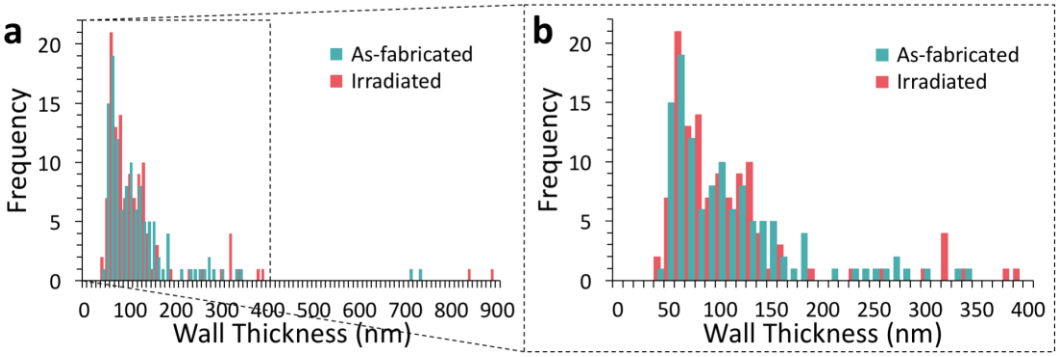

Figure 44. Histogram of wall thickness measurements for as-fabricated and irradiated nanolattices. (a) Histogram displayed over the entire range of wall thicknesses measured from 0-900 nm. (b) Histogram zoomed in to the wall thickness range of 0-400 nm to make the distribution at small wall thicknesses more visible.

Table 3. Measured wall thickness of as-fabricated and irradiated nanolattices. Measurements of wall thickness were conducted from SEM images of different FIB-created cross-sections, ranging from the edge to the center of the nanolattices. ~120 wall thickness measurements from representative regions in each nanolattice were used to determine each median, average, and standard deviation.

Nanolattice type	Measured Wall Thickness		
	Median	**Average**	**Standard deviation**
As-fabricated	88 nm	114 nm	101 nm
Irradiated	85 nm	117 nm	120 nm

As observed in Figure 43, it is not necessarily the wall thickness of the nanolattice beams that appears to change upon irradiation but the overall beam dimensions. Consequently, the inner beam dimensions were also measured, with the results displayed in Table 4. As the beams were not perfectly circular, both the vertical (major) beam axis and the horizontal (minor) beam axis were measured. The slightly elliptical shape of the beams became more pronounced upon irradiation as the vertical (major) beam axis increased from 803 nm to 867 nm and the horizontal (minor) beam axis decreased from 751 nm to 713 nm. Consistent with the general distortion and shape changes upon irradiation, as observed in Figure 43, the standard deviation in the measured beam dimensions increases by roughly a factor of two upon irradiation; the standard deviation in the vertical beam axes increase from 66.6 nm to 125 nm upon irradiation, and the standard deviation in the horizontal beam axes increase from 42.7 nm to 95.3 nm upon irradiation. However, the simultaneous increase in the vertical beam axis with the decrease in the horizontal beam axis led to only a small net change in the average beam axis, increasing by only 1.7% from 777 nm in the as-fabricated nanolattices to 790 in the irradiated nanolattices.

Table 4. Measured inner beam dimensions of as-fabricated and irradiated nanolattices. The beams are slightly elliptical in shape, hence both the vertical (major) axis and the horizontal (minor) axis of each beam were measured. Measurements were conducted from SEM images of different FIB-created cross-sections ranging from the edge to the center of the nanolattices. 30 beam measurements were used to determine the average and standard deviation for the vertical and horizontal beam axes. 60 beam measurements were used to determine the average and standard deviation for overall inner beam dimension.

Nanolattice type	**Vertical beam axis**		**Horizontal beam axis**		**Overall**	
	Average	**Standard deviation**	**Average**	**Standard deviation**	**Average**	**Standard deviation**
As-fabricated	803 nm	66.6 nm	751 nm	42.7 nm	777 nm	61.3 nm
Irradiated	867 nm	125 nm	713 nm	95.3 nm	790 nm	135 nm

5.3.2. Microstructural characterization

Figure 45 (a) displays XRD data obtained on the as-fabricated, irradiated, and annealed specimens. The XRD scans from the as-fabricated and irradiated samples have the broad characteristic amorphous hump present over the 2θ range of ~28-43 degrees and exhibit no sharp peaks, apart from those characteristic of the (100) Si substrate. In addition, the as-fabricated and irradiated XRD scans are nearly identical, demonstrating no major change in microstructure upon irradiation. For comparison, the scan from the sample annealed at $1.1T_g$ exhibits significant changes: the characteristic amorphous hump disappears, and several new sharper peaks appear, indicating the onset of crystallization. The lack of such peaks in either the as-fabricated or irradiated scans supports the notion that these samples are amorphous.

Figure 45 (b, c) shows TEM performed on the beam wall of an irradiated nanolattice. For comparison, TEM on the as-fabricated nanolattice was shown in Figure 31. The diffuse rings in the diffraction pattern of Figure 45 (b) are characteristic of an amorphous material. The dark field image in Figure 45 (c) shows no crystallites and the largest size of anything resembling a nanocrystalline grain is only ~0.8 nm. As such, irradiation did not cause crystallization of the metallic glass. There may be some small changes in the short- and medium-range atomic order of the metallic glass upon irradiation but such changes are not detectable by TEM or benchtop XRD.

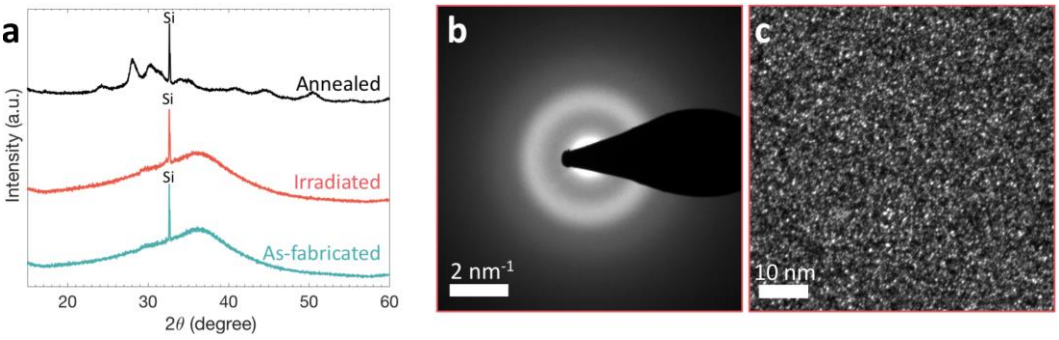

Figure 45. Microstructural characterization of as-fabricated and irradiated nanolattices. (a) XRD scans from as-sputtered, irradiated, and annealed samples. (b) TEM diffraction pattern and (c) dark-field TEM image obtained from the beam wall of an irradiated nanolattice.

5.3.3. Compression experiments on as-fabricated and irradiated nanolattices

Figure 46 contains engineering stress versus strain data obtained via uniaxial compression of individual nanolattices to various strains. In Figure 46 (a), the data is displayed over the whole range of strains tested, with dotted lines connecting each data point. The presence of long stretches of dotted line with no data points indicates a failure event, i.e. a strain burst, that occurred too rapidly for data acquisition. The data capture rate was 100 Hz, indicating the large first strain bursts, involving ~30-40% increases in strain with 0-1 data points captured, took place in only ~0.01 seconds. Strain bursts, these rapid increases in strain indicative of sudden failure events, are present in the stress-strain response of both as-fabricated and irradiated nanolattices. However, the stress-strain data of the irradiated nanolattices contain noticeably smaller strain bursts, signifying less catastrophic failure events and increased deformability compared to the as-fabricated nanolattices. Representative videos of as-fabricated (Video 14) and irradiated (Video 15) nanolattices during compression are included in the supplementary files.

Figure 46 (b) displays the same stress-strain data shown in Figure 46 (a), but zoomed into the low strain region of 0-0.07 strain so that the stress-strain response before the first strain burst is more visible. In Figure 46 (b), only the data points are plotted, no connecting dotted lines are drawn between data points. The irradiated nanolattices are able to accommodate much larger strains before any strain burst occurs, as demonstrated by the presence of continuous data in Figure 46 (b) to larger strains for the irradiated nanolattices. As can be observed in Figure 46 (b), the irradiated nanolattices reach strains of ~6% before the first strain burst while the as-fabricated nanolattice only reach strains ~2% before the first strain burst. This low strain region was also used for determination of the elastic modulus (E) and yield strength (σ_y), which are plotted in Figure 46 (c, d). Irradiation resulted in little change to the elastic modulus, which was measured as 245 ± 32.1 MPa for the as-fabricated nanolattices

and 261 ± 51.3 MPa for the irradiated nanolattices. The yield strength increases by 35.7% upon irradiation from 3.69 ± 0.247 MPa in the as-fabricated nanolattices to 5.01 ± 0.299 MPa in the irradiated nanolattices.

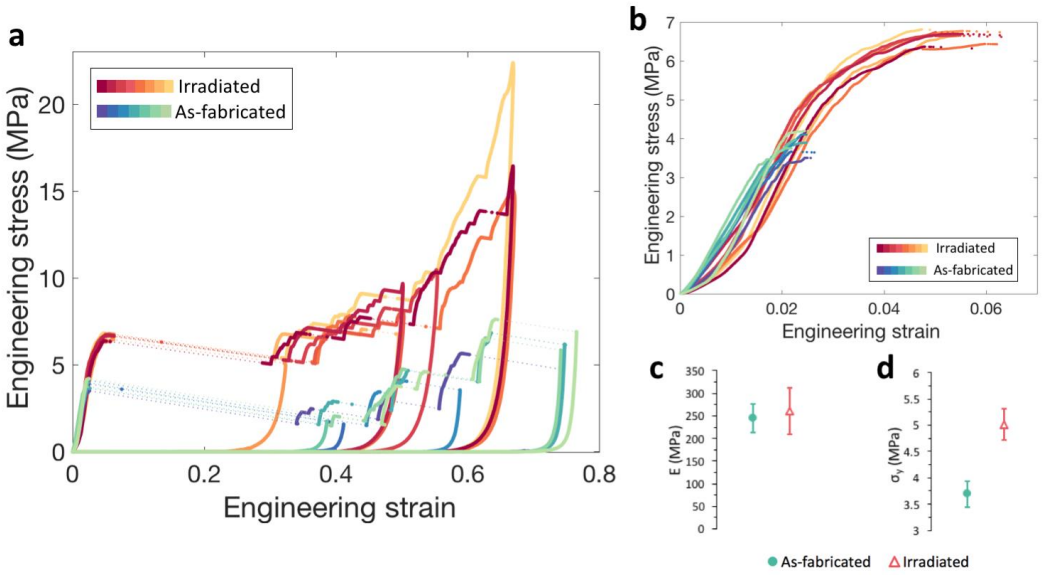

Figure 46. Engineering stress-strain data obtained via uniaxial compression on as-fabricated and irradiated nanolattices. (a) Stress-strain data displayed for the whole range of strain tested, utilizing dotted lines to connect data points. (b) Stress-strain data displayed from 0-0.07 strain in the region just before the first strain burst. Only data points are shown with no dotted line connections. Average (c) elastic modulus and (d) yield strength for as-fabricated and irradiated nanolattices with error bar denoting ± one standard deviation in the measured property.

Compared to tension experiments, compression experiments often do not result in a clear failure event; however, the size and nature of the first strain burst observed after elastic loading in the compression experiment of this chapter can be thought of as analogous to the fracture of a tensile sample. Figure 47 (a) displays a direct comparison between the representative stress-strain response of an as-fabricated nanolattice and an irradiated nanolattice as a result of compression to the first strain burst. The size of the first strain burst and the size of the stress decrease as a result of the strain burst (stress drop) can be used as measures of the severity (or catastrophic-nature) of the first strain burst. The average size of this first strain burst and the corresponding stress-drop were both found to decrease upon irradiation as

shown in Figure 47 (b, c). The size of the first strain burst in the as-fabricated nanolattices was measured as 0.377 ± 0.039 and decreased upon irradiation to 0.293 ± 0.037. Likewise, the size of the corresponding stress drop in as-fabricated nanolattices was measured as 2.28 ± 0.23 MPa and decreased upon irradiation to 1.54 ± 0.20 MPa. The decrease in the size of the first strain burst and stress drop upon irradiation demonstrates that compared to the as-fabricated nanolattices, the irradiated nanolattices exhibit less catastrophic first failure events. As discussed in section 4.3.2, the absolute size of the strain burst and stress drop will depend on the details of compression test method and controls as well as the dynamics of the mechanical testing instrument used. As all nanolattices in this chapter were compressed utilizing an identical test method and testing instrument, a direct comparison can be made for the sizes of the strain bursts and stress drops between the as-fabricated and irradiated nanolattices. However, the size of these strain bursts and stress drops may vary with a different mechanical testing instrument and test method; hence care should be taken in comparing the strain burst and stress drop size in this study with those in another study using disparate testing conditions or instrumentation.

SEM images following compression to the first strain burst and unloading for a representative as-fabricated nanolattice (Figure 47 (d-f)) and a representative irradiated nanolattice (Figure 47 (g-i)) reveal a significant difference in the morphology of the failed layers. The as-fabricated nanolattice exhibits complete failure of the two middle layers with the unit cells of the failed layers destroyed beyond recognition. The irradiated nanolattice exhibits deformation akin in appearance to the layer-by-layer collapse observed in the deformable thinner walled nanolattices discussed in Chapter 4 and illustrated in Figure 34.

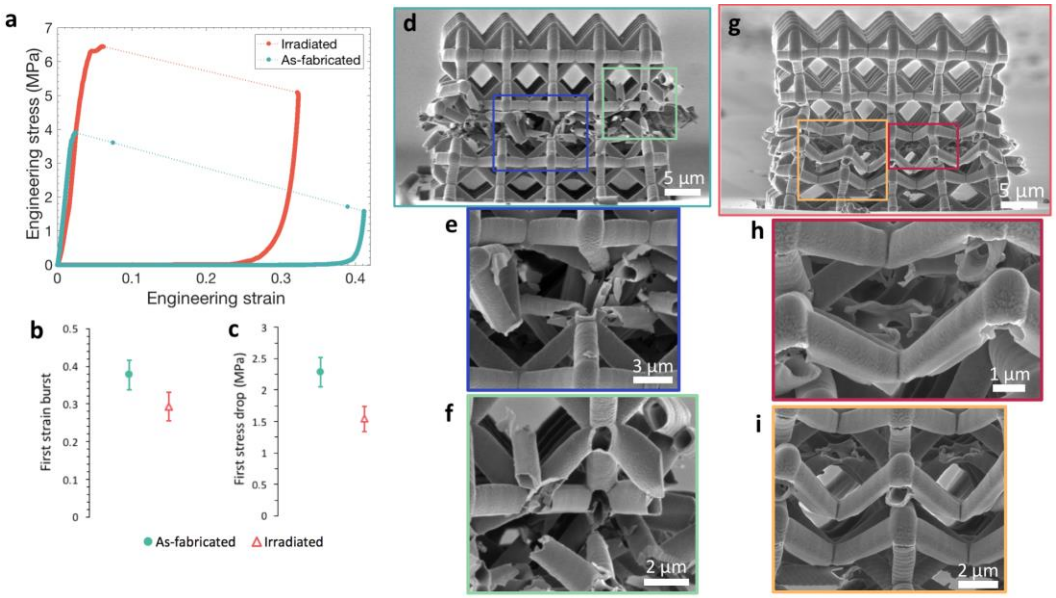

Figure 47. First strain burst comparison between representative as-fabricated and irradiated nanolattices. (a) Representative stress-strain responses of as-fabricated and irradiated nanolattices obtained from compression to the first strain burst and unloading. Quantification of the first strain burst by measurement of (b) the average size of the first strain burst and (c) the average size of the stress drop upon the first strain burst, with error bars denoting ± one standard deviation in the measurement. Post-mortem SEM images of (d-f) as-fabricated and (g-i) irradiated nanolattices whose stress-strain data are shown in (a).

5.4. Discussion

5.4.1. Atomic-level changes in metallic glass from irradiation

Changes in metallic glasses' mechanical response, particularly deformability, upon exposure to irradiation are generally explained in terms of local atomic structural changes brought about by the ion irradiation, as discussed in [23-26,44,154,185]. In the case of the current study, the incoming high energy Ni^{2+} ions bombard the metallic glass nanolattice, moving the constituent metallic glass atoms into a higher potential energy state. This higher potential energy state brought about by irradiation has been equivalently referred to in literature as more disordered [25], containing less icosahedral [24,186] or short-range [187,188] order, more unrelaxed or farther from relaxation [44], in a more liquid-like state [23], and containing more free volume [154,189-192]. Local atomic structural changes in the metallic

glass upon irradiation decrease the energetic cost of moving atoms and brings about more atomic mobility. The increased atomic mobility upon irradiation allows the atoms to more readily participate in shear transformation zones, with the effect that many smaller shear bands form simultaneously, intersect each other, and result in a globally ductile-like response. In contrast, metallic glasses containing low atomic mobility usually fail by a single catastrophic shear band event.

The irradiation conditions were chosen to minimize the presence of additional Ni in the nanolattices as a result of the ion irradiation. The utilization of a low fluence (6×10^{14} ions cm^{-2}) resulted in a small amount of total Ni^{2+} ions present, and the utilization of high energy (12 MeV) resulted in most ions passing completely through the nanolattices. This minimized additional Ni concentration resulting from the irradiation and the corresponding complicating effects of such additional Ni. As discussed in section 5.2.2, SRIM calculations estimate the maximum additional concentration of Ni from the irradiation as only 1.1×10^{-4} at. %. While the collision cascades set off by the incoming Ni ions likely had a significant influence on the metallic glass material, the concentration of additional Ni from the irradiation is so small that the presence of this additional Ni is not expected to have an influence on the mechanical response.

5.4.2. Nanolattice structural effects and changes upon irradiation

The arrangement of the metallic glass in nanolattice structures necessitates the consideration of potential structural failure mechanisms. Following the work of Meza et. al [161], failure of the nanolattice structure will result from the combinations of three potential mechanisms: yielding, local shell buckling, and Euler beam buckling. As derived in section 4.4.1, equating the stresses necessary to initiate each individual failure mechanism, the

following expressions were obtained for the critical transition point between structural buckling and yielding:

$$\left(\frac{t}{r}\right)_{crit} = \frac{\sigma_y}{E}\sqrt{3(1-\nu^2)} \tag{35}$$

$$\left(\frac{r}{L}\right)_{crit} = \frac{3}{5\pi}\sqrt{\frac{2\sigma_y}{E}} \tag{36}$$

where equation (35) is the critical transition point between yielding and shell buckling and equation (36) is the critical transition point between yielding and Euler (beam) buckling. Equations (35) and (36) depend on only the constituent metallic glass bulk material properties: yield strength (σ_y), elastic modulus (E), and Poisson's ratio (ν), which were taken as 1.26 GPa, 130 GPa, and 0.36 respectively, as discussed in section 4.4.1. Substituting these values into equations (35) and (36), the critical local shell buckling transition is found to occur at $(t/r)_{crit}$ = 0.016 and the critical Euler beam buckling transition is found to occur at $(r/L)_{crit}$ = 0.027. Considering only these structural effects, nanolattice structures with geometrical values of wall thickness (t), beam radius (r), and beam length (L) such that (t/r) and (r/L) are greater than these critical ratios would be expected to fail by yielding with no structural buckling.

As this work focused on the compression and characterization of the thickest-walled nanolattices, the calculation of (t/r) and (r/L) will depend on the t, r, and L from these thickest-walled nanolattices. The wall thickness (t) is given in Table 3, the beam radius (r) is given in Table 4, and beam length (L) is unchanged by irradiation at 4.9 μm. Considering local shell buckling, the as-fabricated nanolattices exhibit,

$$\left(\frac{t}{r}\right)_{as-fab} = \left(\frac{88\ nm}{388\ nm}\right) = 0.23 \tag{37}$$

and the irradiated nanolattices exhibit

$$\left(\frac{t}{r}\right)_{irr} = \left(\frac{85\ nm}{395\ nm}\right) = 0.21 \tag{38}$$

The (t/r) ratios in equations (37) and (38) are both over an order of magnitude greater than the critical ratio for shell-buckling of $(t/r)_{crit} = 0.016$, therefore no nanolattices in this work would be expected to exhibit local (shell) buckling. Considering Euler beam buckling, the as-fabricated nanolattices exhibit,

$$\left(\frac{r}{L}\right)_{as-fab} = \left(\frac{388\ nm}{4900\ nm}\right) = 0.079 \tag{39}$$

and the irradiated nanolattices exhibit,

$$\left(\frac{r}{L}\right)_{irr} = \left(\frac{395\ nm}{4900\ nm}\right) = 0.081 \tag{40}$$

The (r/L) ratios in equations (39) and (40) are significantly larger than the critical value for Euler beam buckling of $(r/L)_{crit} = 0.027$, thus no nanolattices in this work would be expected to exhibit Euler beam buckling. These calculations reveal that the structure of both the as-fabricated and irradiated nanolattices is outside of the regime where local shell buckling or Euler beam buckling are expected, and hence yielding is the dominant failure mechanism. Further, the similarity between as-fabricated and irradiated nanolattices in (t/r) ratios noted in equations (37) and (38) and (r/L) ratios noted in equations (39) and (40) demonstrates that the small changes in measured wall thickness and beam radius upon irradiation do not change the expected failure mechanisms of the nanolattice structure.

The presence of contraction in the structure of the nanolattices upon irradiation renders any changes in mechanical response a convolution of the atomic-level changes in the constituent metallic glass with these structural changes in the nanolattices. The thinner-walled nanolattices, pictured in Figure 41, underwent such significant contraction upon irradiation that we chose not to conduct compression experiments on those nanolattices, as the mechanical response would likely be dominated by the contraction of the structure. Compression experiments were only performed on the thickest-walled nanolattices, pictured in Figure 42 and Figure 43, which exhibited the smallest structural change upon irradiation.

Although the overall structure of these thicker-walled nanolattices does exhibit some contraction upon irradiation, as visualized in Figure 42 (bottom), the wall thickness and inner beam dimensions are largely unchanged upon irradiation.

In terms of the inner beam dimensions, the average inner beam axis measurement only increases by 1.7% upon irradiation. The apparent collapse of nanolattice beams upon irradiation is more pronounced for the thinner-walled interior beams as visualized in Figure 43. The slightly elliptical shape of the beams became more elliptical upon irradiation as evidenced by the increase in the measured beam major axis and decrease in the measured beam minor axis, as shown in Table 4. Further, the ~two-fold increase in standard deviation of these measured beam dimensions demonstrates a larger variation in inner beam dimensions upon irradiation, consistent with these shape changes.

As observed in Chapter 4, the nanolattice wall thickness plays a key role in determining mechanical response with thicker-walled nanolattices exhibiting higher strength and more catastrophic failure. Obtaining measures of any wall thickness changes upon irradiation is vital to understand the origin of the resultant nanolattice mechanical response. As shown in Table 3, the median and average wall thicknesses are largely unchanged upon irradiation, with the median wall thickness decreasing from 88 nm to 85 nm upon irradiation and the average wall thickness increasing from 114 nm to 117 nm upon irradiation. The simultaneous decrease of the median wall thickness and increase of the average wall thickness results in no significant change to the overall relative density of the nanolattice. However, the relative density may exhibit some local changes with the originally thinner-walled beams, which lost material upon irradiation, also losing some relative density upon irradiation and the originally thicker-walled beams, which gained material upon irradiation, also gaining some relative density upon irradiation. These local changes in relative density are slight as the median and average wall thickness each change by less than 5 nm upon irradiation.

The larger change in relative density likely comes from the minor collapse of the nanolattices upon irradiation, which led to a 13.6% decrease in the height of the irradiated nanolattices. This collapse of the nanolattices upon irradiation also caused the top surface of the irradiated nanolattices to become slightly curved, with the center of the nanolattice marginally taller than the outer edges, as can be observed in Figure 42 (bottom right). This structural change reduces the measured elastic modulus of the irradiated nanolattices because the flat punch tip must first compress the taller central unit cells before full contact can be made with the shorter unit cells on the edges of the nanolattice. Therefore, the measured elastic modulus of the irradiated nanolattices is likely artificially lower than it would have been had the top surface of the irradiated nanolattices been perfectly flat.

5.4.3. Increased strength with improved deformability

Improved ductility or deformability usually come with a significant sacrifice in strength. For example, as observed in Chapter 3, while ductility could be improved in metallic glass nanopillars by processing them in an as-sputtered as opposed to annealed state, the more ductile pillars exhibited a 16% decrease in yield strength, as shown in Figure 20 (c). This lower yield strength in the more ductile pillars is thought to occur because sputtering results in a metallic glass with excess free volume and a corresponding lower density, as discussed in Chapter 3. Likewise, the decrease in wall thickness of the nanolattices in Chapter 4 led to a more deformable response; however the thinnest-walled nanolattices also exhibited a two order of magnitude loss in strength compared to the thickest-walled nanolattices, as shown in Figure 39 (b). With these results in mind, the observation that irradiated nanolattices exhibit improved deformability with a simultaneous 35.7% increase in yield strength is quite remarkable and surprising. The simultaneous increase in strength and deformability upon irradiation suggests that the observed enhancement in deformability from irradiation cannot

be attributed to a potential structural effect of decreased wall thickness as decreased wall thickness would lead to a loss of strength, as demonstrated in Chapter 4; see for example Figure 39 (b).

Structural changes in the nanolattices upon irradiation may be at least partially responsible for the increased strength. The observed contraction of the nanolattices upon irradiation led to a 13.6% reduction in height with negligible changes in measured wall thickness and overall beam dimension. Assuming the total amount of material in the nanolattice is unchanged upon irradiation, which is consistent with the negligible changes in measured wall thickness and beam dimensions, a 13.6% decrease in height corresponds to a 15.5% increase in relative density. A denser nanolattice would be expected to exhibit higher strength. For the bending-dominated octahedron-based structure used in this study, the expected scaling of yield strength with relative density is $\sigma_y \propto \bar{\rho}^{1.5}$ as shown in equation (24). Using this relation, the 15.5% increase in relative density corresponds to an expected increase in yield strength of 24.1%. Hence, a large portion of the observed 35.7% increase in yield strength can be attributed to the decrease in height upon irradiation causing a densification of the nanolattice structure. There is still a significant portion of the increase in yield strength that cannot be attributed to this structural effect.

Previous investigations of the influence of irradiation on metallic glass strength have had mixed results. Irradiation of metallic glasses has been reported to lead to an increase [193-197], negligible change [23,24,154], and decrease [26,44,185,187,188,198,199] in the strength or hardness of metallic glasses. Observed increases in strength or hardness of irradiated metallic glasses sometimes occur because of the formation of precipitates and crystalline phases within the amorphous matrix upon irradiation [193-196]. The XRD and TEM results shown in Figure 45 indicate that the amorphous structure of the nanolattices was maintained upon irradiation with no evidence of crystallization. Therefore, the increased strength and deformability upon

irradiation in this work cannot be attributed to the presence of nanocrystallites. In the nanolattice system of this chapter, the confluence of irradiation-induced changes in the larger nanolattice structure with the local atomic structural changes within the constituent metallic glass unfortunately makes it difficult to fully ascertain the reason for the observed strengthening upon irradiation.

5.5. Summary and Outlook

Irradiating metallic glass nanolattices led to improved deformability and decreased the catastrophic nature of failure while also increasing yield strength by 35.7%. The enhanced deformability in irradiated metallic glass nanolattices can be attributed to irradiation bringing the constituent metallic glass into a more disordered, higher potential energy state with greater atomic mobility. The observed increase in yield strength can be at least partially attributed to the densification that occurs in the metallic glass nanolattices as the structure contracts slightly upon irradiation, reducing in height by 13.6%. The simultaneous improvement in deformability and strength suggests irradiation as a promising knob to use to enhance the mechanical properties of metallic glass nanolattices.

The slight contraction observed in the ~88 nm wall thickness nanolattices upon irradiation and the significant contraction observed in the thinner walled nanolattices (Figure 41) upon irradiation highlights the importance of considering the particular combination of nanolattice structure and irradiation conditions. These low relative density nanolattices may exhibit enhanced deformability under certain irradiation conditions (as in the thickest-walled nanolattices) but complete destruction of the nanolattice structure under other irradiation conditions (as seen with the thinner-walled nanolattices). A previous study on irradiation of nanoporous Au [180], which possessed characteristic feature sizes in the same range as the nanolattice wall thicknesses of this work, found a particular window in the parameter space of

ligament diameter, temperature, ion energy, and dose rate where the nanoporous Au exhibited radiation-damage tolerance. However, outside of that window, where irradiation conditions were too intense and ligaments were too small, ligaments experienced melting, breaking, and compaction with increasing dose [180]. Although the mechanism of radiation damage in metallic glasses is different than that of crystalline metals, the same concern for the structural stability of ligaments in nanoporous metals applies to the structural stability of hollow metallic glass beams in nanolattices. Care must be taken in utilizing such low density materials, like nanolattices, for radiation-intensive applications as the nanoscale thickness of the beam wall is likely more sensitive to structural damage from irradiation than denser bulk materials.

Chapter 6. Summary and Outlook

All metallic glasses are amorphous with no long-range atomic order. This amorphous state presents a challenge in the precise understanding and quantification of atomic arrangement. However, this challenge does not mean the amorphous atomic structure of different metallic glasses can be thought of as equivalent. The presence of differences in short- and medium-range order among different metallic glasses leads to substantial changes in the resultant mechanical behavior and deformability.

These changes in short- and medium-range order can be brought about by changes in processing conditions, for example fabrication method or exposure to irradiation. In Chapter 2, we observed that He^+ implantation of metallic glass nanopillars led to a two-fold increase in plastic strain with no sacrifice in strength. Those experiments demonstrated that enhanced deformability can be brought about by irradiation, which is thought to bring the metallic glass into a more disordered state with greater atomic mobility. Similarly, reducing the sample size of the metallic glass to the nanoscale can similarly enhance deformability, partially due to the decrease in short- and medium- range order among metallic glass atoms close to free surfaces. In Chapter 3, this "smaller is more ductile" size effect was demonstrated in Zr-Ni-Al metallic glass nanopillars, which exhibited substantial necking for certain nanopillar sizes. Importantly, it was not only the sample size that influenced the necking behavior but also the processing conditions. Samples in an as-sputtered state exhibited substantially more ductility than those in an annealed state; and synchrotron XRD revealed a significant increase in short- and medium-range order upon annealing, thereby linking the state of atomic order in a metallic glass with its ductility.

The work in Chapter 4 and Chapter 5 built upon the fundamental nanopillar studies of the earlier chapters to proliferate some of the effects observed in metallic glass nanopillars to larger metallic glass nanolattices. Chapter 4 demonstrated that the "smaller is more

deformable" size effect, first observed in metallic glass nanopillars, also occurs in larger metallic glass nanolattices so long as the wall thickness of the nanolattice beams is kept below a critical size. In Chapter 5, irradiation of metallic glass nanolattices led to a further enhancement of deformability and a 35.7% increase in yield strength. The enhanced deformability in irradiated nanolattices can be attributed to the same reason for enhanced deformability in irradiated metallic glass nanopillars, namely that irradiation brings the metallic glass into a more disordered state with less short- and medium-range order. This more disordered state has more atomic mobility, allowing the atoms to more easily deform without catastrophic failure.

Perhaps unsurprisingly, the key to controlling deformability in metallic glasses is controlling details of the short- and medium-range order in their underlying amorphous atomic structure. The work in this thesis demonstrates that sample size reduction, fabrication by sputter deposition, and exposure to irradiation can all be used to enhance deformability. The "smaller is more deformable" sample size effect has also been shown to occur in larger nanolattices, which also similarly exhibit irradiation-mediated enhancement in deformability. This work points the way towards carefully designing metallic glasses with particular fabrication conditions, characteristic feature size, nano-architecture, processing conditions, and irradiation exposure to achieve a certain atomic-level structure and concomitant mechanical response meeting some desirable criteria of deformability.

References

[1] W. Klement, R.H. Willens, and P.O.L. Duwez, Non-crystalline structure in solidified gold--silicon alloys, Nature. 187 (1960) 869-870.

[2] M.F. Ashby, and A.L. Greer, Metallic glasses as structural materials, Scripta Materialia. 54 (2006) 321-326.

[3] M. Telford, The case for bulk metallic glass, Materials Today. 7 (2004) 36-43.

[4] W.H. Wang, C. Dong, and C.H. Shek, Bulk metallic glasses, Materials Science and Engineering R. 44 (2004) 45-89.

[5] W.L. Johnson, Bulk glass-forming metallic alloys: Science and technology, MRS Bulletin. 24 (1999) 42-56.

[6] C. Smith, A Liquidmetal iPhone might soon become a reality, BGR. (n.d.).

[7] M. Chen, A brief overview of bulk metallic glasses, NPG Asia Materials. 3 (2011) 82-90.

[8] J. Schroers, T.M. Hodges, G. Kumar, H. Raman, A.J. Barnes, Q. Pham, and T.A. Waniuk, Thermoplastic blow molding of metals, Materials Today. 14 (2011) 14-19.

[9] J. Schroers, G. Kumar, T.M. Hodges, S. Chan, and T.R. Kyriakides, Bulk metallic glasses for biomedical applications, JOM. 61 (2009) 21-29.

[10] P. Sharma, N. Kaushik, H. Kimura, Y. Saotome, and A. Inoue, Nano-fabrication with metallic glass-an exotic material for nano-electromechanical systems, Nanotechnology. 18 (2007) 035302.

[11] G. Kumar, H.X. Tang, and J. Schroers, Nanomoulding with amorphous metals, Nature. 457 (2009) 868-72.

[12] G. Doubek, R.C. Sekol, J. Li, W.-H. Ryu, F.S. Gittleson, S. Nejati, E. Moy, C. Reid, M. Carmo, M. Linardi, P. Bordeenithikasem, E. Kinser, Y. Liu, X. Tong, C.O. Osuji, J. Schroers, S. Mukherjee, and A.D. Taylor, Guided Evolution of Bulk Metallic Glass Nanostructures: A Platform for Designing 3D Electrocatalytic Surfaces, Advanced Materials. (2015).

[13] R.C. Sekol, G. Kumar, M. Carmo, F. Gittleson, N. Hardesty-Dyck, S. Mukherjee, J. Schroers, and A.D. Taylor, Bulk metallic glass micro fuel cell, Small. 9 (2013) 2081-5, 2026.

[14] C.A. Schuh, T.C. Hufnagel, and U. Ramamurty, Mechanical behavior of amorphous alloys, Acta Materialia. 55 (2007) 4067-4109.

[15] F.F. Wu, W. Zheng, J.W. Deng, D.D. Qu, and J. Shen, Super-high compressive plastic deformation behaviors of Zr-based metallic glass at room temperature, Materials Science and Engineering A. 541 (2012) 199-203.

[16] J. Das, M.B. Tang, K.B. Kim, R. Theissmann, F. Baier, W.H. Wang, and J. Eckert, Work-hardenable ductile bulk metallic glass, Physical Review Letters. 94 (2005) 205501.

[17] J. Schroers, and W.L. Johnson, Ductile bulk metallic glass, Physical Review Letters. 93 (2004) 255506.

[18] K.F. Yao, F. Ruan, Y.Q. Yang, and N. Chen, Superductile bulk metallic glass, Applied Physics Letters. 88 (2006) 122106.

[19] Y.H. Liu, G. Wang, R.J. Wang, D.Q. Zhao, M.X. Pan, and W.H. Wang, Super plastic bulk metallic glasses at room temperature, Science. 315 (2007) 1385-8.

[20] C.A. Schuh, and A.C. Lund, Atomistic basis for the plastic yield criterion of metallic glass, Nature Materials. 2 (2003) 449-52.

[21] Q.S. Zhang, W. Zhang, G.Q. Xie, D.V. Louzguine-Luzgin, and A. Inoue, Stable flowing of localized shear bands in soft bulk metallic glasses, Acta Materialia. 58 (2010) 904-909.

[22] T. Mukai, T.G. Nieh, Y. Kawamura, A. Inoue, and K. Higashi, Dynamic response of a $Pd_{40}Ni_{40}P_{20}$ bulk metallic glass in tension, Scripta Materialia. 46 (2002) 43-47.

[23] D.J. Magagnosc, R. Ehrbar, G. Kumar, M.R. He, J. Schroers, and D.S. Gianola, Tunable tensile ductility in metallic glasses, Scientific Reports. 3 (2013) 1096.

[24] D.Z. Chen, D. Jang, K.M. Guan, Q. An, W.A. Goddard, and J.R. Greer, Nanometallic glasses: size reduction brings ductility, surface state drives its extent, Nano Letters. 13 (2013) 4462-8.

[25] Q. Xiao, L. Huang, and Y. Shi, Suppression of shear banding in amorphous ZrCuAl nanopillars by irradiation, Journal of Applied Physics. 113 (2013) 083514-083514.

[26] R. Raghavan, K. Boopathy, R. Ghisleni, M.A. Pouchon, U. Ramamurty, and J. Michler, Ion irradiation enhances the mechanical performance of metallic glasses, Scripta Materialia. 62 (2010) 462-465.

[27] D.R. Harries, Neutron Irradiation Embrittlement of Austenitic Stainless Steels and Nickel-Base Alloys, Journal of the British Nuclear Energy Society. 5 (1966).

[28] J. Henry, L. Vincent, X. Averty, B. Marini, and P. Jung, Effect of a high helium content on the flow and fracture properties of a 9Cr martensitic steel, Journal of Nuclear Materials. 367 (2007) 411-416.

[29] H. Trinkaus, and B.N. Singh, Helium accumulation in metals during irradiation--where do we stand?, Journal of Nuclear Materials. 323 (2003) 229-242.

[30] B.N. Singh, and S.J. Zinkle, Defect accumulation in pure fcc metals in the transient regime: a review, Journal of Nuclear Materials. 206 (1993) 212-229.

[31] P. Jung, and H. Ullmaier, Effects of light-ion irradiation on mechanical properties of metals and alloys, Journal of Nuclear Materials. 174 (1990) 253-263.

[32] M. Victoria, N. Baluc, C. Bailat, Y. Dai, M.I. Luppo, R. Schaublin, and B.N. Singh, The microstructure and associated tensile properties of irradiated fcc and bcc metals, Journal of Nuclear Materials. 276 (2000) 114-122.

[33] L.K. Mansur, Theory of transitions in dose dependence of radiation effects in structural alloys, Journal of Nuclear Materials. 206 (1993) 306-323.

[34] G.R. Odette, and G.E. Lucas, Embrittlement of nuclear reactor pressure vessels, JOM. 53 (2001) 18-22.

[35] R.D. Conner, W.L. Johnson, N.E. Paton, and W.D. Nix, Shear bands and cracking of metallic glass plates in bending, Journal of Applied Physics. 94 (2003) 904-911.

[36] C.Q. Chen, Y.T. Pei, and J.T.M. De Hosson, Effects of size on the mechanical response of metallic glasses investigated through in situ TEM bending and compression experiments, Acta Materialia. 58 (2010) 189-200.

[37] D. Jang, C.T. Gross, and J.R. Greer, Effects of size on the strength and deformation mechanism in Zr-based metallic glasses, International Journal of Plasticity. 27 (2011) 858-867.

[38] C.A. Volkert, A. Donohue, and F. Spaepen, Effect of sample size on deformation in amorphous metals, Journal of Applied Physics. 103 (2008) 083539-083539.

[39] O.V. Kuzmin, Y.T. Pei, C.Q. Chen, and J.T.M. De Hosson, Intrinsic and extrinsic size effects in the deformation of metallic glass nanopillars, Acta Materialia. 60 (2012) 889-898.

[40] D. Jang, and J.R. Greer, Transition from a strong-yet-brittle to a stronger-and-ductile state by size reduction of metallic glasses, Nature Materials. 9 (2010) 215-219.

[41] H. Guo, P.F. Yan, Y.B. Wang, J. Tan, Z.F. Zhang, M.L. Sui, and E. Ma, Tensile ductility and necking of metallic glass, Nature Materials. 6 (2007) 735-9.

[42] L. Tian, Z.-W. Shan, and E. Ma, Ductile necking behavior of nanoscale metallic glasses under uniaxial tension at room temperature, Acta Materialia. 61 (2013) 4823-4830.

[43] J.H. Luo, F.F. Wu, J.Y. Huang, J.Q. Wang, and S.X. Mao, Superelongation and atomic chain formation in nanosized metallic glass, Physical Review Letters. 104 (2010) 215503.

[44] D.J. Magagnosc, G. Kumar, J. Schroers, P. Felfer, J.M. Cairney, and D.S. Gianola, Effect of ion irradiation on tensile ductility, strength and fictive temperature in metallic glass nanowires, Acta Materialia. 74 (2014) 165-182.

[45] W.F. Wu, Z. Han, and Y. Li, Size-dependent malleable-to-brittle transition in a bulk metallic glass, Applied Physics Letters. 93 (2008) 061908.

[46] C.A. Schuh, A.C. Lund, and T.G. Nieh, New regime of homogeneous flow in the deformation map of metallic glasses: elevated temperature nanoindentation experiments and mechanistic modeling, Acta Materialia. 52 (2004) 5879-5891.

[47] R.D. Conner, Y. Li, W.D. Nix, and W.L. Johnson, Shear band spacing under bending of Zr-based metallic glass plates, Acta Materialia. 52 (2004) 2429-2434.

[48] D.C. Hofmann, J.Y. Suh, A. Wiest, G. Duan, M.L. Lind, M.D. Demetriou, and W.L. Johnson, Designing metallic glass matrix composites with high toughness and tensile ductility, Nature. 451 (2008) 1085-9.

[49] G. Kumar, A. Desai, and J. Schroers, Bulk metallic glass: the smaller the better, Adv Mater. 23 (2011) 461-76.

[50] Y. Liu, H. Wu, C.T. Liu, Z. Zhang, and V. Keppens, Physical factors controlling the ductility of bulk metallic glasses, Applied Physics Letters. 93 (2008) 151915.

[51] J.J. Lewandowski, W.H. Wang, and A.L. Greer, Intrinsic plasticity or brittleness of metallic glasses, Philosophical Magazine Letters. 85 (2005) 77-87.

[52] S.F. Pugh, XCII. Relations between the elastic moduli and the plastic properties of polycrystalline pure metals, The London, Edinburgh, and Dublin Philosophical Magazine and Journal of Science. 45 (1954) 823-843.

[53] Y.-Y. Zhao, A. Inoue, C. Chang, J. Liu, B. Shen, X. Wang, and R.-W. Li, Composition effect on intrinsic plasticity or brittleness in metallic glasses, Scientific Reports. 4 (2014) 5733.

[54] Z. Liu, W. Chen, J. Carstensen, J. Ketkaew, R.M.O. Mota, J.K. Guest, and J. Schroers, 3D metallic glass cellular structures, Acta Materialia. 105 (2016) 35-43.

[55] L.J. Gibson, and M.F. Ashby, Cellular solids: structure and properties, Cambridge University Press, Cambridge; New York, 1999.

[56] A.H. Brothers, and D.C. Dunand, Plasticity and damage in cellular amorphous metals, Acta Materialia. 53 (2005) 4427-4440.

[57] A.H. Brothers, and D.C. Dunand, Ductile bulk metallic glass foams, Advanced Materials. 17 (2005) 484-486.

[58] X. Wei, J.H. Chen, and L.H. Dai, Energy absorption mechanism of open-cell Zr-based bulk metallic glass foam, Scripta Materialia. 66 (2012) 721-724.

[59] A.G. Evans, J.W. Hutchinson, N.A. Fleck, M.F. Ashby, and H.N.G. Wadley, The topological design of multifunctional cellular metals, Progress in Materials Science. 46 (2001) 309-327.

[60] A.G. Evans, J.W. Hutchinson, and M.F. Ashby, Multifunctionality of cellular metal systems, Progress in Materials Science. 43 (1998) 171-221.

[61] W. Chen, Z. Liu, H.M. Robinson, and J. Schroers, Flaw tolerance vs. performance: A tradeoff in metallic glass cellular structures, Acta Materialia. 73 (2014) 259-274.

[62] J. Rys, L. Valdevit, T.A. Schaedler, A.J. Jacobsen, W.B. Carter, and J.R. Greer, Fabrication and Deformation of Metallic Glass Micro-Lattices, Advanced Engineering Materials. 16 (2014) 889-896.

[63] S.-W. Lee, M. Jafary-Zadeh, D.Z. Chen, Y.-W. Zhang, and J.R. Greer, Size Effect Suppresses Brittle Failure in Hollow $Cu_{60}Zr_{40}$ Metallic Glass Nanolattices Deformed at Cryogenic Temperatures, Nano Letters. 15 (2015) 5673-81.

[64] D.M. Dimiduk, C. Woodward, R. Lesar, and M.D. Uchic, Scale-free intermittent flow in crystal plasticity, Science. 312 (2006) 1188-90.

[65] J.R. Greer, W.C. Oliver, and W.D. Nix, Size dependence of mechanical properties of gold at the micron scale in the absence of strain gradients, Acta Materialia. 53 (2005) 1821-1830.

[66] M.D. Uchic, D.M. Dimiduk, J.N. Florando, and W.D. Nix, Sample dimensions influence strength and crystal plasticity, Science. 305 (2004) 986-9.

[67] J.R. Greer, J.-Y. Kim, and M.J. Burek, The in-situ mechanical testing of nanoscale single-crystalline nanopillars, JOM. 61 (2009) 19-25.

[68] J.-Y. Kim, D. Jang, and J.R. Greer, Tensile and compressive behavior of tungsten, molybdenum, tantalum and niobium at the nanoscale, Acta Materialia. 58 (2010) 2355-2363.

[69] E.G. Fu, J. Carter, M. Martin, G. Xie, X. Zhang, Y.Q. Wang, R. Littleton, S. McDeavitt, and L. Shao, Ar-ion-milling-induced structural changes of $Cu_{50}Zr_{45}Ti_5$ metallic glass, Nuclear Instruments and Methods in Physics Research Section B: Beam Interactions with Materials and Atoms. 268 (2010) 545-549.

[70] J. Carter, E.G. Fu, M. Martin, G. Xie, X. Zhang, Y.Q. Wang, D. Wijesundera, X.M. Wang, W.-K. Chu, and L. Shao, Effects of Cu ion irradiation in $Cu_{50}Zr_{45}Ti_5$ metallic glass, Scripta Materialia. 61 (2009) 265-268.

[71] D. Kiener, C. Motz, M. Rester, M. Jenko, and G. Dehm, FIB damage of Cu and possible consequences for miniaturized mechanical tests, Materials Science and Engineering A. 459 (2007) 262-272.

[72] M.J. Burek, and J.R. Greer, Fabrication and microstructure control of nanoscale mechanical testing specimens via electron beam lithography and electroplating, Nano Letters. 10 (2009) 69-76.

[73] G.R. Odette, M.J. Alinger, and B.D. Wirth, Recent developments in irradiation-resistant steels, Annual Review of Materials Research. 38 (2008) 471-503.

[74] S.E. Donnelly, The density and pressure of helium in bubbles in implanted metals: a critical review, Radiation Effects. 90 (1985) 1-47.

[75] S.J. Zinkle, and J.T. Busby, Structural materials for fission & fusion energy, Materials Today. 12 (2009) 12-19.

[76] D. Kiener, P. Hosemann, S.A. Maloy, and A.M. Minor, In situ nanocompression testing of irradiated copper, Nature Materials. 10 (2011) 608-13.

[77] P. Landau, Q. Guo, K. Hattar, and J.R. Greer, The Effect of He Implantation on the Tensile Properties and Microstructure of Cu/Fe Nano-bicrystals, Advanced Functional Materials. 23 (2012) 1281-1288.

[78] Q. Guo, P. Landau, P. Hosemann, Y. Wang, and J.R. Greer, Helium implantation effects on the compressive response of Cu nanopillars, Small. 9 (2013) 691-6.

[79] P. Hosemann, Studying radiation damage in structural materials by using ion accelerators, Reviews of Accelerator Science and Technology. 4 (2011) 161-182.

[80] C.S. Lin, C.Y. Lee, F.J. Chen, and W.C. Li, Structural evolution and internal stress of nickel-phosphorus electrodeposits, Journal of the Electrochemical Society. 152 (2005) C370-C375.

[81] A.M. Pillai, A. Rajendra, and A.K. Sharma, Electrodeposited nickel--phosphorous (Ni--P) alloy coating: an in-depth study of its preparation, properties, and structural transitions, Journal of Coatings Technology and Research. 9 (2012) 785-797.

[82] P.K. Ng, D.D. Snyder, J. LaSala, B. Clemens, and C. Fuerst, Structure and Crystallization of Nickel-Phosphorus Alloys Prepared by High-Rate Electrodeposition, Journal of the Electrochemical Society. 135 (1988) 1376-1381.

[83] E. Bredael, B. Blanpain, J.-P. Celis, and J.R. Roos, On the Amorphous and Crystalline State of Electrodeposited Nickel-Phosphorus Coatings, Journal of the Electrochemical Society. 141 (1994) 294-299.

[84] A. Haseeb, P. Chakraborty, I. Ahmed, F. Caccavale, and R. Bertoncello, XRD, XPS and SIMS investigations on electrodeposited nickel-phosphorous alloy coatings, Thin Solid Films. 283 (1996) 140-144.

[85] J.F. Ziegler, M.D. Ziegler, and J.P. Biersack, SRIM--The stopping and range of ions in matter (2010), Nuclear Instruments and Methods in Physics Research Section B: Beam Interactions with Materials and Atoms. 268 (2010) 1818-1823.

[86] F. Frost, R. Fechner, B. Ziberi, J. Völlner, D. Flamm, and A. Schindler, Large area smoothing of surfaces by ion bombardment: fundamentals and applications, Journal of Physics: Condensed Matter. 21 (2009) 224026.

[87] F. Frost, R. Fechner, D. Flamm, B. Ziberi, W. Frank, and A. Schindler, Ion beam assisted smoothing of optical surfaces, Applied Physics A. 78 (2004) 651-654.

[88] J.W. Park, C.W. Sohn, and B.H. Choi, Some characteristics of materials surface-modified by ions beam bombardment, Current Applied Physics. 6 (2006) 188-193.

[89] B. Emmoth, M. Braun, T. Fried, J. Winter, F. Waelbroeck, and P. Wienhold, Helium irradiation of metallic glasses: sputtering and blistering properties, Journal of Nuclear Materials. 103 (1981) 393-396.

[90] R.V. Naneedkar, and A.K. Tyagi, Helium gas-bubble formation and blistering in metallic glass $Ni_{45}Fe_5Co_{20}Cr_{10}Mo_4B_{16}$, Radiation Effects. 58 (1981) 91-96.

[91] A.K. Tyagi, R.V. Nandedkar, and K. Krishan, Effect of 100 keV helium ion bombardment on surface topography and microstructure of $Ni_{33}Zr_{67}$, Journal of Nuclear Materials. 114 (1983) 181-189.

[92] A.K. Tyagi, R.V. Nandedkar, and K. Krishan, Blistering, flaking and bubble formation in metal-metalloid metallic glasses bombarded with helium ions, Journal of Nuclear Materials. 116 (1983) 29-39.

[93] A.K. Tyagi, and R.V. Nandedkar, Helium irradiation of Ni-(Zr or Nb) metallic glasses: Blistering, flaking and bubble formation, Journal of Nuclear Materials. 132 (1985) 62-69.

[94] P.V. Aksenov, A.N. Mansurova, A.V. Mikhailov, and A.I. Ryazanov, Investigation of the radiation damage of the amorphous $Ni_{60}Nb_{40}$ alloy and microcrystalline Ni during irradiation of 2.5 MeV alfa-particles, Journal of Non-Crystalline Solids. 117 (1990) 248-251.

[95] M.L. Jenkins, and M.A. Kirk, Characterization of radiation damage by transmission electron microscopy, Taylor & Francis, 2001.

[96] J. Carter, E.G. Fu, M. Martin, G. Xie, X. Zhang, Y.Q. Wang, D. Wijesundera, X.M. Wang, W.-K. Chu, and S.M. McDeavitt, Ion irradiation induced nanocrystal formation in amorphous $Zr_{55}Cu_{30}Al_{10}Ni_5$ alloy, Nuclear Instruments and Methods in Physics Research Section B: Beam Interactions with Materials and Atoms. 267 (2009) 2827-2831.

[97] G. Xie, L. Shao, D.V. Louzguine-Luzgin, and A. Inoue, He ion irradiation induced nanocrystallization in $Cu_{50}Zr_{45}Ti_5$ glassy alloy, Surface and Coatings Technology. 206 (2011) 829-833.

[98] G. Lu, G.Q.M. Lu, and Z.M. Xiao, Mechanical properties of porous materials, Journal of Porous Materials. 6 (1999) 359-368.

[99] X.W. Gu, C.N. Loynachan, Z. Wu, Y.-W. Zhang, D.J. Srolovitz, and J.R. Greer, Size-dependent deformation of nanocrystalline Pt nanopillars, Nano Letters. 12 (2012) 6385-92.

[100] H. Zhang, B.E. Schuster, Q. Wei, and K.T. Ramesh, The design of accurate micro-compression experiments, Scripta Materialia. 54 (2006) 181-186.

[101] D. Kiener, and A.M. Minor, Source truncation and exhaustion: insights from quantitative in situ TEM tensile testing, Nano Letters. 11 (2011) 3816-20.

[102] M.L. Falk, J.S. Langer, and L. Pechenik, Thermal effects in the shear-transformation-zone theory of amorphous plasticity: comparisons to metallic glass data, Physical Review E. 70 (2004) 011507.

[103] A.S. Argon, and H.Y. Kuo, Plastic flow in a disordered bubble raft (an analog of a metallic glass), Materials Science and Engineering. 39 (1979) 101-109.

[104] J.A. Knapp, D.M. Follstaedt, and S.M. Myers, Hardening by bubbles in He-implanted Ni, Journal of Applied Physics. 103 (2008) 013518-013518.

[105] D. Toma, M. Meuris, and U. Köster, Oxidation of Zr-based metallic glasses in air, Journal of Non-Crystalline Solids. 250 (1999) 719-723.

[106] Q. Jing, B. Zhang, J. Zhang, M. Ma, and R. Liu, Electrochemical corrosion and oxidation resistances of $Zr_{60}Ni_{21}Al_{19}$ bulk amorphous alloys, Science China Physics, Mechanics and Astronomy. 53 (2010) 2223-2226.

[107] Y.H. Li, W. Zhang, C. Dong, J.B. Qiang, A. Makino, and A. Inoue, Formation and mechanical properties of Zr--Ni--Al glassy alloys with high glass-forming ability, Intermetallics. 18 (2010) 1851-1855.

[108] S. Sato, T. Sanada, J. Saida, M. Imafuku, E. Matsubara, and A. Inoue, Effect of Al on local structures of Zr-Ni and Zr-Cu metallic glasses, Materials Transactions. 46 (2005) 2893-2897.

[109] Q. Jing, Y. Zhang, D. Wang, and Y. Li, A study of the glass forming ability in ZrNiAl alloys, Materials Science and Engineering A. 441 (2006) 106-111.

[110] K. Zhang, Y. Liu, J. Schroers, M.D. Shattuck, and C.S. O'Hern, The glass-forming ability of model metal-metalloid alloys, The Journal of Chemical Physics. 142 (2015) 104504.

[111] S. Plimpton, Fast parallel algorithms for short-range molecular dynamics, Journal of Computational Physics. 117 (1995) 1-19.

[112] Howard Sheng, School of Physics, Astronomy & Computational Sciences, George Mason University, Fairfax, VA 22030 (Potential provided through private communications), (n.d.).

[113] D.J. Evans, and B.L. Holian, The nose--hoover thermostat, The Journal of Chemical Physics. 83 (1985) 4069-4074.

[114] H.C. Andersen, RATTLE: A Velocity version of the SHAKE algorithm for molecular dynamics calculations, Journal of Computational Physics. 52 (1983) 24-34.

[115] P.S. Branicio, and D.J. Srolovitz, Local stress calculation in simulations of multicomponent systems, Journal of Computational Physics. 228 (2009) 8467-8479.

[116] D.H. Tsai, The virial theorem and stress calculation in molecular dynamics, The Journal of Chemical Physics. 70 (1979) 1375-1382.

[117] F. Shimizu, S. Ogata, and J. Li, Theory of shear banding in metallic glasses and molecular dynamics calculations, Materials Transactions. 48 (2007) 2923-2927.

[118] A. Stukowski, Visualization and analysis of atomistic simulation data with OVITO--the Open Visualization Tool, Modelling and Simulation in Materials Science and Engineering. 18 (2010) 015012.

[119] J.L. Finney, Random packings and the structure of simple liquids. I. The geometry of random close packing, Proceedings of the Royal Society of London A: Mathematical, Physical and Engineering Sciences. 319 (1970) 479-493.

[120] H.W. Sheng, W.K. Luo, F.M. Alamgir, J.M. Bai, and E. Ma, Atomic packing and short-to-medium-range order in metallic glasses, Nature. 439 (2006) 419-25.

[121] J. Ding, Y.-Q. Cheng, and E. Ma, Full icosahedra dominate local order in $Cu_{64}Zr_{34}$ metallic glass and supercooled liquid, Acta Materialia. 69 (2014) 343-354.

[122] A. Hirata, L.J. Kang, T. Fujita, B. Klumov, K. Matsue, M. Kotani, A.R. Yavari, and M.W. Chen, Geometric frustration of icosahedron in metallic glasses, Science. 341 (2013) 376-379.

[123] J. Lu, G. Ravichandran, and W.L. Johnson, Deformation behavior of the $Zr_{41.2}Ti_{13.8}Cu_{12.5}Ni_{10}Be_{22.5}$ bulk metallic glass over a wide range of strain-rates and temperatures, Acta Materialia. 51 (2003) 3429-3443.

[124] Y.Q. Cheng, A.J. Cao, and E. Ma, Correlation between the elastic modulus and the intrinsic plastic behavior of metallic glasses: The roles of atomic configuration and alloy composition, Acta Materialia. 57 (2009) 3253-3267.

[125] A.J. Cao, Y.Q. Cheng, and E. Ma, Structural processes that initiate shear localization in metallic glass, Acta Materialia. 57 (2009) 5146-5155.

[126] P. Murali, T.F. Guo, Y.W. Zhang, R. Narasimhan, Y. Li, and H.J. Gao, Atomic scale fluctuations govern brittle fracture and cavitation behavior in metallic glasses, Physical Review Letters. 107 (2011) 215501.

[127] X.W. Gu, M. Jafary-Zadeh, D.Z. Chen, Z. Wu, Y.-W. Zhang, D.J. Srolovitz, and J.R. Greer, Mechanisms of failure in nanoscale metallic glass, Nano Letters. 14 (2014) 5858-64.

[128] S. Adibi, P.S. Branicio, R. Liontas, D.Z. Chen, J.R. Greer, D.J. Srolovitz, and S.P. Joshi, Surface roughness imparts tensile ductility to nanoscale metallic glasses, Extreme Mechanics Letters. 5 (2015) 88-95.

[129] S. Adibi, Z.-D. Sha, P.S. Branicio, S.P. Joshi, Z.-S. Liu, and Y.-W. Zhang, A transition from localized shear banding to homogeneous superplastic flow in nanoglass, Applied Physics Letters. 103 (2013) 211905.

[130] Z.D. Sha, L.C. He, Q.X. Pei, H. Pan, Z.S. Liu, Y.W. Zhang, and T.J. Wang, On the notch sensitivity of CuZr nanoglass, Journal of Applied Physics. 115 (2014) 163507.

[131] Y.Q. Cheng, A.J. Cao, H.W. Sheng, and E. Ma, Local order influences initiation of plastic flow in metallic glass: Effects of alloy composition and sample cooling history, Acta Materialia. 56 (2008) 5263-5275.

[132] J. Ding, S. Patinet, M.L. Falk, Y. Cheng, and E. Ma, Soft spots and their structural signature in a metallic glass, Proceedings of the National Academy of Sciences. 111 (2014) 14052-14056.

[133] L. Zhang, Y.-Q. Cheng, A. Cao, J. Xu, and E. Ma, Bulk metallic glasses with large plasticity: Composition design from the structural perspective, Acta Materialia. 57 (2009) 1154-1164.

[134] A.R. Yavari, A. Le Moulec, A. Inoue, N. Nishiyama, N. Lupu, E. Matsubara, W.J. Botta, G. Vaughan, M. Di Michiel, and Kvick, Excess free volume in metallic glasses measured by X-ray diffraction, Acta Materialia. 53 (2005) 1611-1619.

[135] A.R. Yavari, M. Tonegaru, N. Lupu, A. Inoue, E. Matsubara, G. Vaughan, Kvick, and W.J. Botta, Quenched-in Free Volume V_f, Deformation-induced Free Volume, the Glass Transition T_g and Thermal Expansion in glassy ZrNbCuNiAl measured by Time-resolved Diffraction in Transmission, MRS Proceedings, (2003) MM3-5.

[136] E. Teatum, K. Gschneidner Jr, and J. Waber, Compilation of calculated data useful in predicting metallurgical behavior of the elements in binary alloy systems, 1959.

[137] D. Caprion, and H.R. Schober, Influence of the quench rate and the pressure on the glass transition temperature in selenium, The Journal of Chemical Physics. 117 (2002) 2814-2818.

[138] U. Ramamurty, M.L. Lee, J. Basu, and Y. Li, Embrittlement of a bulk metallic glass due to low-temperature annealing, Scripta Materialia. 47 (2002) 107-111.

[139] F.H. Stillinger, A topographic view of supercooled liquids and glass formation, Science. 267 (1995) 1935-9.

[140] P. Murali, and U. Ramamurty, Embrittlement of a bulk metallic glass due to sub-T_g annealing, Acta Materialia. 53 (2005) 1467-1478.

[141] D. Suh, and R.H. Dauskardt, Mechanical relaxation time scales in a Zr--Ti--Ni--Cu--Be bulk metallic glass, Journal of Materials Research. 17 (2002) 1254-1257.

[142] Y. Fan, T. Iwashita, and T. Egami, How thermally activated deformation starts in metallic glass, Nature Communications. 5 (2014) 5083.

[143] M. Mehra, W.L. Johnson, A.P. Thakoor, and S.K. Khanna, Influence of preparation techniques on the structure of amorphous metallic alloy $(Mo_{0.6}Ru_{0.4})_{82}B_{18}$, Solid State Communications. 47 (1983) 859-862.

[144] A. Van den Beukel, and J. Sietsma, The glass transition as a free volume related kinetic phenomenon, Acta Metallurgica Et Materialia. 38 (1990) 383-389.

[145] Q.-K. Li, and M. Li, Assessing the critical sizes for shear band formation in metallic glasses from molecular dynamics simulation, Applied Physics Letters. 91 (2007) 231905.

[146] F. Delogu, Molecular dynamics study of size effects in the compression of metallic glass nanowires, Physical Review B. 79 (2009) 184109.

[147] T. Mukai, T.G. Nieh, Y. Kawamura, A. Inoue, and K. Higashi, Effect of strain rate on compressive behavior of a $Pd_{40}Ni_{40}P_{20}$ bulk metallic glass, Intermetallics. 10 (2002) 1071-1077.

[148] C.A. Volkert, and A.M. Minor, Focused ion beam microscopy and micromachining, MRS Bulletin. 32 (2007) 389-399.

[149] G. Moser, H. Felber, B. Rashkova, P.J. Imrich, C. Kirchlechner, W. Grosinger, C. Motz, G. Dehm, and D. Kiener, Sample preparation by metallography and focused ion beam for nanomechanical testing, Practical Metallography. 49 (2012) 343-355.

[150] S. Nagata, S. Higashi, B. Tsuchiya, K. Toh, T. Shikama, K. Takahiro, K. Ozaki, K. Kawatusra, S. Yamamoto, and A. Inouye, Ion irradiation effects on amorphization and thermal crystallization in Zr--Al--Ni--Cu alloys, Nuclear Instruments and Methods in Physics Research Section B: Beam Interactions with Materials and Atoms. 257 (2007) 420-423.

[151] T. Nagase, and Y. Umakoshi, Electron irradiation induced nanocrystallization behavior in $Fe_{71}Zr_9B_{20}$ metallic glass, Materials Transactions. 46 (2005) 608-615.

[152] P.J. Tao, Y.Z. Yang, Z.X. Mu, X.C. Chen, and Z.W. Xie, Influences of ion implantation on non-isothermal crystallization behaviors of bulk metallic glass, Journal of Alloys and Compounds. 479 (2009) 736-740.

[153] H. Gao, B. Ji, I.L. Jager, E. Arzt, and P. Fratzl, Materials become insensitive to flaws at nanoscale: lessons from nature, Proceedings of the National Academy of Sciences of the United States of America. 100 (2003) 5597-600.

[154] R. Liontas, X.W. Gu, E. Fu, Y. Wang, N. Li, N. Mara, and J.R. Greer, Effects of helium implantation on the tensile properties and microstructure of $Ni_{73}P_{27}$ metallic glass nanostructures, Nano Letters. 14 (2014) 5176-83.

[155] J. Fischer, and M. Wegener, Three-dimensional optical laser lithography beyond the diffraction limit, Laser & Photonics Reviews. 7 (2013) 22-44.

[156] W. Xiong, Y.S. Zhou, X.N. He, Y. Gao, M. Mahjouri-Samani, L. Jiang, T. Baldacchini, and Y.F. Lu, Simultaneous additive and subtractive three-dimensional nanofabrication using integrated two-photon polymerization and multiphoton ablation, Light: Science & Applications. 1 (2012) e6.

[157] H.-B. Sun, and S. Kawata, NMR 3D Analysis Photopolymerization, NMR 3D Analysis Photopolymerization. (2004) 169-273.

[158] L. Montemayor, V. Chernow, and J.R. Greer, Materials by design: Using architecture in material design to reach new property spaces, MRS Bulletin. 40 (2015) 1122-1129.

[159] D. Jang, L.R. Meza, F. Greer, and J.R. Greer, Fabrication and deformation of three-dimensional hollow ceramic nanostructures, Nature Materials. 12 (2013) 893-8.

[160] L.R. Meza, and J.R. Greer, Mechanical characterization of hollow ceramic nanolattices, Journal of Materials Science. 49 (2014) 2496-2508.

[161] L.R. Meza, S. Das, and J.R. Greer, Strong, lightweight, and recoverable three-dimensional ceramic nanolattices, Science. 345 (2014) 1322-6.

[162] L.R. Meza, A.J. Zelhofer, N. Clarke, A.J. Mateos, D.M. Kochmann, and J.R. Greer, Resilient 3D hierarchical architected metamaterials, Proceedings of the National Academy of Sciences of the United States of America. 112 (2015) 11502-7.

[163] L.C. Montemayor, W.H. Wong, Y.-W. Zhang, and J.R. Greer, Insensitivity to Flaws Leads to Damage Tolerance in Brittle Architected Meta-Materials, Scientific Reports. 6 (2016) 20570.

[164] L.C. Montemayor, L.R. Meza, and J.R. Greer, Design and Fabrication of Hollow Rigid Nanolattices via Two-Photon Lithography, Advanced Engineering Materials. 16 (2013) 184-189.

[165] L.C. Montemayor, and J.R. Greer, Mechanical Response of Hollow Metallic Nanolattices: Combining Structural and Material Size Effects, Journal of Applied Mechanics. 82 (2015) 071012.

[166] J. Schroers, C. Veazey, and W.L. Johnson, Amorphous metallic foam, Applied Physics Letters. 82 (2003) 370-372.

[167] J. Schroers, C. Veazey, M.D. Demetriou, and W.L. Johnson, Synthesis method for amorphous metallic foam, Journal of Applied Physics. 96 (2004) 7723-7730.

[168] T. Wada, and A. Inoue, Fabrication, thermal stability and mechanical properties of porous bulk glassy Pd-Cu-Ni-P alloys, Materials Transactions. 44 (2003) 2228-2231.

[169] A.H. Brothers, R. Scheunemann, J.D. DeFouw, and D.C. Dunand, Processing and structure of open-celled amorphous metal foams, Scripta Materialia. 52 (2005) 335-339.

[170] M.H. Lee, and D.J. Sordelet, Synthesis of bulk metallic glass foam by powder extrusion with a fugitive second phase, Applied Physics Letters. 89 (2006) 21921-21921.

[171] V.S. Deshpande, N.A. Fleck, and M.F. Ashby, Effective properties of the octet-truss lattice material, Journal of the Mechanics and Physics of Solids. 49 (2001) 1747-1769.

[172] N.A. Fleck, V.S. Deshpande, and M.F. Ashby, Micro-architectured materials: past, present and future, Proceedings of the Royal Society of London A: Mathematical, Physical and Engineering Sciences. 466 (2010) 2495-2516.

[173] V.S. Deshpande, M.F. Ashby, and N.A. Fleck, Foam topology: bending versus stretching dominated architectures, Acta Materialia. 49 (2001) 1035-1040.

[174] M.F. Ashby, The properties of foams and lattices, Philosophical Transactions of the Royal Society A. 364 (2006) 15-30.

[175] W.C. Oliver, and G.M. Pharr, An improved technique for determining hardness and elastic modulus using load and displacement sensing indentation experiments, Journal of Materials Research. 7 (1992) 1564-1583.

[176] H.G. Allen, and P.S. Bulson, Background to Buckling, McGraw-Hill, 1980.

[177] Personal communication with L.R. Meza, (2016).

[178] Z. Zhang, V. Keppens, P.K. Liaw, Y. Yokoyama, and A. Inoue, Elastic properties of Zr-based bulk metallic glasses studied by resonant ultrasound spectroscopy, Journal of Materials Research. 22 (2007) 364-367.

[179] X.W. Gu, and J.R. Greer, Ultra-strong architected Cu meso-lattices, Extreme Mechanics Letters. 2 (2015) 7-14.

[180] E.M. Bringa, J.D. Monk, A. Caro, A. Misra, L. Zepeda-Ruiz, M. Duchaineau, F. Abraham, M. Nastasi, S.T. Picraux, Y.Q. Wang, and D. Farkas, Are nanoporous materials radiation resistant?, Nano Letters. 12 (2012) 3351-5.

[181] E.G. Fu, M. Caro, L.A. Zepeda-Ruiz, Y.Q. Wang, K. Baldwin, E. Bringa, M. Nastasi, and A. Caro, Surface effects on the radiation response of nanoporous Au foams, Applied Physics Letters. 101 (2012) 191607.

[182] C. Sun, D. Bufford, Y. Chen, M.A. Kirk, Y.Q. Wang, M. Li, H. Wang, S.A. Maloy, and X. Zhang, In situ study of defect migration kinetics in nanoporous Ag with enhanced radiation tolerance, Scientific Reports. 4 (2014) 3737.

[183] L.A. Zepeda-Ruiz, E. Martinez, M. Caro, E.G. Fu, and A. Caro, Deformation mechanisms of irradiated metallic nanofoams, Applied Physics Letters. 103 (2013) 031909.

[184] M. Caro, W.M. Mook, E.G. Fu, Y.Q. Wang, C. Sheehan, E. Martinez, J.K. Baldwin, and A. Caro, Radiation induced effects on mechanical properties of nanoporous gold foams, Applied Physics Letters. 104 (2014) 233109.

[185] Z. Hu, Z. Zhao, Y. Hu, J. Xing, T. Lu, and B. Wei, Effect of ion irradiation on mechanical behaviors of $Ti_{40}Zr_{25}Be_{30}Cr_5$ bulk metallic glass, Materials Research. 15 (2012) 713-717.

[186] T. Mattila, R.M. Nieminen, and M. Dzugutov, Simulation of radiation-induced structural transformation in amorphous metals, Physical Review B. 53 (1996) 192-200.

[187] K.A. Avchaciov, Y. Ritter, F. Djurabekova, K. Nordlund, and K. Albe, Controlled softening of $Cu_{64}Zr_{36}$ metallic glass by ion irradiation, Applied Physics Letters. 102 (2013) 181910.

[188] K.A. Avchaciov, Y. Ritter, F. Djurabekova, K. Nordlund, and K. Albe, Effect of ion irradiation on structural properties of $Cu_{64}Zr_{36}$ metallic glass, Nuclear Instruments and Methods in Physics Research Section B: Beam Interactions with Materials and Atoms. 341 (2014) 22-26.

[189] D.Z. Chen, X.W. Gu, Q. An, W.A. Goddard III, and J.R. Greer, Ductility and work hardening in nano-sized metallic glasses, Applied Physics Letters. 106 (2015) 061903.

[190] R. Liontas, M. Jafary-Zadeh, Q. Zeng, Y.-W. Zhang, W.L. Mao, and J.R. Greer, Substantial tensile ductility in sputtered Zr-Ni-Al nano-sized metallic glass, Acta Materialia. 118 (2016) 270-285.

[191] X.L. Bian, G. Wang, H.C. Chen, L. Yan, J.G. Wang, Q. Wang, P.F. Hu, J.L. Ren, K.C. Chan, and N. Zheng, Manipulation of free volumes in a metallic glass through Xe-ion irradiation, Acta Materialia. 106 (2016) 66-77.

[192] Y. Fukumoto, A. Ishii, A. Iwase, Y. Yokoyama, and F. Hori, Behavior of free volume in ZrCuAl bulk metallic glass after irradiation, Journal of Physics: Conference Series. 225 (2010) 012010.

[193] M. Iqbal, J.I. Akhter, Z.Q. Hu, H.F. Zhang, A. Qayyum, and W.S. Sun, Mechanical properties and ion irradiation of bulk amorphous $Zr_{55}Cu_{30}Al_{10}Ni_5$ alloy, Journal of Non-Crystalline Solids. 353 (2007) 2452-2458.

[194] P.J. Tao, Y.Z. Yang, X.J. Bai, Z.X. Mu, G.Q. Li, Z.W. Xie, and X.C. Chen, Study on implantation of Co ions in ZrCuNiAl bulk metallic glass, Surface and Coatings Technology. 203 (2009) 1656-1659.

[195] Y.Z. Yang, P.J. Tao, G.Q. Li, Z.X. Mu, Q. Ru, Z.W. Xie, and X.C. Chen, Effects of ion implantation on surface structures and properties for bulk metallic glass, Intermetallics. 17 (2009) 722-726.

[196] J. Carter, E.G. Fu, G. Bassiri, B.M. Dvorak, N. David Theodore, G. Xie, D.A. Lucca, M. Martin, M. Hollander, and X. Zhang, Effects of ion irradiation in metallic glasses, Nuclear Instruments and Methods in Physics Research Section B: Beam Interactions with Materials and Atoms. 267 (2009) 1518-1521.

[197] Y. Huang, H. Fan, X. Zhou, P. Xue, Z. Ning, D. Daisenberger, J. Sun, and J. Shen, Structure and mechanical property modification of a Ti-based metallic glass by ion irradiation, Scripta Materialia. 103 (2015) 41-44.

[198] A.G. Perez-Bergquist, H. Bei, K.J. Leonard, Y. Zhang, and S.J. Zinkle, Effects of ion irradiation on $Zr_{52.5}Cu_{17.9}Ni_{14.6}Al_{10}Ti_5$ (BAM-11) bulk metallic glass, Intermetallics. 53 (2014) 62-66.

[199] R. Raghavan, B. Kombaiah, M. Döbeli, R. Erni, U. Ramamurty, and J. Michler, Nanoindentation response of an ion irradiated Zr-based bulk metallic glass, Materials Science and Engineering A. 532 (2012) 407-413.